A FULL WAVE CODE FOR ION CYCLOTRON WAVES IN TOROIDAL PLASMAS

Dr. Marco Brambilla

IPP 5/66 Februar 1996

MAX-PLANCK-INSTITUT FÜR PLASMAPHYSIK

85748 GARCHING BEI MÜNCHEN

„Dieser IPP-Bericht ist als Manuskript des Autors gedruckt. Die Arbeit entstand im Rahmen der Zusammenarbeit zwischen dem IPP und EURATOM auf dem Gebiet der Plasmaphysik. Alle Rechte vorbehalten."

"This IPP-Report has been printed as author's manuscript elaborated under the collaboration between the IPP and EURATOM on the field of plasma physics. All rights reserved."

MAX-PLANCK-INSTITUT FÜR PLASMAPHYSIK

GARCHING BEI MÜNCHEN

A FULL WAVE CODE FOR ION CYCLOTRON WAVES IN TOROIDAL PLASMAS

Dr. Marco Brambilla

IPP 5/66 Februar 1996

Die nachstehende Arbeit wurde im Rahmen des Vertrages zwischen dem Max-Planck-Institut für Plasmaphysik und der Europäischen Atomgemeinschaft über die Zusammenarbeit auf dem Gebiete der Plasmaphysik durchgeführt.

A FULL WAVE CODE FOR ION CYCLOTRON WAVES IN TOROIDAL PLASMAS

Marco Brambilla

Max–Planck Institut für Plasmaphysik
EURATOM Association
Garching bei München, Germany

ABSTRACT

The code TORIC solves the finite Larmor radius wave equations in the ion cyclotron frequency range in arbitrary axisymmetric toroidal geometry. The model used describes the compressional and torsional Alfvén waves (or, depending on the parallel phase velocity, the kinetic counterpart of the latter), and ion Bernstein waves excited by mode conversion near the first ion cyclotron harmonic. In the ion response the broadening of the absorption regions due to the finite width of the cyclotron resonance of individual ions in toroidal geometry is taken into account. The parallel component of the wave electric field is evaluated on the same footing as the transverse ones; the response of the electrons includes Landau damping, Transit Time damping and the mixed term.

The numerical approach uses a spectral representation of the solution in the poloidal angle ϑ, and cubic finite elements in the radial variable ψ. Great flexibility is provided in the way ion Bernstein waves excited by mode conversion are damped when their wavelength becomes comparable with the ion Larmor radius, in the regularization of Alfvén resonances, and in the treatment of the outer plasma layers. As an option, we have also implemented the Order Reduction Algorithm, which provides a particularly fast, yet accurate evaluation of the power deposition profiles in toroidal geometry. The present report describes the model and its numerical implementation, and provides the information needed to use the code. A few examples illustrating applications of TORIC are also included.

1 – Introduction.

Considerable effort has been devoted to the theoretical and numerical modelling of ion cyclotron (IC) heating of tokamak plasmas. Among the most ambitious goals is the solution of Maxwell equations in a hot plasma in toroidal geometry. Several codes have been developed for this purpose [1]–[6] (for a review and further references, cfr. [7]). They find application in understanding present experiments, e.g. in JET, ASDEX Upgrade, ALCATOR C-mod, and in planning h.f. heating and current drive in future ones, in particular ITER.

In this Report we document a new version of the toroidal ion cyclotron full wave code first described in [4], which has been completely rewritten and renamed TORIC. This code solves the finite Larmor radius (FLR) wave equations in arbitrary axisymmetric toroidal geometry in the so–called Swanson–Colestock–Kashuba (SCK) approximation [8]–[9] augmented by the appropriate FLR terms for the electrons [10]. The numerical approach is based on the spectral representation of the solution in the poloidal angle ϑ, and on cubic finite elements [11] in the radial variable ψ. The new version is considerably faster than the original one, contains more physics, and has a number of additional options.

With respect to [4] the most important innovations of TORIC are:

a) Toroidal effects on parallel dispersion are treated more accurately. In toroidal geometry the existence of a gradient of the magnetic field strength along magnetic field lines results in a broadening of the thermal Doppler width of the cyclotron absorption region. A quantitatively accurate approximation for this important effect has been found which can be implemented without appreciably slowing execution.

b) The finite Larmor terms in the plasma h.f. current has been carefully written in toroidal geometry by putting it explicitly in vector form. This turns out to be important, in particular, for the ion contribution resonant near the first ion cyclotron harmonic, $\omega = 2\Omega_c$.

c) The parallel component of the electric field is evaluated on the same footing as the perpendicular components, rather than iteratively. This improves the accuracy of the evaluation of power absorption by the electrons, and makes possible a more reliable evaluation of the efficiency of current drive by h.f. waves in the IC frequency range.

d) As an option, we have implemented the Order Reduction Algorithm (ORA) [12], which replaces the excitation of ion Bernstein waves by an equivalent power sink. Although based on an euristic approach, the power deposition profiles obtained in this way are quite accurate; the suppression of short wavelength features in the solution, on the other hand, allows relatively coarse meshes both in the poloidal and the radial directions. The resulting reduction in execution time and memory requirements make

the ORA option of TORIC a useful tool for routine analysis of IC heating, possibly also in conjunction with other codes, such as those describing radial transport in tokamaks.

Other improvements include: more flexibility in the way ion Bernstein waves are damped when their wavelength becomes comparable with the ion Larmor radius; collisional damping by the electrons; the possibility of artificially broadening Alfvén resonances occurring at the plasma periphery; and several optionals models for the outer plasma layers. Greater execution speed has been obtained by careful vectorization, and a new, simpler solver has been written.

The present documentation has been written with three goals in view. The first is to acquaint users with the possibilities and limitations of TORIC. To get reliable results with a full-wave code requires a good preliminary knowledge of the physics of IC heating in general and of the SCK model in particular, and also some familiarity with the numerical problems arising from the limited resolution achievable in practice by the poloidal and radial meshes. In the second place, we have tried to facilitate the comparison with other codes which solve the same problem. It is often difficult to trace the origin of discrepancies between results obtained with different codes, because too many details of each implementation are not available; here we give a reasonably complete information covering both the physical model and the numerical realization. The last goal is to facilitate future extensions of the code. A few domains in which such extensions are desirable and might soon become feasible are mentioned below.

This report is organized as follows. In section 2 we describe the plasma configuration used, and in section 3 we introduce the wave equations of the SCK model and the associated boundary conditions. In section 4 the wave equations are put into the weak variational form which is the basis of the finite elements (FEM) discretization used in TORIC. In section 5 the spectral representation of the solution is introduced and the contributions of the various terms to the stiffness matrix are listed. Section 6 is devoted to the regularity conditions at the magnetic axis and to the boundary conditions at the antenna and Faraday shield. In section 7 we discuss our treatment of the integrals along magnetic field lines which arise from the integration of the linearized Vlasov equation (which describe the effects of toroidicity on parallel dispersion), and the related problem of the power balance. Ad–hoc damping of ion Bernstein waves and collisional broadening of Alfvén resonances occurring near the plasma edge are also discussed in this section. The Order Reduction Algorithm is introduced in section 8. Section 9 summarizes the numerical implementation of the spectral Ansatz and of the radial discretization, and sketches the structure of the solver. In section 10 we lists the available options and offer some advice on the use of the code, stressing in particular the limitations of the model and those of the numerical realization. Finally, a few examples are presented in section 11. The parameters and input variables which must be defined by the user are given in the Appendix.

Before proceeding to the description of the code, it is worth identifying a few areas in which further work would be desirable. One is the inclusion of quasilinear effects. The present version assumes that all species have Maxwellian distribution functions; the only way to take into account suprathermal ions is to treat them as a separate population with a different temperature. The main obstacle against allowing for general non–Maxwellian distribution functions is the enormous slowing down of execution speed which this would imply. Adequate approximations for the quasilinear distribution function of IC heated ions which would still permit a reasonably fast evaluation of the coefficients of the wave equations are available, however [13] (we insist on the fact that these approximations are much less sophisticated than those required for the complete specification of the ion distribution function [14]), and it might soon be possible to use them in TORIC.

Another domain in which new developments would be useful is in modelling the antennas. In TORIC the numerical integration extends all the way to the vessel, with appropriate jump conditions imposed at the Faraday shield and at the antenna conductors. This has the advantage of simplicity, and helps to avoid solutions dominated by surface modes, which sometimes develop when boundary conditions are imposed along an artificial discontinuity between plasma and vacuum. On the other hand it greatly restricts the flexibility of the antenna modelling, since the antenna is situated in the region where achieving a good numerical resolution with a reasonable mesh is most difficult. Although several choices are offered for the treatment of the region behind the Faraday screen, ranging from a vacuum layer to the continuation of the scrape–off plasma (cfr. section 8.2 d), an optional analytic model for this region would also be desirable. The modularity of TORIC should allow to easily implement such a model without altering the basic structure of the code.

We would like to recall that although the code has been largely rewritten, its basic structure is still the same as that of the first version, developed in collaboration with Dr. T. Krücken. Useful comments and suggestions from Drs. P. Bonoli, D. Batchelor, C.S. Chiu and E. F. Jaeger are also gratefully aknowledged.

2 – The model.

2.1 – The MHD configuration. We use a representation of the axisymmetric MHD equilibrium of the form:

$$X = X(\psi, \vartheta) \qquad\qquad Z = Z(\psi, \vartheta) \tag{2.1}$$

where X, Z are horizontal and vertical Cartesian coordinates in the poloidal cross–section, with origin at a distance R_o from the vertical axis (the centre of the vacuum vessel); a is the plasma radius. Thus $R = R_o + X$, ϕ, Z constitute a cylindrical coordinate system. The dimensionless variable ψ ($0 \leq \psi \leq 1$) which labels magnetic surfaces, the poloidal angle ϑ ($0 \leq \vartheta \leq 2\pi$), and the toroidal angle $\varphi = -\phi$ (the change in sign is needed to make both systems right–handed) will be called 'magnetic coordinates'. Note that ψ is assumed proportional to the radius rather than the area (or the magnetic flux) of the magnetic surface.

The Jacobian of Eqs. (2.1),

$$J = \left(\frac{\partial X}{\partial \psi}\right)\left(\frac{\partial Z}{\partial \vartheta}\right) - \left(\frac{\partial Z}{\partial \psi}\right)\left(\frac{\partial X}{\partial \vartheta}\right) \tag{2.2}$$

vanishes only on the magnetic axis $R_m = R_o + \Delta(0)$. The covariant metric of the magnetic coordinates can be written

$$g_{ij} = \begin{pmatrix} N_\psi^2 & G & 0 \\ G & N_\tau^2 & 0 \\ 0 & 0 & R^2 \end{pmatrix} \tag{2.3}$$

with determinant

$$g = (\det(g_{ij}))^{1/2} = RJ \tag{2.4}$$

and elements

$$\begin{aligned} N_\tau^2 &= \left(\frac{\partial X}{\partial \vartheta}\right)^2 + \left(\frac{\partial Z}{\partial \vartheta}\right)^2 \\ G &= \left(\frac{\partial X}{\partial \psi}\right)\left(\frac{\partial X}{\partial \vartheta}\right) + \left(\frac{\partial Z}{\partial \psi}\right)\left(\frac{\partial Z}{\partial \vartheta}\right) \\ N_\psi^2 &= \left(\frac{\partial X}{\partial \psi}\right)^2 + \left(\frac{\partial Z}{\partial \psi}\right)^2 \end{aligned} \tag{2.5}$$

satisfying the identity $N_\psi^2 N_\tau^2 = J^2 + G^2$. In general ψ and ϑ are not orthogonal, i.e. $G \neq 0$. Orthogonal unit vectors $\vec{u}_\psi$, $\vec{u}_\tau$ in the poloidal cross–section can nevertheless defined at each point through

$$\begin{aligned} \vec{u}_\psi &= \frac{1}{N_\tau}\left(\frac{\partial Z}{\partial \vartheta}\vec{u}_X - \frac{\partial X}{\partial \vartheta}\vec{u}_Z\right) \\ \vec{u}_\tau &= \frac{1}{N_\tau}\left(\frac{\partial X}{\partial \vartheta}\vec{u}_X + \frac{\partial Z}{\partial \vartheta}\vec{u}_Z\right) \end{aligned} \tag{2.6}$$

where $\vec{u}_X$ and $\vec{u}_Z$ are unit vectors of the cartesian coordinates. The elements of g_{ij} and J have all the dimensions of a length squared, and tend to zero when $\psi \to 0$. For circular cross–sections $N_\tau = r$, the minor radius.

Explicitly, we use

$$\begin{aligned} X(\psi,\vartheta) &= \Delta(\psi) + a\psi\cos\left(\vartheta - \delta(\psi)\sin\vartheta\right) \\ Z(\psi,\vartheta) &= a\eta(\psi)\sin\vartheta \end{aligned} \tag{2.7}$$

The static magnetic field has the covariant and physical representations

$$\begin{aligned} \vec{B} &= B_o R_o \left\{ a\, f(\psi)\, \vec{\nabla}\varphi \times \vec{\nabla}\psi + g(\psi)\, \vec{\nabla}\varphi \right\} \\ &= \frac{R_o}{R} B_o \left(\sin\Theta\, \vec{e}_\tau + \cos\Theta\, \vec{e}_\varphi\right) \end{aligned} \tag{2.8}$$

respectively, with

$$\tan\Theta = \frac{B_\tau}{B_\varphi} = a\,\frac{N_\tau}{J}\,\frac{f(\psi)}{g(\psi)} \tag{2.9}$$

The functions $\Delta(\psi)$ (Shafranov shift), $\eta(\psi)$ (ellipticity) and $\delta(\psi)$ (triangularity), as well as $f(\psi)$ and $g(\psi)$ should in principle be specified consistently with the MHD equilibrium conditions. The stand–alone TORIC code, however, is not coupled to a solver of the Grad–Shafranov equation, although such coupling woud require a very simple interfacing. As a default, simple analytic representations are used, namely:

$$\begin{aligned} \Delta(\psi) &= \Delta_o(1-\psi^2) \\ \delta(\psi) &= \delta_o\psi^2 \\ \eta(\psi) &= \left[e_o + (e_1 - e_o)\psi^2\right]\psi \end{aligned} \tag{2.10}$$

Here Δ_o is the Shafranov shift of the magnetic axis, and e_o, e_1 the ellipticity at the magnetic axis and at the plasma edge, respectively. The dependence of $R\,B_\varphi$ on ψ, which is a finite–β effect, is neglected, i.e. $g(\psi) = 1$. On the other hand $f(\psi)$ is determined from Faraday law:

$$f(\psi) = \frac{4\pi}{c}\,\frac{I(\psi)}{R_o a\, B_o \int_0^{2\pi} (N_\tau/RJ)\, d\vartheta} \tag{2.11}$$

where

$$I(\psi) = \int_{\psi'<\psi} \vec{J}(\psi')\cdot d\vec{S}_\varphi \tag{2.12}$$

is the total toroidal current inside the magnetic surface ψ. This ensures that the equilibrium conditions are satisfied at least on average on each magnetic surface.

2.2 – Differential operators in Stix components. The wave equations in the plasma are naturally written in the local 'Stix' frame, whose basis unit vectors are related to those of the magnetic coordinates by

$$\begin{aligned} \vec{u}_\xi &= \vec{u}_\psi \\ \vec{u}_\eta &= \cos\Theta\ \vec{u}_\tau - \sin\Theta\ \vec{u}_\varphi \\ \vec{u}_\zeta &= \sin\Theta\ \vec{u}_\tau + \cos\Theta\ \vec{u}_\varphi \end{aligned} \tag{2.13}$$

Here $\vec{u}_\zeta = \vec{B}/B$ is the unit vector tangent to the magnetic field line, while $\vec{u}_\eta$ is orthogonal to it and lies in the magnetic surface. The code uses physical components E_ψ, E_η, E_ζ of the electric field in Stix frame; they are related to the physical component in cylindrical coordinates by

$$\begin{aligned} E_X &= \frac{1}{N_\tau}\left\{\frac{\partial Z}{\partial\vartheta}E_\psi + \frac{\partial X}{\partial\vartheta}\left(E_\eta\cos\Theta - E_\zeta\sin\Theta\right)\right\} \\ E_Z &= \frac{1}{N_\tau}\left\{-\frac{\partial X}{\partial\vartheta}E_\psi + \frac{\partial Z}{\partial\vartheta}\left(E_\eta\cos\Theta - E_\zeta\sin\Theta\right)\right\} \\ E_\varphi &= -E_\eta\sin\Theta + E_\zeta\cos\Theta \end{aligned} \tag{2.14}$$

We will also need a basis for circularly polarised components perpendicular to $\vec{B}$. The correct definitions in toroidal geometry turn out to be

$$\vec{u}_\pm = \frac{1}{\sqrt{2}}\left\{e^{\mp i\tau}\left(\vec{u}_\psi \mp i\vec{u}_\eta\right)\right\} \qquad E_\pm = \frac{1}{\sqrt{2}}e^{\pm i\tau}\left(E_\psi \pm iE_\eta\right) \tag{2.15}$$

where

$$e^{\pm i\tau} = \frac{1}{\kappa N_\tau}\left(\frac{\partial Z}{\partial\vartheta} \mp i\cos\Theta\frac{\partial X}{\partial\vartheta}\right) \qquad \kappa^2 = 1 - \frac{\sin^2\Theta}{N_\tau^2}\left(\frac{\partial X}{\partial\vartheta}\right)^2 \tag{2.16}$$

The numerical approach based on the Galerkin weak–variational formulation requires only first order differential operators. To write them in Stix components it is convenient to introduce the notations

$$\begin{aligned} \partial_\psi &\equiv (\vec{u}_\psi\cdot\vec{\nabla}) = \frac{N_\tau}{J}\left(\frac{\partial}{\partial\psi} - \frac{G}{N_\tau^2}\frac{\partial}{\partial\vartheta}\right) \\ \partial_\eta &\equiv (\vec{u}_\eta\cdot\vec{\nabla}) = \frac{1}{N_\tau}\cos\Theta\frac{\partial}{\partial\vartheta} - \frac{1}{R}\sin\Theta\frac{\partial}{\partial\varphi} \\ \partial_\zeta &\equiv (\vec{u}_\zeta\cdot\vec{\nabla}) = \frac{1}{N_\tau}\sin\Theta\frac{\partial}{\partial\vartheta} + \frac{1}{R}\cos\Theta\frac{\partial}{\partial\varphi} \end{aligned} \tag{2.17}$$

a) – The gradient. If Φ is a scalar quantity, its gradient can be written:

$$\vec{\nabla}\Phi = \partial_\psi\Phi\,\vec{u}_\psi + \partial_\eta\Phi\,\vec{u}_\eta + \partial_\zeta\Phi\,\vec{u}_\zeta \tag{2.18}$$

b) – The divergence. The divergence of a vector field $\vec{E}$ is

$$\vec{\nabla}\cdot\vec{E} = \partial_\psi E_\psi + \nu_\psi E_\psi + \partial_\eta E_\eta + \nu_\eta E_\eta + \partial_\zeta E_\zeta + \nu_\zeta E_\zeta$$

$$\begin{aligned}
\nu_\psi &= \frac{N_\tau}{J}\left\{\frac{1}{R}\left(\frac{\partial R}{\partial\psi} - \frac{G}{N_\tau^2}\frac{\partial R}{\partial\vartheta}\right) + \frac{1}{N_\tau}\left(\frac{\partial N_\tau}{\partial\psi} - \frac{\partial}{\partial\vartheta}\left(\frac{G}{N_\tau}\right)\right)\right\} \\
\nu_\eta &= \frac{\cos\Theta}{N_\tau}\left(\frac{1}{R}\frac{\partial R}{\partial\vartheta} + \frac{1}{J}\frac{\partial J}{\partial\vartheta} - \frac{1}{N_\tau}\frac{\partial N_\tau}{\partial\vartheta}\right) - \frac{\sin\Theta}{N_\tau}\frac{\partial\Theta}{\partial\vartheta} \\
\nu_\zeta &= \frac{\sin\Theta}{N_\tau}\left(\frac{1}{R}\frac{\partial R}{\partial\vartheta} + \frac{1}{J}\frac{\partial J}{\partial\vartheta} - \frac{1}{N_\tau}\frac{\partial N_\tau}{\partial\vartheta}\right) + \frac{\cos\Theta}{N_\tau}\frac{\partial\Theta}{\partial\vartheta}
\end{aligned} \tag{2.19}$$

c) – The curl. The Stix components of $\vec{\nabla}\times\vec{E}$ are

$$(\vec{\nabla}\times\vec{E})_\psi = (\partial_\eta E_\zeta + \gamma_{\psi\zeta}E_\zeta) - (\partial_\zeta E_\eta + \gamma_{\psi\eta}E_\eta)$$

$$\gamma_{\psi\eta} = \frac{1}{N_\tau}\left\{\sin\Theta\,\frac{1}{R}\frac{\partial R}{\partial\vartheta} + \cos\Theta\,\frac{\partial\Theta}{\partial\vartheta}\right\}$$

$$\gamma_{\psi\zeta} = \frac{1}{N_\tau}\left\{\cos\Theta\,\frac{1}{R}\frac{\partial R}{\partial\vartheta} - \sin\Theta\,\frac{\partial\Theta}{\partial\vartheta}\right\}$$

$$(\vec{\nabla}\times\vec{E})_\eta = (\partial_\zeta E_\psi + \gamma_{\eta\psi}E_\psi) + \gamma_{\eta\eta}E_\eta - (\partial_\psi E_\zeta + \gamma_{\eta\zeta}E_\zeta)$$

$$\begin{aligned}
\gamma_{\eta\psi} &= \frac{\sin\Theta}{N_\tau}\left(\frac{1}{J}\frac{\partial J}{\partial\vartheta} - \frac{1}{N_\tau}\frac{\partial N_\tau}{\partial\vartheta}\right) \\
\gamma_{\eta\eta} &= \frac{N_\tau}{J}\left\{\cos\Theta\sin\Theta\left[\frac{1}{R}\left(\frac{\partial R}{\partial\psi} - \frac{G}{N_\tau^2}\frac{\partial R}{\partial\vartheta}\right)\right.\right. \\
&\qquad \left.\left. - \frac{1}{N_\tau}\left(\frac{\partial N_\tau}{\partial\psi} - \frac{G}{N_\tau^2}\frac{\partial N_\tau}{\partial\vartheta}\right) - \frac{\partial}{\partial\vartheta}\left(\frac{G}{N_\tau^2}\right)\right] + \left(\frac{\partial\Theta}{\partial\psi} - \frac{G}{N_\tau^2}\frac{\partial\Theta}{\partial\vartheta}\right)\right\} \\
\gamma_{\eta\zeta} &= \frac{N_\tau}{J}\left\{\cos^2\Theta\left[\frac{1}{R}\left(\frac{\partial R}{\partial\psi} - \frac{G}{N_\tau^2}\frac{\partial R}{\partial\vartheta}\right)\right]\right. \\
&\qquad \left. + \sin^2\Theta\left[\frac{1}{N_\tau}\left(\frac{\partial N_\tau}{\partial\psi} - \frac{G}{N_\tau^2}\frac{\partial N_\tau}{\partial\vartheta}\right) - \frac{\partial}{\partial\vartheta}\left(\frac{G}{N_\tau^2}\right)\right]\right\}
\end{aligned} \tag{(2.20)}$$

$$(\vec{\nabla}\times\vec{E})_\zeta = (\partial_\psi E_\eta + \gamma_{\zeta\eta}E_\eta) - (\partial_\eta E_\psi + \gamma_{\zeta\psi}E_\psi) + \gamma_{\zeta\zeta}E_\zeta$$

$$\begin{aligned}
\gamma_{\zeta\psi} &= \frac{\cos\Theta}{N_\tau}\left(\frac{1}{J}\frac{\partial J}{\partial\vartheta} - \frac{1}{N_\tau}\frac{\partial N_\tau}{\partial\vartheta}\right) \\
\gamma_{\zeta\eta} &= \frac{N_\tau}{J}\left\{\sin^2\Theta\frac{1}{R}\left(\frac{\partial R}{\partial\psi} - \frac{G}{N_\tau^2}\frac{\partial R}{\partial\vartheta}\right)\right. \\
&\qquad \left. + \cos^2\Theta\left[\frac{1}{N_\tau}\left(\frac{\partial N_\tau}{\partial\psi} - \frac{G}{N_\tau^2}\frac{\partial N_\tau}{\partial\vartheta}\right) - \frac{\partial}{\partial\vartheta}\left(\frac{G}{N_\tau^2}\right)\right]\right\} \\
\gamma_{\zeta\zeta} &= \frac{N_\tau}{J}\left\{\cos\Theta\sin\Theta\left[\frac{1}{N_\tau}\left(\frac{\partial N_\tau}{\partial\psi} - \frac{G}{N_\tau^2}\frac{\partial N_\tau}{\partial\vartheta}\right) - \frac{\partial}{\partial\vartheta}\left(\frac{G}{N_\tau^2}\right)\right.\right. \\
&\qquad \left.\left. - \frac{1}{R}\left(\frac{\partial R}{\partial\psi} - \frac{G}{N_\tau^2}\frac{\partial R}{\partial\vartheta}\right)\right] + \frac{1}{N_\tau}\left(\frac{\partial\Theta}{\partial\psi} - \frac{G}{N_\tau^2}\frac{\partial\Theta}{\partial\vartheta}\right)\right\}
\end{aligned}$$

3 – The wave equations.

3.1 – The Swanson–Colestock–Kashuba approximation. Maxwell equations in the plasma can be written

$$\vec{\nabla} \times \vec{\nabla} \times \vec{E} = \frac{\omega^2}{c^2} \left\{ \vec{E} + \frac{4\pi i}{\omega} \left(\vec{J}^P + \vec{J}^A \right) \right\} \tag{3.1}$$

where $\vec{J}^P$ is the h.f. plasma current, and $\vec{J}^A$ the antenna current. In the FLR approximation the plasma current can be split into

$$\vec{J}^P = \vec{J}^{(0)} + \vec{J}^{(2)} \tag{3.2}$$

where suffixes 0, 2, denote the order in the Larmor radius expansion. The linear plasma current has recently been derived in [15] directly in axisymmetric toroidal geometry. Our procedure, however, has been to start from the results of [10], in which Vlasov equation is solved in plane–stratified geometry, assuming that the vector form of $\vec{J}^P$ obtained there holds also in toroidal geometry, except for the evaluation of the orbit integrals along magnetic field lines. The two approaches should be essentially equivalent: in the small Larmor radius approximation the role of toroidicity in $\vec{J}^P$ is critical (i.e. it does not reduce to a trivial change of coordinates) only in the integrals along the magnetic field lines which describe to parallel dispersion. These integrals have been treated in a formal way in [10], and completely ignored in [15]. We will discuss them in section 6.1.

a) – The zero Larmor radius plasma current. The zero Larmor radius plasma current, combined for convenience with the vacuum displacement current, can be written

$$\begin{aligned} \vec{E} + \frac{4\pi i}{\omega} \vec{J}^{(0)} &= \hat{L}\, E_+ \vec{u}_+ + \hat{R}\, E_- \vec{u}_- + \hat{P}\, E_\zeta \vec{u}_\zeta \\ &= \left(\hat{S}\, E_\psi - i\hat{D}\, E_\eta \right) \vec{u}_\psi + \left(i\hat{D}\, E_\psi + \hat{S}\, E_\eta \right) \vec{u}_\eta + \hat{P}\, E_\zeta \vec{u}_\zeta \end{aligned} \tag{3.3}$$

where we have introduced the integral operators

$$\begin{aligned} \hat{L}E_+ &= E_+(\vec{r}) - \sum_\alpha \frac{\omega_{p\alpha}^2}{\omega^2} \int_{-\infty}^{+\infty} du \frac{e^{-u^2}}{\sqrt{\pi}} \left(-i\omega \int_{-\infty}^{t} dt' e^{i\int_{t'}^{t} (\omega - \Omega_g')\, d\tau} E_+' \right) \\ \hat{R}E_- &= E_-(\vec{r}) - \sum_\alpha \frac{\omega_{p\alpha}^2}{\omega^2} \int_{-\infty}^{+\infty} du \frac{e^{-u^2}}{\sqrt{\pi}} \left(-i\omega \int_{-\infty}^{t} dt' e^{i\int_{t'}^{t} (\omega + \Omega_g')\, d\tau} E_-' \right) \\ \hat{P}E_z &= E_z(\vec{r}) - \sum_\alpha \frac{\omega_{p\alpha}^2}{\omega^2} \int_{-\infty}^{+\infty} du \frac{e^{-u^2}}{\sqrt{\pi}} (2u^2) \left(-i\omega \int_{-\infty}^{t} dt' e^{i\omega(t-t')} E_z' \right) \end{aligned} \tag{3.4}$$

and

$$\hat{S} = \frac{1}{2} \left(\hat{R} + \hat{L} \right) \qquad \hat{D} = \frac{1}{2} \left(\hat{R} - \hat{L} \right) \tag{3.5}$$

The t'–integrations are along magnetic field lines, with, for each species

$$\vec{E}' = \vec{E}\left(\vec{r} - \int_{t'}^{t} (v_\parallel \vec{u}_\zeta)\, d\tau\right) \tag{3.6}$$

and $u = v_\parallel / v_{th}$, where $v_{th} = \sqrt{2T/m}$ is the thermal speed.

b) The ion FLR current. In the SCK approximation [8]–[9] only the terms resonant at $\omega = 2\Omega_{ci}$ are retained in the the FLR ion current. They can be written in vector form as [10]

$$\begin{aligned}\frac{4\pi i}{\omega}\vec{J}^{(2)} = \frac{c^2}{\omega^2}\underline{\underline{R}}\cdot\Bigg\{&\vec{\nabla}_\perp\left[\sigma^{(2)}\,\vec{\nabla}_\perp\cdot(\underline{\underline{R}}\cdot\vec{E}_\perp) - i\delta^{(2)}\,\vec{\nabla}_\perp\cdot\left(\vec{u}_\zeta\times\underline{\underline{R}}\cdot\vec{E}_\perp\right)\right]\\ &+\left(\vec{u}_\zeta\times\vec{\nabla}_\perp\right)\left[\sigma^{(2)}\,\vec{\nabla}_\perp\cdot\left(\vec{u}_\zeta\times\underline{\underline{R}}\cdot\vec{E}_\perp\right) + i\delta^{(2)}\,\vec{\nabla}_\perp\cdot(\underline{\underline{R}}\cdot\vec{E}_\perp)\right]\Bigg\}\end{aligned} \tag{3.7}$$

where

$$\hat{\sigma}_2 = \frac{\hat{\rho}_2 + \hat{\lambda}_2}{2} \qquad \hat{\delta}_2 = \frac{\hat{\rho}_2 - \hat{\lambda}_2}{2} \tag{3.8}$$

with

$$\begin{aligned}\hat{\lambda}^{(2)}\,E_+ &= \frac{1}{2}\sum_i \frac{\omega_{pi}^2}{\Omega_{ci}^2}\frac{v_{thi}^2}{c^2}\int_{-\infty}^{+\infty} du\,\frac{e^{-u^2}}{\sqrt{\pi}}\left(-i\omega\int_{-\infty}^{t} dt' e^{i\int_{t'}^{t}(\omega-2\Omega_g')\,d\tau}E_+'\right)\\ \hat{\rho}^{(2)}\,E_- &= \frac{1}{2}\sum_i \frac{\omega_{pi}^2}{\Omega_{ci}^2}\frac{v_{thi}^2}{c^2}\,\frac{\omega}{\omega+2\Omega_{ci}}\,E_-\end{aligned} \tag{3.9}$$

The matrix $\underline{\underline{R}} = \underline{\underline{R}}^{-1}$ is the reflection matrix with respect to the plane containing $\vec{B}_o$ and $\vec{\nabla}B_o$:

$$\underline{\underline{R}}\cdot\vec{E}_\perp = \vec{E}_\perp - 2\,\vec{u}_g\times\left(\vec{E}_\perp\times\vec{u}_g\right) \tag{3.10}$$

where $\vec{u}_g$ is a unit vector in the direction of the perpendicular part of the gradient of the static magnetic field. Neglecting terms of order $\Theta(\partial\Theta/\partial\psi)$ and $\Theta(\partial\Theta/\partial\vartheta)$, one finds

$$\begin{aligned}(\underline{\underline{R}}\cdot\vec{E}_\perp)_\psi &= C_2\,E_\psi + S_2\,E_\eta\\ (\underline{\underline{R}}\cdot\vec{E}_\perp)_\eta &= S_2\,E_\psi - C_2\,E_\eta\end{aligned} \tag{3.11}$$

where

$$C_2 = b_\psi^2 - b_\eta^2 \qquad S_2 = 2b_\psi b_\eta \tag{3.12}$$

with

$$b_\psi = \frac{1}{\kappa N_\tau}\frac{\partial Z}{\partial\vartheta} \qquad b_\eta = \frac{\cos\Theta}{\kappa N_\tau}\frac{\partial Z}{\partial\vartheta} \tag{3.13}$$

κ being defined in Eq. (2.16). Note that $\vec{J}^{(2)}$ is not rotationally invariant (the direction $\vec{\nabla} B_o$ being singled out), but satisfies Onsager relations, which are necessary for energy conservation in the absence of dissipative effects ($\mathrm{Im}\lambda^{(2)} = 0$).

Omitting FLR terms resonant at the fundamental is justified by the fact that they have to be compared with the zero–Larmor radius current which is also resonant at $\omega = \Omega_{ci}$, while near the first harmonic only the FLR part of the ion current is resonant. The superiority of the SCK model over the complete FLR model, however, is confirmed also by the analysis of the local dispersion relation. According to both the exact hot plasma dispersion relation and to the SCK model the root corresponding to the ion Bernstein wave diverges as $\omega \to \Omega_{ci}$ from above. By contrast, the full FLR dispersion relation predicts that this wave remains propagative below the ion cyclotron frequency and in the MHD frequency domain $\omega \ll \Omega_{ci}$ (but with a wavelength shorter than the ion Larmor radius, so that the conditions for the validity of the FLR expansion are violated). Near $\omega = \Omega_{ci}$, moreover, the power absorption predicted by the full FLR model is not positive–definite, in contrast with a general theorem [16] according to which in a Maxwellian plasma P_{abs} is always positive if terms explicitly proportional to the gradients of the equilibrium quantities are neglected. In the SCK model the power absorbed by the ions is always positive, as it should.

c) The electron FLR current. The SCK model must be completed by taking into account the FLR electron current, which consists of two terms,

$$\frac{4\pi i}{\omega}\vec{J}_e^{(2)} = \frac{4\pi i}{\omega}\left(\vec{J}_{TT}^{(2)} + \vec{J}_{MX}^{(2)}\right) \tag{3.14}$$

respectively associated with TTMP damping and mixing TTMP with ELD:

$$\begin{aligned}
\frac{4\pi i}{\omega}\vec{J}_{TT}^{(2)} &= -2\frac{c^2}{\omega^2}\vec{\nabla}_\perp \times \left[\hat{\lambda}^{(o)}(\vec{\nabla}_\perp \times \vec{E}_\perp)\right] \\
\frac{4\pi i}{\omega}\vec{J}_{MX}^{(2)} &= i\frac{c^2}{\omega^2}\Big\{\vec{\nabla}_\perp \times \left[\xi^{(o)}\left(\vec{u}_\zeta \cdot \vec{\nabla}\right) E_\zeta \vec{u}_\zeta\right] + \\
&\qquad + \vec{u}_\zeta\left(\vec{u}_\zeta \cdot \vec{\nabla}\right)\left[\xi^{(o)}\left(\vec{u}_\zeta \cdot \vec{\nabla}_\perp \vec{E}_\perp\right)\right]\Big\}
\end{aligned} \tag{3.15}$$

with

$$\begin{aligned}
\hat{\lambda}^{(o)}\vec{E} &= \frac{1}{2}\frac{\omega_{pe}^2}{\Omega_{ce}^2}\frac{v_{the}^2}{c^2}\int_{-\infty}^{+\infty} du\,\frac{e^{-u^2}}{\sqrt{\pi}}\left(-i\omega\int_{-\infty}^{t} dt' e^{i\omega(t-t')}\vec{E}'\right) \\
\hat{\xi}^{(o)}E_j &= \frac{1}{2}\frac{\omega_{pe}^2}{\omega\Omega_{ce}}\frac{v_{the}^2}{c^2}\int_{-\infty}^{+\infty} du\,\frac{e^{-u^2}}{\sqrt{\pi}}\left(\omega^2\frac{\partial}{\partial\omega}\int_{-\infty}^{t} dt' e^{i\omega(t-t')}E_j'\right)
\end{aligned} \tag{3.16}$$

In addition, the electrons contribute the small quantities

$$\hat{\lambda}_e^2 E_+ = \frac{1}{2}\frac{\omega_{pe}^2}{\Omega_{ce}^2}\frac{v_{the}^2}{c^2}\frac{\omega}{\omega + 2\Omega_{ce}}E_+ \qquad \hat{\rho}_e^2 E_- = \frac{1}{2}\frac{\omega_{pe}^2}{\Omega_{ce}^2}\frac{v_{the}^2}{c^2}\frac{\omega}{\omega - 2\Omega_{ce}}E_- \tag{3.17}$$

to $\hat{\lambda}^2$, $\hat{\rho}^2$, respectively.

3.4 – Boundary conditions. In TORIC the numerical integration is continued up to the wall. The system of equation is therefore completed by boundary conditions at the wall and at the antenna. The wall is assumed perfectly conducting, so that

$$E_\eta(a) = E_\zeta(a) = 0 \tag{3.18}$$

The antenna is modelled by a current sheath on the magnetic surface $\psi = \psi_A$,

$$\vec{J}^A = \frac{N_\tau}{J} J^s(\vartheta, \varphi)\, \delta(\psi - \psi_A)\, \vec{u}_A \tag{3.19}$$

where J^s is a line current density (A/m), and

$$\vec{u}_A = \cos(\Theta - \alpha)\vec{u}_\eta + \sin(\Theta - \alpha)\vec{u}_\zeta \tag{3.20}$$

for conductors inclined by an angle α to the poloidal direction. The jump conditions for the tangential magnetic field are then

$$\begin{aligned} \frac{c}{\omega}\left[\vec{\nabla}\times\vec{E})_\zeta\right]_{\psi_A} &= +\frac{4\pi i}{c} J^s \cos(\Theta - \alpha) \\ \frac{c}{\omega}\left[\vec{\nabla}\times\vec{E})_\eta\right]_{\psi_A} &= -\frac{4\pi i}{c} J^s \sin(\Theta - \alpha) \end{aligned} \tag{3.21}$$

(in practice, only the case $\alpha = \Theta$ is implemented, since antenna currents parallel to $\vec{B}_o$ can excite short wavelength waves in the plasma periphery, whose numerical resolution in toroidal geometry is nearly prohibitive). In addition, we must explicitly require the continuity of the parallel electric field across the surface of the antenna, $\psi = \psi_A$,

$$[E_\eta]_{\psi_A} = 0 \qquad\qquad [E_\zeta]_{\psi_A} = 0 \tag{3.22}$$

Finally, a Faraday shield with blades inclined by an angle β with respect to the equatorial plane is simulated by imposing

$$-\sin(\Theta - \beta)\, E_\eta + \cos(\Theta - \beta)\, E_\zeta = 0 \tag{3.23}$$

on the magnetic surface in which the screen lies. Again only the case $\beta = \Theta$ is implemented.

4 - Weak–variational formulation.

4.1 – The variational integral. The first step towards the numerical solution of the wave equations is to put them into the Galerkin weak–variational form by multiplying Eq. (3.1) scalarly with an arbitrary vector function $\vec{F}$ belonging to a suitable test function space (defined so that $\vec{F}$ satisfies the same boundary conditions as $\vec{E}$), and integrating over the whole plasma volume:

$$\int dV\, \vec{F}^* \cdot \left\{ -\frac{c^2}{\omega^2} \vec{\nabla} \times \vec{\nabla} \times \vec{E} + \vec{E} + \frac{4\pi i}{\omega} \left(\vec{J}^P + \vec{J}^A \right) \right\} = 0 \tag{4.1}$$

(In the code all lengths are measured in units of c/ω, and the variational integral is dimensionless). The second order operators are then eliminated by part integration, and the resulting equation will be written

$$\mathcal{Q}_{curl} + \mathcal{Q}_{pl} = \mathcal{Q}_{ant} + \mathcal{S}_{curl} + \mathcal{S}_{pl} \tag{4.2}$$

where $\mathcal{Q}$, $\mathcal{S}$ denote volume and surface integrals, respectively. The latter extend over the plasma surface and any other discontinuity surface; the surface integrals on the wall vanish, however, because of the boundary condition at an ideal conductor. Moreover, $\mathcal{Q}_{pl}$ and $\mathcal{S}_{pl}$ will be further split into zero and second order terms in the Larmor radius expansion,

$$\mathcal{Q}_{pl} = \mathcal{Q}_{pl}^{(0)} + \mathcal{Q}_{pl}^{(2)} \qquad \mathcal{S}_{pl} = \mathcal{S}_{pl}^{(0)} + \mathcal{S}_{pl}^{(2)} \tag{4.3}$$

For simplicity, the vacuum displacement current will be collected with the zero Larmor radius plasma current, as it is done when defining the dielectric tensor of the uniform plasma.

We now list all the terms in Eq. (4.2) in turn; the surface terms are to be evaluated at the "plasma surface", which is a magnetic surface. The volume and surface elements for the integrations are then

$$dV = RJ\, d\psi\, d\vartheta \qquad d\vec{S} = \pm RN_\tau\, d\vartheta\, \vec{u}_\psi \tag{4.4}$$

where in $d\vec{S}$ the positive sign is for a surface oriented from the plasma toward the vacuum.

a) – The vacuum contribution. The identity

$$\vec{F}^* \cdot \vec{\nabla} \times \vec{\nabla} \times \vec{E} = \vec{\nabla} \times \vec{F}^* \cdot \vec{\nabla} \times \vec{E} - \vec{\nabla} \cdot \left(\vec{F}^* \times (\vec{\nabla} \times \vec{E}) \right) \tag{4.5}$$

gives for the vacuum contributions (excluding the displacement current)

$$\mathcal{Q}_{curl} = -\frac{c^2}{\omega^2} \int \int RJ \left(\vec{\nabla} \times \vec{F}^* \cdot \vec{\nabla} \times \vec{E} \right) d\psi\, d\vartheta \tag{4.6}$$

and

$$\mathcal{S}_{curl} = -\frac{c^2}{\omega^2} \int RN_\tau \left\{ \vec{u}_\psi \cdot \left(\vec{F}^* \times (\vec{\nabla} \times \vec{E}) \right) \right\} d\vartheta \tag{4.7}$$

respectively.

b) – The zero Larmor radius plasma current. The contribution from the zero Larmor radius plasma current, including the vacuum displacement current, is

$$\begin{aligned}\mathcal{Q}_{pl}^{(0)} &= \iint RJ\left\{F_+^*\,\hat{L}\,E_+ + F_-^*\,\hat{R}\,E_- + F_\zeta^*\,\hat{P}\,E_\zeta\right\}d\psi\,d\vartheta \\ &= \iint RJ\left\{F_\psi^*\left(\hat{S}\,E_\psi - i\hat{D}\,E_\eta\right) + F_\eta^*\left(i\hat{D}\,E_\psi + \hat{S}\,E_\eta\right) + F_\zeta^*\,\hat{P}\,E_\zeta\right\}d\psi\,d\vartheta\end{aligned} \tag{4.8}$$

c) – The ion FLR current. After integration by parts, the contribution of the FLR part of the ion current to the variational integral becomes

$$\begin{aligned}\mathcal{Q}_{pl}^{(2,i)} &= -\frac{c^2}{\omega^2}\iint RJ\Big\{\vec{\nabla}_\perp\cdot(\underline{\underline{R}}\cdot\vec{F}_\perp^*)\left[\hat{\sigma}^{(2)}\vec{\nabla}_\perp\cdot(\underline{\underline{R}}\cdot\vec{E}'_\perp) - i\hat{\delta}^{(2)}\vec{\nabla}_\perp\cdot(\vec{u}_\zeta\times\underline{\underline{R}}\cdot\vec{E}'_\perp)\right] \\ &\quad + \vec{\nabla}_\perp\cdot(\vec{u}_\zeta\times\underline{\underline{R}}\cdot\vec{F}_\perp^*)\left[\hat{\sigma}^{(2)}\vec{\nabla}_\perp\cdot(\vec{u}_\zeta\times\underline{\underline{R}}\cdot\vec{E}'_\perp) + i\hat{\delta}^{(2)}\vec{\nabla}_\perp\cdot(\underline{\underline{R}}\cdot\vec{E}'_\perp)\right]\Big\}d\psi\,d\vartheta \\ &= -2\frac{c^2}{\omega^2}\iint RJ\Big\{(\partial_+F_+)^*\,\hat{\lambda}^{(2)}\,(\partial_+E_+) + (\partial_-F_-)^*\,\hat{\rho}^{(2)}\,(\partial_-E_-)\Big\}d\psi\,d\vartheta\end{aligned} \tag{4.9}$$

and

$$\begin{aligned}\mathcal{S}_{pl}^{(2,i)} = -\frac{c^2}{\omega^2}\int RN_\tau\,\vec{u}_\psi\cdot\Big\{&\underline{\underline{R}}\cdot\vec{F}_\perp^*\left[\hat{\sigma}_2\vec{\nabla}_\perp\cdot(\underline{\underline{R}}\cdot\vec{E}'_\perp) - i\hat{\delta}_2\vec{\nabla}_\perp\cdot(\vec{u}_\zeta\times\underline{\underline{R}}\cdot\vec{E}'_\perp)\right] \\ &+\underline{\underline{R}}\cdot\vec{F}_\perp^*\times\left[\hat{\sigma}_2\vec{\nabla}_\perp\cdot(\vec{u}_\zeta\times\underline{\underline{R}}\cdot\vec{E}'_\perp) + i\hat{\delta}_2\vec{\nabla}_\perp\cdot(\underline{\underline{R}}\cdot\vec{E}'_\perp)\right]\Big\}d\vartheta\end{aligned} \tag{4.10}$$

In writing the last form of $\mathcal{Q}_{pl}^{(2,i)}$, neglecting terms of order $\Theta(\partial\Theta/\partial\psi)$ and $\Theta(\partial\Theta/\partial\vartheta)$, we have defined

$$\begin{aligned}(\partial_\pm E_\pm) &\equiv \frac{1}{2}\left\{\vec{\nabla}_\perp\cdot(\underline{\underline{R}}\cdot\vec{E}_\perp) \pm i\vec{\nabla}_\perp\cdot(\vec{u}_\zeta\times\underline{\underline{R}}\cdot\vec{E}_\perp)\right\} \\ &\simeq \frac{1}{2}\left[(\partial_\psi+\nu_\psi) \pm i(\partial_\eta+\nu_\eta)\right]\left\{e^{\pm 2i\tau}\,(E_\psi \pm iE_\eta)\right\}\end{aligned} \tag{4.11}$$

and we have used the fact that (cfr. Eq. (2.14))

$$C_2 \mp iS_2 = \frac{1}{\kappa^2 N_\tau^2}\left(\frac{\partial Z}{\partial\vartheta} \mp i\cos\Theta\frac{\partial X}{\partial\vartheta}\right)^2 = e^{\pm 2i\tau} \tag{4.12}$$

d) – The electron FLR current. After integration by parts, the volume contributions of the FLR part of the electron current to the variational integral become

$$\begin{aligned}
\mathcal{Q}^{(2)}_{TT} &= -2\frac{c^2}{\omega^2}\int\int RJ\left\{(\vec{\nabla}_\perp \times \vec{F}_\perp)^*\,\hat{\lambda}^{(o)}\,(\vec{\nabla}_\perp \times \vec{E}_\perp)\right\} d\psi\, d\vartheta \\
\mathcal{Q}^{(2)}_{MX} &= i\,\frac{c^2}{\omega^2}\int\int RJ\Big\{\left[\vec{u}_\zeta \cdot \left(\vec{\nabla}_\perp \times \vec{F}_\perp\right)\right]^*\,\hat{\xi}^{(o)}\,(\partial_\zeta E_\zeta) \\
&\qquad - (\partial_\zeta F_\zeta)^*\,\hat{\xi}^{(o)}\left[\vec{u}_\zeta \cdot \left(\vec{\nabla}_\perp \times \vec{E}_\perp\right)\right]\Big\}
\end{aligned} \tag{4.13}$$

while the surface contributions are

$$\begin{aligned}
\mathcal{S}^{(2)}_{TT} &= -2\frac{c^2}{\omega^2}\int RN_\tau\,\vec{u}_\psi \cdot \left\{\vec{F}^*_\perp \times \left[\hat{\lambda}^{(o)}\,(\vec{\nabla}_\perp \times \vec{E}_\perp)\right]\right\} d\vartheta \\
\mathcal{S}^{(2)}_{MX} &= i\,\frac{c^2}{\omega^2}\int RN_\tau \left\{\vec{F}^*_\perp \times \left[\hat{\xi}^{(o)}\,(\partial_\zeta E_\zeta)\,\vec{u}_\zeta\right] \cdot \vec{u}_\psi\right\}
\end{aligned} \tag{4.14}$$

respectively.

4.2 – Boundary conditions at the plasma edge. Let the plasma be bounded by the magnetic surface $\psi = \psi_s$, on which moreover we allow for given surface currents $\vec{J}_s$ flowing in thin external conductors, to simulate for example the Faraday screen. To handle such a discontinuity, surface contributions from the inner (plasma side, suffix p) and outer (vacuum side, suffix v) face of the boundary surface must be added to the variational integral. The contribution from the inner side is of the form

$$\begin{aligned}
\mathcal{S}_p = -\frac{c^2}{\omega^2}\int RN_\tau\Big\{ & F^*_\psi\,\mathcal{L}^{(2)}_\psi(\vec{E}^{\,p}) \\
& + F^*_\eta\left[(\vec{\nabla}\times\vec{E})^p_\zeta + \mathcal{L}^{(2)}_\eta(\vec{E}^{\,p})\right] - F^*_\eta(\vec{\nabla}\times\vec{E})^p_\eta\Big\}\, d\vartheta
\end{aligned} \tag{4.15}$$

where we have singled out the contribution from the vacuum part, Eq. (4.7), while those from the FLR plasma current, Eqs. (4.10) and (4.14), have been put together in the first order vector differential operator $\vec{\mathcal{L}}^{(2)}$, whose parallel component vanishes identically. The contribution from the outer side of the boundary is

$$\mathcal{S}_v = \frac{c^2}{\omega^2}\int RN_\tau\left\{F^*_\eta(\vec{\nabla}\times\vec{E})^v_\zeta - F^*_\eta(\vec{\nabla}\times\vec{E})^v_\eta\right\} d\vartheta \tag{4.16}$$

We recall that up to common a numerical factor the vacuum and FLR contributions represent the electromagnetic and kinetic part of the power flux through the surface,

respectively. The continuity of this flux at the surface imposes the boundary conditions [17]

$$\begin{aligned} &\mathcal{L}_{\psi}^{(2)}(\vec{E}^{p}) = 0 \\ &(\vec{\nabla}\times\vec{E})_{\zeta}^{p} - (\vec{\nabla}\times\vec{E})_{\zeta}^{v} + \mathcal{L}_{\eta}^{(2)}(\vec{E}^{p}) = \frac{4\pi i\omega}{c^2}\left(J_{\eta}^{s} + J_{\eta}^{D}\right) \\ &(\vec{\nabla}\times\vec{E})_{\eta}^{p} - (\vec{\nabla}\times\vec{E})_{\eta}^{v} = -\frac{4\pi i\omega}{c^2} J_{\zeta}^{s} \end{aligned} \tag{4.17}$$

where J_{η}^{D} is a surface h.f. diamagnetic currents of amplitude such that

$$\frac{4\pi i\omega}{c^2} J_{\eta}^{D} = \mathcal{L}_{\eta}^{(2)}(\vec{E}^{p}) \tag{4.18}$$

As a consequence, the surface contributions to the variational integral at $\psi = \psi_s$ can be expressed in terms of the external currents only,

$$\mathcal{S}_p + \mathcal{S}_v = \frac{4\pi i}{\omega}\int RN_{\tau}\left\{F_{\eta}^{*} J_{\zeta}^{s} - F_{\zeta}^{*} J_{\eta}^{s}\right\} d\vartheta \tag{4.19}$$

The FLR surface terms, therefore, need not to be coded explicitly.

4.3 – The antenna contribution. If a small but finite thickness $\Delta\psi$ is attributed to the antenna, its contribution to the variational integral can be written

$$\mathcal{Q}_{ant} = -\frac{4\pi i}{\omega}\Delta\psi \iint_{\psi_A} RN_{\tau}\, J^{s}(\vartheta,\varphi)\left\{F_{\eta}^{*}\cos(\Theta-\alpha) + F_{\zeta}^{*}\sin(\Theta-\alpha)\right\} d\vartheta\, d\varphi \tag{4.20}$$

It is more convenient, however, to model the antenna by a surface current flowing in an infinitely thin conductor. If the antenna is located in vacuum, then, the tangent magnetic field is discontinuous at $\psi = \psi_A$, and from each side of this surface we get surface contributions to the variational integral such as

$$[\mathcal{S}_{curl}]_{\psi_A} = \frac{c^2}{\omega^2}\int_{\psi=\psi_A} RN_{\tau}\left\{F_{\eta}^{*}\left[(\vec{\nabla}\times\vec{E})_{\zeta}\right]_{\psi_A} - F_{\zeta}^{*}\left[(\vec{\nabla}\times\vec{E})_{\eta}\right]_{\psi_A}\right\} d\vartheta\, d\varphi \tag{4.21}$$

where $[\mathcal{S}]_{\psi_A} = \mathcal{S}^{+} - \mathcal{S}^{-}$, and superscripts $+$ $(-)$ refers to the outer (inner) side of the conductor, respectively. The jump conditions (3.17) for the tangential magnetic field are therefore equivalent to the condition

$$[\mathcal{S}_{curl}]_{\psi_A} = \mathcal{Q}_{ant} \tag{4.22}$$

5 – The spectral Ansatz.

We assume a solution of the form

$$E_\alpha = e^{in_\varphi \varphi} \sum_{m=-\infty}^{+\infty} E_\alpha^m(n_\varphi;\psi)\, e^{im\vartheta} \tag{5.1}$$

Because of axisymmetry there is no coupling between different n_φ components; in the following, the argument n_φ will usually be omitted.

5.1 – The differential operators in the spectral representation. With lengths in units of c/ω, the components of $\operatorname{div} E$ and $\operatorname{curl} E$ for the field (4.3) are:

$$\vec{\nabla}\cdot\vec{E} = \sum_m e^{im\vartheta}\left\{\frac{N_\tau}{J}\frac{dE_\psi^m}{d\psi} + \nu_\psi E_\psi^m + (i\,k_\eta + \nu_\eta)\,E_\eta^m + (i\,k_\zeta + \nu_\zeta)\,E_\zeta^m\right\} \tag{5.2}$$

and

$$\begin{aligned}
\vec{\nabla}\times\vec{E})_\psi &= \sum_m e^{im\vartheta}\left\{(ik_\eta^m + \gamma_{\psi\zeta})E_\zeta^m - (ik_\zeta^m + \gamma_{\psi\eta})E_\eta^m\right\} \\
\vec{\nabla}\times\vec{E})_\eta &= \sum_m e^{im\vartheta}\left\{(ik_\zeta^m + \gamma_{\eta\psi})E_\psi^m + \gamma_{\eta\eta}E_\eta^m\right. \\
&\qquad \left. - \left[\frac{N_\tau}{J}\left(\frac{dE_\zeta^m}{d\psi} - im\frac{G}{N_\tau^2}E_\zeta^m\right) + \gamma_{\eta\zeta}E_\zeta^m\right]\right\} \\
\vec{\nabla}\times\vec{E})_\zeta &= \sum_m e^{im\vartheta}\left\{\left[\frac{N_\tau}{J}\left(\frac{dE_\eta^m}{d\psi} - im\frac{G}{N_\tau^2}E_\eta^m\right) + \gamma_{\zeta\eta}E_\eta^m\right] -\right. \\
&\qquad \left. - (ik_\eta^m + \gamma_{\zeta\psi})E_\psi^m + \gamma_{\zeta\zeta}E_\zeta^m\right\}
\end{aligned} \tag{5.3}$$

where

$$\begin{aligned}
k_\eta^m &= \frac{m}{N_\tau}\cos\Theta - \frac{n_\varphi}{R}\sin\Theta \\
k_\zeta^m &= \frac{m}{N_\tau}\sin\Theta + \frac{n_\varphi}{R}\cos\Theta
\end{aligned} \tag{5.4}$$

In particular, k_ζ can be regarded as the local parallel component of the wavevector of the Fourier component m.

It is convenient to rewrite the divergence compactly as

$$\vec{\nabla}\cdot\vec{E} = \sum_{m=-\infty}^{+\infty} e^{im\vartheta}\sum_\beta\left\{\tilde{S}_\beta^{(3)}\frac{dE_\beta^m}{d\psi} + \left(m\tilde{S}_\beta^{(2)} + \tilde{S}_\beta^{(1)}\right)E_\beta^m\right\} \tag{5.5}$$

with

$$\begin{array}{lll}
\tilde{S}_\psi^{(1)} = \nu_\psi & \tilde{S}_\psi^{(2)} = -i\dfrac{G}{JN_\tau} & \tilde{S}_\psi^{(3)} = \dfrac{N_\tau}{J} \\
\tilde{S}_\eta^{(1)} = \nu_\eta - i\dfrac{n_\varphi}{R}\sin\Theta & \tilde{S}_\eta^{(2)} = i\dfrac{\cos\Theta}{N_\tau} & \tilde{S}_\eta^{(3)} = 0 \\
\tilde{S}_\zeta^{(1)} = \nu_\zeta + i\dfrac{n_\varphi}{R}\cos\Theta & \tilde{S}_\zeta^{(2)} = i\dfrac{\sin\Theta}{N_\tau} & \tilde{S}_\zeta^{(3)} = 0
\end{array} \tag{5.6}$$

Similarly the curl can be written compactly as

$$\vec{\nabla} \times \vec{E})_\alpha = \sum_{m=-\infty}^{+\infty} e^{im\vartheta} \sum_\beta \left\{ \tilde{R}^{(3)}_{\alpha\beta} \frac{dE^m_\beta}{d\psi} + \left(m\tilde{R}^{(2)}_{\alpha\beta} + \tilde{R}^{(1)}_{\alpha\beta} \right) E^m_\beta \right\} \tag{5.7}$$

where

$$\begin{array}{lll}
\tilde{R}^{(1)}_{\psi\psi} = 0 & \tilde{R}^{(2)}_{\psi\psi} = 0 & \tilde{R}^{(3)}_{\psi\psi} = 0 \\
\tilde{R}^{(1)}_{\psi\eta} = -i\frac{n_\varphi}{R}\cos\Theta - \gamma_{\psi\eta} & \tilde{R}^{(2)}_{\psi\eta} = -i\frac{1}{N_\tau}\sin\Theta & \tilde{R}^{(3)}_{\psi\eta} = 0 \\
\tilde{R}^{(1)}_{\psi\zeta} = -i\frac{n_\varphi}{R}\sin\Theta + \gamma_{\psi\zeta} & \tilde{R}^{(2)}_{\psi\zeta} = +i\frac{1}{N_\tau}\cos\Theta & \tilde{R}^{(3)}_{\psi\zeta} = 0 \\
\tilde{R}^{(1)}_{\eta\psi} = i\frac{n_\varphi}{R}\cos\Theta + \gamma_{\eta\psi} & \tilde{R}^{(2)}_{\eta\psi} = i\frac{1}{N_\tau}\sin\Theta & \tilde{R}^{(3)}_{\eta\psi} = 0 \\
\tilde{R}^{(1)}_{\eta\eta} = \gamma_{\eta\eta} & \tilde{R}^{(2)}_{\eta\eta} = 0 & \tilde{R}^{(3)}_{\eta\eta} = 0 \\
\tilde{R}^{(1)}_{\eta\zeta} = -\gamma_{\eta\zeta} & \tilde{R}^{(2)}_{\eta\zeta} = i\frac{G}{JN_\tau} & \tilde{R}^{(3)}_{\eta\zeta} = -\frac{N_\tau}{J} \\
\tilde{R}^{(1)}_{\zeta\psi} = i\frac{n_\varphi}{R}\sin\Theta - \gamma_{\zeta\psi} & \tilde{R}^{(2)}_{\zeta\psi} = -i\frac{1}{N_\tau}\cos\Theta & \tilde{R}^{(3)}_{\zeta\psi} = 0 \\
\tilde{R}^{(1)}_{\zeta\eta} = \gamma_{\zeta\eta} & \tilde{R}^{(2)}_{\zeta\eta} = -i\frac{G}{JN_\tau} & \tilde{R}^{(3)}_{\zeta\eta} = \frac{N_\tau}{J} \\
\tilde{R}^{(1)}_{\zeta\zeta} = \gamma_{\zeta\zeta} & \tilde{R}^{(2)}_{\zeta\zeta} = 0 & \tilde{R}^{(3)}_{\zeta\zeta} = 0
\end{array} \tag{5.8}$$

Finally, the operator in the ion FLR current has the spectral representation

$$\begin{aligned}
&\frac{1}{2}\left\{ \vec{\nabla}_\perp \cdot (\underline{\underline{R}} \cdot \vec{E}_\perp) \pm i\vec{\nabla}_\perp \cdot (\vec{u}_\zeta \times \underline{\underline{R}} \cdot \vec{E}_\perp) \right\} \\
&\quad = \sum_\alpha \sum_m e^{im\vartheta} \left\{ \tilde{T}^{(3)}_\pm \left(\frac{\partial E_\psi}{\partial\psi} \pm i\frac{\partial E_\eta}{\partial\psi} \right) + \left(mT^{(2)}_\pm + T^{(1)}_\pm \right) (E_\psi \pm iE_\eta) \right\}
\end{aligned} \tag{5.9}$$

where

$$\begin{aligned}
\tilde{T}^{(3)}_\pm &= \frac{1}{2}\frac{N_\tau}{J}\left[\frac{1}{\kappa N_\tau}\left(\frac{\partial Z}{\partial\vartheta} \mp i\cos\Theta\frac{\partial X}{\partial\vartheta} \right) \right]^2 \\
\tilde{T}^{(2)}_\pm &= \frac{1}{2}\left(S^{(2)}_\psi \pm iS^{(2)}_\eta \right)\left[\frac{1}{\kappa N_\tau}\left(\frac{\partial Z}{\partial\vartheta} \mp i\cos\Theta\frac{\partial X}{\partial\vartheta} \right) \right]^2 \\
\tilde{T}^{(1)}_\pm &= \frac{1}{2}\left\{ \left(S^{(1)}_\psi \pm iS^{(1)}_\eta \right)\left[\frac{1}{\kappa N_\tau}\left(\frac{\partial Z}{\partial\vartheta} \mp i\cos\Theta\frac{\partial X}{\partial\vartheta} \right) \right]^2 \right. \\
&\quad \left. + \left[\frac{N_\tau}{J}\left(\frac{\partial}{\partial\psi} - \frac{G}{N_\tau^2}\frac{\partial}{\partial\vartheta} \right) \pm i\frac{\cos\Theta}{N_\tau}\frac{\partial}{\partial\vartheta} \right]\left[\frac{1}{\kappa N_\tau}\left(\frac{\partial Z}{\partial\vartheta} \mp i\cos\Theta\frac{\partial X}{\partial\vartheta} \right) \right]^2 \right\}
\end{aligned} \tag{5.10}$$

The coefficients $\tilde{S}^{(k)}_\beta$, $\tilde{R}^{(k)}_{\alpha\beta}$ and $\tilde{T}^{(k)}_\pm$ are functions of the poloidal angle ϑ, but do not depend on m.

5.2 – Construction of the variational integral. Expanding also the test functions $\vec{F}$ in Fourier modes, the variational integral takes the form

$$\begin{aligned}
&\sum_m \sum_{m'} \int\int RJ\, e^{i(m'-m)\vartheta} \left(\vec{F}^{(m)*}(\psi)\cdot \underline{\underline{\mathcal{Q}}}^{\mathrm{op}}\cdot \vec{E}^{(m')}(\psi)\right) d\vartheta\, d\psi \\
&\quad = \frac{4\pi i}{\omega}\sum_m \int\int RJ\, e^{-im\vartheta}\left(\vec{F}^{(m)*}(\psi)\cdot \vec{J}_A(n_\varphi,\psi,\vartheta)\right) d\vartheta\, d\psi \qquad (5.11)\\
&\quad + \sum_{\psi_s}\sum_m\sum_{m'} \int RN_\tau\, e^{i(m'-m)\vartheta}\left(\vec{F}^{(m)*}(\psi_s)\cdot \underline{\underline{\mathcal{S}}}^{\mathrm{op}}\cdot \vec{E}^{(m')}(\psi_s)\right) d\vartheta
\end{aligned}$$

On the r.h. side the first term is a weighted poloidal Fourier transform of the antenna current; the last term extends over the plasma surface and any other discontinuity surface, e.g. the antenna and Faraday shield locations.

The operator $\mathcal{Q}^{\mathrm{op}}$ has the form

$$\begin{aligned}
&\vec{F}^{(m)*}(\psi)\cdot \underline{\underline{\mathcal{Q}}}^{\mathrm{op}}\cdot \vec{E}^{(m')}(\psi) = \\
&\sum_\alpha\sum_\beta \left\{ \frac{dF_\alpha^{m*}}{d\psi}\,\Gamma_{\alpha\beta}(m,2;m',2)\,\frac{dE_\beta^{m'}}{d\psi} + \frac{dF_\alpha^{m*}}{d\psi}\,\Gamma_{\alpha\beta}(m,2;m',1)\,E_\beta^{m'} \right. \qquad (5.12)\\
&\qquad \left. + F_\alpha^{m*}\,\Gamma_{\alpha\beta}(m,1;m',2)\,\frac{dE_\beta^{m'}}{d\psi} + F_\alpha^{m*}\,\Gamma_{\alpha\beta}(m,1;m',1)\,E_\beta^{m'} \right\}
\end{aligned}$$

The operator $\mathcal{S}^{\mathrm{op}}$ has a similar representation, except that it does not contain derivatives of $\vec{F}^*$. According to the remarks made in section 4.2, however, the explicit form of this operator is not needed. We now list the contributions to $\mathcal{Q}^{\mathrm{op}}$.

a) – Contribution from the curl *operator.* The contributions from the vacuum part of Maxwell equations are

$$\begin{aligned}
\Gamma^v_{\alpha\beta}(m,1;m',1) &= \sum_\gamma \left(m\tilde{R}^{(2)}_{\gamma\alpha} + \tilde{R}^{(1)}_{\gamma\alpha}\right)^* \cdot \left(m'\tilde{R}^{(2)}_{\gamma\beta} + \tilde{R}^{(1)}_{\gamma\beta}\right)\\
\Gamma^v_{\alpha\beta}(m,2;m',1) &= \sum_\gamma \left(\tilde{R}^{(3)}_{\gamma\alpha}\right)^* \cdot \left(m'\tilde{R}^{(2)}_{\gamma\beta} + \tilde{R}^{(1)}_{\gamma\beta}\right) \qquad (5.13)\\
\Gamma^v_{\alpha\beta}(m,1;m',2) &= \sum_\gamma \left(m\tilde{R}^{(2)}_{\gamma\alpha} + \tilde{R}^{(1)}_{\gamma\alpha}\right)^* \cdot \left(\tilde{R}^{(3)}_{\gamma\beta}\right)\\
\Gamma^v_{\alpha\beta}(m,2;m',2) &= \sum_\gamma \left(\tilde{R}^{(3)}_{\gamma\alpha}\right)^* \cdot \left(\tilde{R}^{(3)}_{\gamma\beta}\right)
\end{aligned}$$

b) – Contribution from the zero Larmor radius plasma current. The contributions of the zero Larmor radius plasma currents are:

$$\begin{aligned}
\Gamma^0_{\psi\psi}(m,1;m',1) &= \Gamma_{\eta\eta}(m,1;m',1) = -\hat{S}(\psi,\vartheta;k_\zeta^{m'}) \\
\Gamma^0_{\psi\eta}(m,1;m',1) &= -\Gamma^0_{\eta\psi}(m,1;m',1) = i\hat{D}(\psi,\vartheta;k_\zeta^{m'}) \\
\Gamma^0_{\zeta\zeta}(m,1;m',1) &= -\hat{P}(\psi,\vartheta;k_\zeta^{m'})
\end{aligned} \tag{5.14}$$

with

$$\begin{aligned}
\hat{L} &= 1 - \sum_\alpha \frac{\omega_{p\alpha}^2}{\omega^2}\left(-x_{o\alpha}\tilde{Z}(x_{1\alpha})\right) \simeq 1 - \sum_i \frac{\omega_{pi}^2}{\omega^2}\left(\frac{\omega}{\Omega_{ci}} - x_{o,i}\tilde{Z}(x_{1i})\right) \\
\hat{R} &= 1 - \sum_\alpha \frac{\omega_{p\alpha}^2}{\omega^2}\left(-x_{o\alpha}\tilde{Z}(x_{-1\alpha})\right) \simeq 1 + \sum_i \frac{\omega_{pi}^2}{\Omega_{ci}(\omega+\Omega_{ci})} \\
\hat{P} &= 1 - \sum_\alpha \frac{\omega_{p\alpha}^2}{\omega^2}\left(x_{o\alpha}^2\tilde{Z}'(x_{o\alpha})\right)
\end{aligned} \tag{5.15}$$

and

$$\begin{aligned}
\hat{S}(\psi,\vartheta;k_\zeta^{m'}) &= \frac{1}{2}\left\{\hat{L}(\psi,\vartheta;k_\zeta^{m'}) + \hat{R}(\psi,\vartheta)\right\} \\
\hat{D}(\psi,\vartheta;k_\zeta^{m'}) &= \frac{1}{2}\left\{\hat{L}(\psi,\vartheta;k_\zeta^{m'}) - \hat{R}(\psi,\vartheta)\right\}
\end{aligned} \tag{5.16}$$

Here

$$x_{n,\alpha} = x_{n,\alpha}(m,\psi,\vartheta) = \frac{\omega - n\Omega_{c\alpha}}{k_\zeta^m v_{th\alpha}} \tag{5.17}$$

and $\tilde{Z}$ is the toroidal Plasma dispersion function

$$-x_{o\alpha}\tilde{Z}(x_{n\alpha}) = \int_{-\infty}^{+\infty} du\,\frac{e^{-u^2}}{\sqrt{\pi}}\left\{-i\omega\int_{-\infty}^{t} e^{i\int_{t'}^{t} k_\zeta^m v_{th}\left(x''_{n\alpha}-u''\right)dt''}\,dt'\right\} \tag{5.18}$$

which will be discussed in the next section.

c) – Contribution from the ion FLR current. Defining

$$\begin{aligned}
\lambda^2\left(\psi,\vartheta;k_\zeta^{m'}\right) &= \frac{1}{2}\sum_i \frac{\omega_{pi}^2}{\Omega_{ci}^2}\frac{v_{thi}^2}{c^2}\left(-x_{oi}\tilde{Z}_{2i}\right) + \frac{1}{2}\frac{\omega_{pe}^2}{\Omega_{ce}^2}\frac{v_{the}^2}{c^2}\frac{\omega}{\omega+2\Omega_{ce}} \\
\rho^2\left(\psi,\vartheta\right) &= \frac{1}{2}\sum_i \frac{\omega_{pi}^2}{\Omega_{ci}^2}\frac{v_{thi}^2}{c^2}\frac{\omega}{\omega+2\Omega_{ci}} + \frac{1}{2}\frac{\omega_{pe}^2}{\Omega_{ce}^2}\frac{v_{the}^2}{c^2}\frac{\omega}{\omega-2\Omega_{ce}}
\end{aligned} \tag{5.19}$$

the contributions from $\vec{J}_i^{(2)}$ to the coefficients Γ can be written

$$\begin{aligned}
\Gamma^{(2)}_{\psi\psi}(m,1,m',1) &= \Gamma^{(2)}_{\eta\eta}(m,1,m',1) \\
&= 2\left(\tilde{T}^{(1)}_- + m\tilde{T}^{(2)}_-\right)^* \cdot \rho^{(2)}(\psi,\vartheta;k_\zeta^{m'}) \cdot \left(\tilde{T}^{(1)}_- + m'\tilde{T}^{(2)}_-\right) \\
&+ 2\left(\tilde{T}^{(1)}_+ + m\tilde{T}^{(2)}_+\right)^* \cdot \lambda^{(2)}(\psi,\vartheta;k_\zeta^{m'}) \cdot \left(\tilde{T}^{(1)}_+ + m'\tilde{T}^{(2)}_+\right) \\
\Gamma^{(2)}_{\psi\psi}(m,1,m',2) &= \Gamma^{(2)}_{\eta\eta}(m,1,m',2) = \\
&= 2\left(\tilde{T}^{(3)}_-\right)^* \cdot \rho^{(2)}(\psi,\vartheta;k_\zeta^{m'}) \cdot \left(\tilde{T}^{(1)}_- + m'\tilde{T}^{(2)}_-\right) \\
&+ 2\left(\tilde{T}^{(3)}_+\right)^* \cdot \lambda^{(2)}(\psi,\vartheta;k_\zeta^{m'}) \cdot \left(\tilde{T}^{(1)}_+ + m'\tilde{T}^{(2)}_+\right) \qquad (5.20) \\
\Gamma^{(2)}_{\psi\psi}(m,2,m',1) &= \Gamma^{(2)}_{\eta\eta}(m,2,m',1) = \\
&= 2\left(\tilde{T}^{(1)}_- + m\tilde{T}^{(2)}_-\right)^* \cdot \rho^{(2)}(\psi,\vartheta;k_\zeta^{m'}) \cdot \tilde{T}^{(3)}_- \\
&+ 2\left(\tilde{T}^{(1)}_+ + m\tilde{T}^{(2)}_+\right)^* \cdot \lambda^{(2)}(\psi,\vartheta;k_\zeta^{m'}) \cdot \tilde{T}^{(3)}_+ \\
\Gamma^{(2)}_{\psi\psi}(m,2,m',2) &= \Gamma^{(2)}_{\eta\eta}(m,2,m',2) = 2\left(\tilde{T}^{(3)}_-\right)^* \cdot \rho^{(2)}(\psi,\vartheta;k_\zeta^{m'}) \cdot \tilde{T}^{(3)}_- \\
&+ 2\left(\tilde{T}^{(3)}_+\right)^* \cdot \lambda^{(2)}(\psi,\vartheta;k_\zeta^{m'}) \cdot \tilde{T}^{(3)}_+
\end{aligned}$$

and

$$\begin{aligned}
\Gamma^{(2)}_{\psi\eta}(m,1,m',1) &= -\Gamma^{(2)}_{\eta\psi}(m,1,m',1) \\
&= -2i\left(\tilde{T}^{(1)}_- + m\tilde{T}^{(2)}_-\right)^* \cdot \rho^{(2)}(\psi,\vartheta;k_\zeta^{m'}) \cdot \left(\tilde{T}^{(1)}_- + m'\tilde{T}^{(2)}_-\right) \\
&+ 2i\left(\tilde{T}^{(1)}_+ + m\tilde{T}^{(2)}_+\right)^* \cdot \lambda^{(2)}(\psi,\vartheta;k_\zeta^{m'}) \cdot \left(\tilde{T}^{(1)}_+ + m'\tilde{T}^{(2)}_+\right) \\
\Gamma^{(2)}_{\psi\eta}(m,1,m',2) &= -\Gamma^{(2)}_{\eta\psi}(m,1,m',2) = \\
&= -2i\left(\tilde{T}^{(3)}_-\right)^* \cdot \rho^{(2)}(\psi,\vartheta;k_\zeta^{m'}) \cdot \left(\tilde{T}^{(1)}_- + m'\tilde{T}^{(2)}_-\right) \\
&+ 2i\left(\tilde{T}^{(3)}_+\right)^* \cdot \lambda^{(2)}(\psi,\vartheta;k_\zeta^{m'}) \cdot \left(\tilde{T}^{(1)}_+ + m'\tilde{T}^{(2)}_+\right) \qquad (5.21) \\
\Gamma^{(2)}_{\psi\eta}(m,2,m',1) &= -\Gamma^{(2)}_{\eta\psi}(m,2,m',1) = \\
&= -2i\left(\tilde{T}^{(1)}_- + m\tilde{T}^{(2)}_-\right)^* \cdot \rho^{(2)}(\psi,\vartheta;k_\zeta^{m'}) \cdot \tilde{T}^{(3)}_- \\
&+ 2i\left(\tilde{T}^{(1)}_+ + m\tilde{T}^{(2)}_+\right)^* \cdot \lambda^{(2)}(\psi,\vartheta;k_\zeta^{m'}) \cdot \tilde{T}^{(3)}_+ \\
\Gamma^{(2)}_{\psi\eta}(m,2,m',2) &= \Gamma^{(2)}_{\eta\psi}(m,2,m',2) = -2i\left(\tilde{T}^{(3)}_-\right)^* \cdot \rho^{(2)}(\psi,\vartheta;k_\zeta^{m'}) \cdot \tilde{T}^{(3)}_- \\
&+ 2i\left(\tilde{T}^{(3)}_+\right)^* \cdot \lambda^{(2)}(\psi,\vartheta;k_\zeta^{m'}) \cdot \tilde{T}^{(3)}_+
\end{aligned}$$

d) – Contribution from the electron FLR current. The TTMP part of the electron current gives the contribution

$$\begin{aligned}
\Gamma^{TT}_{\alpha\beta}(m,1;m',1) &= 2\left(m\tilde{R}^{(2)}_{\zeta\,\alpha}+\tilde{R}^{(1)}_{\zeta\,\alpha}\right)^{*}\cdot\lambda^{o}_{e}(\psi,\vartheta;k^{m'}_{\zeta})\cdot\left(m'\tilde{R}^{(2)}_{\zeta\,\beta}+\tilde{R}^{(1)}_{\zeta\,\beta}\right)\\
\Gamma^{TT}_{\alpha\beta}(m,2;m',1) &= 2\left(\tilde{R}^{(3)}_{\zeta\,\alpha}\right)^{*}\cdot\lambda^{o}_{e}(\psi,\vartheta;k^{m'}_{\zeta})\cdot\left(m'\tilde{R}^{(2)}_{\zeta\,\beta}+\tilde{R}^{(1)}_{\zeta\,\beta}\right)\\
\Gamma^{TT}_{\alpha\beta}(m,1;m',2) &= 2\left(m\tilde{R}^{(2)}_{\zeta\,\alpha}+\tilde{R}^{(1)}_{\zeta\,\alpha}\right)^{*}\cdot\lambda^{o}_{e}(\psi,\vartheta;k^{m'}_{\zeta})\cdot\left(\tilde{R}^{(3)}_{\zeta\,\beta}\right)\\
\Gamma^{TT}_{\alpha\beta}(m,2;m',2) &= 2\left(\tilde{R}^{(3)}_{\zeta\,\alpha}\right)^{*}\cdot\lambda^{o}_{e}(\psi,\vartheta;k^{m'}_{\zeta})\cdot\left(\tilde{R}^{(3)}_{\zeta\,\beta}\right)
\end{aligned}\tag{5.22}$$

where the indexes α, β run only over the perpendicular coordinates ψ, η, and

$$\lambda^{o}_{e}=\frac{1}{2}\frac{\omega^{2}_{pe}}{\Omega^{2}_{ce}}\frac{v^{2}_{the}}{c^{2}}\left(-x_{oe}\tilde{Z}_{oe}\right)\tag{5.23}$$

With the same index convention, the off–diagonal electron current gives the contributions

$$\begin{aligned}
\Gamma^{MX}_{\alpha\zeta}(m,1;m',1) &= \left(\tilde{R}^{(1)}_{\zeta\alpha}+m\tilde{R}^{(2)}_{\zeta\alpha}\right)^{*}\cdot\xi^{o}_{e}(\psi,\vartheta;k^{m'}_{\zeta})\cdot k^{m'}_{\zeta}\\
\Gamma^{MX}_{\alpha\zeta}(m,2;m',1) &= \left(\tilde{R}^{(3)}_{\zeta\alpha}\right)^{*}\cdot\xi^{o}_{e}(\psi,\vartheta;k^{m'}_{\zeta})\cdot k^{m'}_{\zeta}\\
\Gamma^{MX}_{\zeta\beta}(m,1;m',1) &= (k^{m}_{\zeta})^{*}\cdot\xi^{o}_{e}(\psi,\vartheta;k^{m'}_{\zeta})\cdot\left(\tilde{R}^{(1)}_{\zeta\beta}+m'\tilde{R}^{(2)}_{\zeta\beta}\right)\\
\Gamma^{MX}_{\zeta\beta}(m,1;m',2) &= (k^{m}_{\zeta})^{*}\cdot\xi^{o}_{e}(\psi,\vartheta;k^{m'}_{\zeta})\cdot\tilde{R}^{(3)}_{\zeta\beta}
\end{aligned}\tag{5.24}$$

with

$$\xi^{o}_{e}=\frac{1}{2}\frac{\omega^{2}_{pe}}{\omega\Omega_{ce}}\frac{v^{2}_{the}}{c^{2}}x^{2}_{oe}\tilde{Z}'_{oe}\tag{5.25}$$

6 – Boundary conditions in the spectral representation.

6.1 – Regularity conditions on the magnetic axis. The Cartesian components of $\vec{E}$ on the magnetic axis must be uniquely defined, i.e. independent from ϑ. From (2.13) for $\psi\to 0$ we get

$$\begin{aligned}
E_X(0) &= \sum_m e^{im\vartheta}\left\{\left(\frac{1}{N_\tau}\frac{\partial Z}{\partial\vartheta}\right)_o E^{(m)}_{\psi}(0)+\left(\frac{1}{N_\tau}\frac{\partial X}{\partial\vartheta}\right)_o E^{(m)}_{\eta}(0)\right\}\\
E_X(0) &= \sum_m e^{im\vartheta}\left\{-\left(\frac{1}{N_\tau}\frac{\partial X}{\partial\vartheta}\right)_o E^{(m)}_{\psi}(0)+\left(\frac{1}{N_\tau}\frac{\partial Z}{\partial\vartheta}\right)_o E^{(m)}_{\eta}(0)\right\}\\
E_\varphi(0) &= \sum_m e^{im\vartheta}\,E^{(m)}_{\varphi}(0)
\end{aligned}\tag{6.1}$$

These equations completely define the harmonic contents of the electric field components at $\psi = 0$. It is convenient to write the resulting conditions in rotating components. Defining

$$\left(\frac{1}{N_\tau}\frac{\partial Z}{\partial \vartheta}\right)_o = \sum_m Z^m\, e^{im\vartheta} \qquad \left(\frac{1}{N_\tau}\frac{\partial Z}{\partial \vartheta}\right)_o = \sum_m X^m\, e^{im\vartheta} \tag{6.2}$$

we obtain

$$\begin{aligned} 0 &= \sum_{m'} \left(Z^{(m-m')} \mp iX^{(m-m')}\right)\left(E_\psi^{(m')}(0) \pm iE_\eta^{(m')}(0)\right) \\ 0 &= E_\zeta^{(m)}(0) \end{aligned} \tag{6.3}$$

for all $m \neq 0$. If magnetic surfaces approach circular shape as $\psi \to 0$, then $X^{-1} = -X^1 = i/2$, $Z^{-1} = Z^1 = 1/2$, and all other coefficients in Eqs. (6.2) vanish. The first two of Eqs. (6.3) then reduce to

$$\begin{gathered} E_\psi^1 + iE_\eta^1 = 0 \qquad\qquad E_\psi^{-1} - iE_\eta^{-1} = 0 \\ E_\psi^m = E_\eta^m \equiv 0 \quad \text{for all other } m \end{gathered} \tag{6.4}$$

The regularity conditions for $\vec{E}$ suffice to guarantee that the differential operators $\vec{\nabla}\cdot\vec{E}$ and $\vec{\nabla}\times\vec{E}$ (hence the wave magnetic field $\vec{B}$) are *finite* on the magnetic axis. Additional conditions on the derivatives should in principle be imposed to ensure that $\vec{B}$ and $\vec{\nabla}\cdot\vec{E}$ are also indepependent from ϑ as $\psi \to 0$. These conditions, however, are automatically nearly satisfied because of the divergence of the appropriate elements of the metrics near the axis, and it is not necessarily to impose them explicitly.

6.3 – Antenna conditions in the spectral representation.

a) Conditions at the antenna conductors. According to Eq. (4.22) the currents in the antenna conductors provide the r.h. side of the discretized equations. In the spectral representation this driving term is

$$\mathcal{Q}_{ant} = \frac{4\pi i}{\omega}\sum_m \int RN_\tau\, e^{-im\vartheta}\, J^s(\vartheta, n_\varphi)\, \left[F_\eta^{m\,*}\cos(\Theta-\alpha) + F_\zeta^{m\,*}\sin(\Theta-\alpha)\right]_{\psi_A} d\vartheta \tag{6.10}$$

the integral extending on the magnetic surface $\psi = \psi_A$ in which the antenna is located. As already mentioned, only the case $\Theta - \alpha = 0$ is implemented.

If the antenna is immersed in a cold low density scrape-off plasma, numerical perturbations are sometimes observed in the form of relatively strong oscillations of the fields over a few radial mesh intervals on both sides of the antenna (akin to a localized spectral pollution). To improve the situation in these cases we have provided the possibility of having two radial mesh points at $\psi = \psi_A$, one on each side of the conductor. With this

option, the jump conditions (3.21) are used as relations between the variables at the two points. This is implemented by adding to the stiffness matrix at the inner point the appropriate surface contribution. Using the jump conditions to express the values of $(\vec{\nabla} \times \vec{E})^{m'}$ on the inner side of the conductor in terms of those at the outer side, this gives

$$\begin{aligned} \mathcal{Q}^{-}_{surf} = & \frac{c^2}{\omega^2} \sum_{m,m'} \int R N_\tau \, e^{i(m'-m)\vartheta} \left[F^{m\,*}_{\eta} (\vec{\nabla} \times \vec{E})^{m'}_{\zeta} - F^{m\,*}_{\zeta} (\vec{\nabla} \times \vec{E})^{m'}_{\eta} \right]_{\psi=\psi^+_A} \\ & + \frac{4\pi i}{\omega} \sum_{m} \int R N_\tau \, e^{-im\vartheta} \, J^s(\vartheta, n_\varphi) \left[F^{m\,*}_{\eta} \cos(\Theta - \alpha) + F^{m\,*}_{\zeta} \sin(\Theta - \alpha) \right]_{\psi_A} d\vartheta \end{aligned} \tag{6.11}$$

which is a "natural" boundary conditions for the FEL discretisation. We must then also impose the continuity conditions for the tangential field components, which translate immediately into the continuity of the corresponding Fourier coefficients:

$$\left[E^m_\eta \right]_{\psi_A} = \left[E^m_\zeta \right]_{\psi_A} = 0 \tag{6.12}$$

These are "essential" boundary conditions. The continuity of the perpendicular magnetic field, $\left[B^m_\psi \right]_{\psi_A} = 0$, is a consequence of the previous two, and needs not to be imposed separately. As an alternative to the inclusion of the radial currents in feeder and shorts, on the other hand, one can explicitly impose the continuity of E_ψ across the antenna (which strictly speaking should be a consequence of Eq. (5.37)). The rationale of taking the feeders into account is to compensate for the apparent charges at the tips of the main conductor due to the discontinuity of $J^s(\vartheta)$ [18]. Requiring explicitly the continuity of E_ψ should have the same effect.

The two alternative ways of imposing the matching conditions at the antenna usually give identical results, as they should. When the direct method has numerical problems, the two-point method, particularly with a forced continuous E_ψ, sometimes (but not always) improves the behaviour of the solution in the layer around the antenna.

b) – Conditions at the Faraday screen. The simplest implementation of a Faraday shield consists in imposing that the component of the electric field parallel to the blades should vanish on the corresponding magnetic surface $\psi = \psi_F$. If the blades are inclined by the angle β to the toroidal direction, the resulting condition are equivalent to

$$-\sin(\Theta - \beta) \, E^m_\eta(\psi_F) + \cos(\Theta - \beta) \, E^m_\zeta(\psi_F) = 0 \tag{6.13}$$

(for simplicity, we have neglected the weak dependence of Θ on ϑ). Again, however, only the case $\Theta - \beta = 0$ has been implemented.

c) – Conditions at the wall. The conditions at the metallic wall translate into

$$E^m_\eta(1) = E^m_\zeta(1) = 0 \tag{6.14}$$

for all m.

7 – Parallel dispersion and power balance.

7.1 – Approximation to the toroidal plasma dispersion functions. The integrals (5.18) which describe parallel dispersion have formally to be evaluated according to the Landau prescrition, $\mathrm{Im}(\omega) \to 0+$. If this limit is taken literaly, however, they contain resonances not only at the harmonics of the cyclotron frequency, but also at the harmonics of the toroidal bounce frequencies of passing and trapped particles [19]–[20]. This is not only analytically and numerically untractable, but in most cases also physically incorrect. As discussed in [21], collisional phase diffusion efficiently destroys the phase memory of the particles, thereby eliminating the bounce frequency dependence of the plasma response. Hamiltonian stochasticity induced by repeated resonant wave–particle interactions can also lead to the same effect [22].

Because of phase diffusion, only the contribution from the last stationary point in the τ integral, i.e. from the last transit through a cyclotron resonance, has to be taken into account in Eq. (5.18). Models for the resulting "toroidal plasma dispersion function" have been discussed in [23]–[27]. The most complete treatment is due to Lamalle [27], who has also indicated how to evaluate the integrals (5.16) for more general distribution functions. The expressions obtained in [27] for $\tilde{Z}$ are also consistent with the quasilinear diffusion coefficients which should be used in the kinetic equation for the steady–state distribution function in toroidal geometry [28]–[29]; their implementation therefore would allow a truly self–consistent treatment of ion cyclotron heating. This is in principle possible also in TORIC; the execution time, however, would increase by orders of magnitude. A different but powerful approach, based on the solution of Vlasov equation in action–angle variables, has been proposed in [30]; its application to TORIC, however, would not be straightforward.

In [31] we have argued that the effects of toroidal trapping can be safely neglected when investigating wave propagation and absorption. In the simplest approximation, retaining only quadratic terms in the expansion of the fase around the stationary point, the velocity integral can then be performed analytically to give [24]–[25]

$$\tilde{Z}(x_n) \simeq \tilde{Z}(x_n, \gamma) = -i \int_0^\infty e^{i x_n \tau - \frac{\tau^2}{4}(1+\gamma\tau)^2} \, d\tau \tag{7.1}$$

with

$$\gamma \simeq \left(\frac{\omega}{2 k_\parallel^2 R v_{th}} \right) \left(-\frac{\partial \log R}{\partial \vartheta} \right) \sin\Theta \tag{7.2}$$

evaluated at the cyclotron resonance. This approximation is equivalent to assume that ions cross the resonance layer with constant velocity. For large argument $|x_n| \gg 1$ the function $\tilde{Z}(x_n, \gamma)$ has the same asymptotic behaviour as the Fried–Conte Plasma Dispersion Function of the uniform plasma [32],

$$Z(x_n) = \frac{1}{\sqrt{\pi}} \int_{-\infty}^{+\infty} \frac{e^{-u^2}}{u - x_n} \, du + i\sqrt{\pi}\, e^{-x_n^2} \tag{7.3}$$

to which it reduces when $\gamma \to 0$; $\tilde{Z}(x_n, \gamma)$ differs appreciably from $Z(x_n)$ only in the resonance layer $|x_n| = O(1)$ where dispersion and damping are important. The most important effect of toroidicity as expressed through the parameter γ is an appreciable broadenening the resonance region. Unfortunately, the imaginary part of $\tilde{Z}(x_n, \gamma)$ is not everywhere negative. As already noticed in [24], this gives rise to difficulties in interpreting the local power balance, since it makes the local power deposition by ion cyclotron damping negative in some regions even in a Maxwellian plasma. By a more accurate treatment of the parallel particle motion, Lamalle [27] has shown that the local power deposition in a Maxwellian plasma is positive defined everywhere, as one would expect.

An accurate approximation to the τ–integral which takes into account toroidal broadening of the cyclotron resonances while avoiding the unphysical oscillating behaviour of Eq. (7.1) in the asymptotic region, has been proposed in [31]. Following this reference, in TORIC $\tilde{Z}$ is approximated in terms of the ordinary Plasma dispersion function Z with the argument evaluated using an appropriate effective parallel wavenumber

$$-x_o\, \tilde{Z}(x_n) \simeq -\bar{x}_o\, Z(\bar{x}_n) \qquad\qquad \bar{x}_n = \frac{\omega - n\Omega_c}{(k_\parallel)_{eff} v_{th}} \tag{7.4}$$

with $(k_\parallel)_{eff}$ given by

$$(k_\parallel)_{eff} \simeq k_\parallel \frac{\sqrt{1+4\gamma}-1}{2\gamma} \tag{7.5}$$

This equation can be understood by noting that $L_{res} \simeq (2Rv_{th}/n\Omega \sin\Theta)^{1/2}$ is the resonance length for a single ion. This length adds nonlinearly to the thermal Doppler broadening $(k_\parallel v_{th}/\omega)\, R$ of the cyclotron resonance layer. In particular $(k_\parallel)_{eff}$ remains finite even in the limit $k_\parallel \to 0$:

$$(k_\parallel)_{eff} \to \left(\frac{\omega}{2Rv_{th}} \sin\Theta\right)^{1/2} \qquad \text{for } k_\parallel \to 0 \tag{7.6}$$

This also allows to take advantage of the efficient algorithms available to evaluate the function Z [33].

7.2 – The local power balance in the spectral representation. Identifying in Eq. (5.2) $\vec{F}$ with $\vec{E}$ and taking the imaginary part, we obtain the global power balance in the form

$$\begin{aligned} &-\mathrm{Re}\sum_m \left\{ \int\int RJ\, e^{-im\vartheta} \left(\vec{E}^{(m)*}(\psi) \cdot \vec{J}_A(n_\varphi, \psi, \vartheta) \right) d\vartheta\, d\psi \right\} \\ &= \frac{\omega}{4\pi} \mathrm{Im} \sum_m \sum_{m'} \left\{ \int\int RJ\, e^{i(m'-m)\vartheta} \left(\vec{E}^{(m)*}(\psi) \cdot \underline{\underline{Q}}^{\mathrm{op}} \cdot \vec{E}^{(m')}(\psi) \right) d\vartheta\, d\psi \right\} \end{aligned} \tag{7.6}$$

This is an exact consequence of Vlasov–Maxwell equations. The l.h. side is the power launched by the antenna. The integrand of the r.h. side differs from the local rate of dissipation at most by the divergence of a vector which represents a reversible kinetic transport of energy by the hot plasma; this difference however averages to zero on each magnetic surface. On the other hand, the concept of irreversible h.f. power dissipation is meaningful only for times much longer than the transit time of thermal particles in the tokamak. Hence it will suffice to consider the local dissipation rate averaged on each magnetic surface, which can be read directly from (7.6):

$$P_{abs}(\psi) = \frac{\omega}{4\pi} \operatorname{Im} \sum_m \sum_{m'} \left\{ \int RJ\, e^{i(m'-m)\vartheta} \left(\vec{E}^{(m)*}(\psi) \cdot \underline{\underline{\mathcal{Q}}}^{\mathrm{op}} \cdot \vec{E}^{(m)}(\psi) \right) d\vartheta \right\} \tag{7.7}$$

The ϑ integration annichilates the contribution of the kinetic power flux. We now enumerate the various contributions to $P_{abs}(\psi)$.

a) Fundamental ion cyclotron absorption: We derive the explicit form of P_{abs} for the case of fundamental ion cyclotron absorption; the other cases are similar. From the definition, we have

$$P_i^1(\psi) = \frac{\omega}{4\pi} \operatorname{Im} \sum_m \sum_{m'} \int RJ\, e^{i(m'-m)\vartheta} \left(E_+^{(m)*}(\psi)\, L(\psi, \vartheta, k_\zeta^{m'})\, E_+^{(m')}(\psi) \right) d\vartheta \tag{7.8}$$

Writing the imaginary part explicitly and exchanging m and m' in the second term we can rewrite this in two equivalent ways:

$$\begin{aligned} P_i^1(\psi) = \frac{\omega}{8\pi} \sum_m \sum_{m'} \int RJ\, e^{i(m'-m)\vartheta} \\ \left\{ E_+^{(m)*}(\psi) \left\{ \operatorname{Im} \left[L(\psi, \vartheta, k_\zeta^{m'}) \right] + \operatorname{Im} \left[L(\psi, \vartheta, k_\zeta^{m}) \right] \right\} E_+^{(m')}(\psi) \right\} \qquad (7.9) \\ = \frac{\omega}{4\pi} \operatorname{Re} \sum_m \sum_{m'} \int RJ\, e^{i(m'-m)\vartheta} \left\{ E_+^{(m)*}(\psi) \operatorname{Im} \left[L(\psi, \vartheta, k_\zeta^{m'}) \right] E_+^{(m')}(\psi) \right\} d\vartheta \end{aligned}$$

The power balance has been implemented in the last, asymmetric form.

b) Electron Landau damping:

$$P_e^0(\psi) = \frac{\omega}{4\pi} \operatorname{Re} \sum_m \sum_{m'} \int RJ\, e^{i(m'-m)\vartheta} \left\{ E_\zeta^{(m)*}(\psi) \operatorname{Im} \left[P(\psi, \vartheta, k_\zeta^{m'}) \right] E_\zeta^{(m')}(\psi) \right\} d\vartheta \tag{7.10}$$

c) Ion second harmonic absorption:

$$P_i^{(2)}(\psi) = -\frac{\omega}{8\pi}\,\mathrm{Re}\sum_m\sum_{m'}\frac{c^2}{\omega^2}\int RJ\,e^{i(m'-m)\vartheta}$$
$$\left[\tilde{T}_-^{(3)}\left(\frac{dE_\psi^m}{d\psi}+i\frac{dE_\eta^m}{d\psi}\right)+\left(\tilde{T}_-^{(1)}+m\tilde{T}_-^{(2)}\right)\left(E_\psi^m+iE_\eta^m\right)\right]^*\cdot\mathrm{Im}\left(\hat{\lambda}_i^{(2)}(\psi,\vartheta;k_\zeta^{m'})\right)$$
$$\cdot\left[\tilde{T}_-^{(3)}\left(\frac{dE_\psi^{m'}}{d\psi}+i\frac{dE_\eta^{m'}}{d\psi}\right)+\left(\tilde{T}_-^{(1)}+m\tilde{T}_-^{(2)}\right)\left(E_\psi^{m'}+iE_\eta^{m'}\right)\right] \tag{7.11}$$

d) Electron Transit Time damping:

$$P_e^{TT}(\psi) = -\frac{\omega}{4\pi}\,\mathrm{Re}\sum_m\sum_{m'}\sum_\alpha\sum_\beta\frac{c^2}{\omega^2}\int RJ\,e^{i(m'-m)\vartheta}$$
$$\left\{\left[\tilde{R}_{3\alpha}^{(3)}\frac{dE_\alpha^m}{d\psi}+\left(m\tilde{R}_{3\alpha}^{(2)}+\tilde{R}_{3\alpha}^{(1)}\right)E_\alpha^m\right]^*\cdot\mathrm{Im}\left(2\,\hat{\lambda}^0(\psi,\vartheta;k_\zeta^{m'})\right)\right. \tag{7.12}$$
$$\left.\cdot\left[\tilde{R}_{3\beta}^{(3)}\frac{dE_\beta^{m'}}{d\psi}+\left(m'\tilde{R}_{3\beta}^{(2)}+\tilde{R}_{3\beta}^{(1)}\right)E_\beta^{m'}\right]\right\}d\vartheta$$

e) Mixed electron term:

$$P_e^{mxd}(\psi) = \frac{\omega}{8\pi}\,\mathrm{Re}\sum_m\sum_{m'}\sum_{\beta=\psi,\eta}(-1)^\beta\frac{c^2}{\omega^2}\int RJ\,e^{i(m'-m)\vartheta}$$
$$\left\{\left[\tilde{R}_{3\beta}^{(3)}\frac{dE_\beta^m}{d\psi}+\left(\tilde{R}_{3\beta}^{(1)}+m\tilde{R}_{3\beta}^{(2)}\right)E_\beta^m\right]^*\cdot\mathrm{Im}\left[\hat{\xi}_e^0(\psi,\vartheta;k_\zeta^{m'})\right]\cdot\left(k_\zeta^{m'}E_\zeta^{m'}\right)\right. \tag{7.13}$$
$$\left.+\left(k_\zeta^m E_\zeta^m\right)^*\cdot\mathrm{Im}\left[\hat{\xi}_e^0(\psi,\vartheta;k_\zeta^{m'})\right]\cdot\left[\tilde{R}_{3\beta}^{(3)}\frac{dE_\beta^{m'}}{d\psi}+\left(\tilde{R}_{3\beta}^{(1)}+m'\tilde{R}_{3\beta}^{(2)}\right)E_\beta^{m'}\right]\right\}d\vartheta$$

7.3 – The global power balance. By integrating Eqs. (7.7) to (7.12) over the plasma volume, the total power absorbed P_{abs} and its repartition among different species (ion and electrons) is obtained. A consistency check is offered by the fact that the total absorbed power summed over species must be equal to the power radiated by the antenna

$$P_{ant} = \mathrm{Re}\sum_m E_\eta^{(m)*}(\psi_A)\cdot\hat{J}_s^{(m)} \tag{7.14}$$

with

$$\hat{J}_s^{(m)} = \int RN_\tau\,e^{-im\vartheta}J_s(\vartheta)\,d\vartheta \tag{7.15}$$

In addition, assuming that there is no absorption between the antenna and the wall, P_{abs} must be equal to the electromagnetic power flux across the magnetic surface $\psi = \psi_A$ toward the plasma center,

$$P_{em} = \frac{c}{8\pi} \int RN_\tau \, \mathrm{Im} \left\{ E_\eta^* \left(\frac{c}{\omega} \vec{\nabla} \times \vec{E} \right)_\zeta - E_\zeta^* \left(\frac{c}{\omega} \vec{\nabla} \times \vec{E} \right)_\eta \right\} d\vartheta \tag{7.16}$$

which in the spectral representation becomes

$$\begin{aligned} P_{em} = \frac{c}{8\pi} \sum_m \sum_{m'} \int RN_\tau \, e^{i(m-m')\vartheta} \\ \sum_\beta \left\{ E_\eta^{(m)*} \left[\tilde{R}_{\zeta\beta}^{(3)} \frac{dE_\beta^{m'}}{d\psi} + \left(m' \tilde{R}_{\zeta\beta}^{(2)} + \tilde{R}_{\zeta\beta}^{(1)} \right) E_\beta^{m'} \right] \right. \\ \left. - \left\{ E_\zeta^{(m)*} \left[\tilde{R}_{\eta\beta}^{(3)} \frac{dE_\beta^{m'}}{d\psi} + \left(m' \tilde{R}_{\eta\beta}^{(2)} + \tilde{R}_{\eta\beta}^{(1)} \right) E_\beta^{m'} \right] \right\} d\vartheta \end{aligned} \tag{7.17}$$

The comparison of P_{abs} with both P_{ant} and P_{em} gives an idea of the numerical accuracy of the solution.

7.4 – Ad-hoc damping of ion Bernstein waves. The wavelength of ion Bernstein waves becomes rapidly shorter as they propagate away from the mode conversion layer. When $k_\perp v_{thi}/\Omega_{ci} \gtrsim 1$, the SCK approximation breaks down, and its use often gives unphysical results. At the same time, the numerical resolution of such short wavelengthss is problematic. Ion Bernstein waves must therefore be damped before their wavelength becomes too short. This is done by adding to λ_i^2 (Eq. (5.20)) a correction which simulates absorption by perpendicular ion Landau damping:

$$\delta\lambda_i^2 = \begin{cases} iK_1 \left(1 - \frac{\mu_{crit}^2}{\mu_i^2} \right)^4 \beta_{eff} \, f(x_\perp) \, e^{-K_2 x_\perp^2} & \text{if } k_\perp^2)_{BW} > 0 \text{ and } \mu_i^2 > \mu_{crit}^2 \\ 0 & \text{otherwise} \end{cases} \tag{7.18}$$

where

$$\begin{aligned} \mu_i^2 &= \left(\frac{k_\perp^2 v_{thi}^2}{2\Omega_{ci}^2} \right)_{BW} & x_\perp &= \left(\frac{\omega}{k_\perp v_{thi}} \right)_{BW} \\ \beta_{eff} &= \beta_i(\psi) \left(1 - f + f \frac{\beta_i^2(0)}{\beta_i^2(\psi)} \right) & f(x_\perp) &= x_\perp^3 + 1 \end{aligned} \tag{7.19}$$

while K_1, K_2, f and μ_{crit}^2 are parameters which can be adjusted by the user. The $x_\perp^3$ factor before the exponential is characteristic of perpendicular Landau damping by weakly magnetized ions; the second term in $f(x_\perp)$, as well as the correction to the local β in β_{eff} have been added to avoid $\delta\lambda_i^2$ to become negligible when $\beta_i \to 0$, $k_\perp \to \infty$. The μ_{crit}^2–dependent factor provides a smooth transition between the undamped and

the damped region. By an appropriate choice of the free parameters (of order unity except $f \ll 1$) it is not difficult to make shure that all damping occurs far from the mode conversion region, and does not interfere with mode conversion itself and with the reflection of the fast wave from the ion-ion cutoff.

At high harmonics, $\omega \gg \Omega_{ci}$, perpendicular ion Landau damping arises due to the onset of Hamiltonian stochasticity in the ion motion in an electrostatic wave propagating nearly perpendicularly to $\vec{B}_o$ [34] [35]; stochasticity around the fundamental and first harmonic is even more easily observed, but attributing the form (7.18) to the resulting damping is arbitrary, although convenient.

7.5 – Regularization of Alfvén and ion–ion resonances. The perpendicular index of the Fast Wave is nearly singular whenever

$$n_\parallel^2 - S \simeq 0 \tag{7.20}$$

Ion–ion resonances in a multispecies plasma in the mode conversion regime (low $n_\parallel$ and weak ion cyclotron damping) satisfy this condition, and can be very sharp. To "regularize"these quasi-singularities, an ad-hoc "collisional" damping can be added to $\hat{S}$ by writing

$$\hat{S} \rightarrow \hat{S} + i\, K_{awr}\, |\mathrm{Re}(R)|\, \exp\left\{ -Q_{awr}^2 \frac{(n_\parallel^2 - \mathrm{Re}(S))^2}{[\mathrm{Re}(R)]^2} \right\} \tag{7.21}$$

The parameters K_{awr} and Q_{awr} can be adjusted by the user; values $K_{awr} \simeq 0.1$ and $Q_{awr} \simeq 10$ usually ensure that this damping is closely localized near the singularity, yet sufficient to obtain a sufficiently well behaved solution. This procedure, however, is mostly unable to cure the convergence problems due to Alfvén resonances ($\omega < \Omega_{ci}$) or Lower Hybrid resonances ($\omega > \Omega_{ci}$) occurring at low density in the plasma periphery.

In the code a separate bookkeeping is made of the amount of damping due to the modification (7.21) to $\hat{S}$. Physically, if power is absorbed by collisional broadening of wave resonances it should be attributed to the electrons.

8 – The Order Reduction Algorithm.

The Order Reduction Algorithm (ORA) was introduced in [12] to cure the shortcomings of the zero Larmor radius approximation without renouncing to its simplicity. For this purpose, the ion FLR current is omitted, but the zero Larmor radius ion current is 'corrected' by adding to the zero Larmor radius elements of the dielectric tensor the approppriate FLR corrections in algebraic form. This is equivalent to replace the differential operator describing $\vec{J}_i^{(2)}$ by its algebraic limit obtained with a local WKB approximation.

In TORIC, this is implemented by replacing $\hat{R}$ and $\hat{L}$ (Eqs. (3.3)) with the effective quantities

$$\hat{R}_{eff} = \hat{R} - n_\perp^2)_{FW}\hat{\rho}^{(2)} \qquad \hat{L}_{eff} = \hat{L} - n_\perp^2)_{FW}\hat{\lambda}^{(2)} \tag{8.1}$$

where $\hat{\rho}^{(2)}$ and $\hat{\lambda}^{(2)}$ are given by Eq. (3.9), and $n_\perp^2)_{FW}$ is the index of the compressional wave, obtained by solving the local dispersion relation in the limit of negligible electron inertia

$$\sigma^{(2)} n_\perp^4 + \left[(n_\parallel^2 - \hat{S}) + (n_\parallel^2 - \hat{R})\hat{\lambda}^{(2)} + (n_\parallel^2 - \hat{L})\hat{\rho}^{(2)}\right] n_\perp^2 + (n_\parallel^2 - \hat{L})(n_\parallel^2 - \hat{R}) = 0 \tag{8.2}$$

Care must be taken to chose the fast wave root throughout: in the evanescence regions between a cutoff and a confluence with the Ion Bernstein wave, it is the root with positive imaginary part. The FLR corrections to $\hat{R}$ and $\hat{L}$ provide the correct amount of damping of the fast wave near first harmonic cyclotron resonances, and eliminate the singularity of the cold limit at ion-ion resonances.

9 – Radial discretization and numerical implementation.

9.1 – Evaluation of the coefficients on a magnetic surface. A finite system of coupled ordinary differential equations in ψ is obtained from the variational integral (5.2) by choosing the test functions in the form

$$\vec{F} = \frac{F_\alpha^m(\psi)}{2\pi}\, e^{im\vartheta}\, \vec{u}_\alpha\, \delta_{\alpha\,\alpha_o}\, \delta_{m\,m_o} \tag{9.1}$$

where $\vec{u}_\alpha$, $\alpha_o = 1,\ 2,\ 3$ are the unit vectors of the local Stix frame, and the poloidal modes are restricted to $-M_{max} < m_o < M_{max}$. Each of these equations has the form of a convolution sum between the Fourier transform of the fields and those of the coefficients on each magnetic surface. The latter are evaluated using the Fast Fourier Transform (FFT) algorithm. Note that several of the coefficients arising from the h.f. plasma current, namely all those which are influenced by parallel dispersion, depend in addition explicitly on m through k_ζ^m; in this case the FFT must be performed separately for each value of m. For optimal efficiency of the FFT the number M_c of poloidal Fourier component used in the representation of the coefficients is always a power of 2.

The number M_s of poloidal modes kept in the representation of the solution, on the other hand, is always odd, $M_s = 2\,M_{max} + 1$. To avoid having to check the summation boundaries in the convolutions between coefficients and unknowns, and to make optimal use of the information about the ϑ dependence of the coefficients, the condition $M_c > 2\,M_{max}$ is imposed. To reconstruct the fields after solution of the radial equations the inverse Fourier transform must be taken. To be able to use the same FFT routine as for the evaluation of the coefficients, the arrays of field components on each magnetic surface are extended to M_c elements by adding zeros in the outer positions.

The construction of the FFT of order M_c requires information from M_c equally spaced points in ϑ. From this obvious statement it becomes clear that M_c must be sufficient to allow a good resolution of the poloidal variation of the resonant Z–functions on each magnetic surface, while M_s must be sufficient to resolve numerically the shortest wavelength waves occurring in the solution. To a large extent these two criteria are independent from each other, a fact well confirmed by convergence tests. It is nevertheless clear that the most reasonable choice of M_c and M_s should be such that M_s is the smallest power of 2 greater than $2\,M_s$.

9.2 – The radial discretization. To implement the Finite Element (FEM) discretisation, the interval $0 \leq \psi \leq 1$ is subdivided into N_p intervals *(elements)*, and the solution is assumed to have the form

$$E_\alpha^m(\psi) = \sum_r \sum_{\nu=1}^{2} E_{\alpha,\nu}^m(r)\, \hat{H}_{r,\nu}(\xi_r) \tag{9.2}$$

where ξ_r $(-1 \leq \xi_i \leq 1)$ is the normalised coordinate on element r, and the support functions $\hat{H}_{r,\nu}(\xi_r)$ are

$$\begin{aligned} \hat{H}_{r,0}(\xi_r) &= H_0(\xi) \qquad\qquad (-1 \leq \xi \leq 1) \\ \hat{H}_{r,1}(\xi_r) &= \begin{cases} (\psi_{r+1} - \psi_r) H_1(\xi) & \text{if } 0 \leq \xi \leq 1 \\ (\psi_r - \psi_{r-1}) H_1(\xi) & \text{if } (-1 \leq \xi \leq 0) \end{cases} \end{aligned} \tag{9.3}$$

in terms of the Hermite cubic interpolating polynomials H_o and H_1, defined on the master interval $-1 \leq \xi \leq +1$ as:

$$\begin{aligned} H_0(\xi) &= (|\xi| - 1)^2 (2|\xi| + 1) \\ H_1(\xi) &= (|\xi| - 1)^2 \xi \end{aligned} \tag{9.4}$$

With these normalisations, $E_\alpha^0(r)$ and $E_\alpha^1(r)$ are the values of E_α and of its first derivative, respectively, at the mesh point $\psi = \psi_r$. Cubic Hermite FEM have the distinctive advantage to allow solutions (wave electric field) with continuous derivative (wave magnetic field) everywhere. They have been introduced for wave problems in [11].

When (9.2) is used in the variational integral, on each element $x_r \leq x \leq x_{r+1}$ one has to evaluates integrals of the form

$$\begin{aligned} \underline{\underline{Q}}_r(\hat{H}_\alpha, \hat{H}_\beta) = \int_{x_r}^{x_{r+1}} \Big\{ &\underline{\underline{\Gamma}}(0,0)\, \hat{H}_\alpha\, \hat{H}_\beta + \Delta_r\, \underline{\underline{\Gamma}}(0,1)\, \hat{H}_\alpha\, \frac{d\hat{H}_\beta}{dx} + \\ &+ \Delta_r\, \underline{\underline{\Gamma}}(1,0)\, \frac{d\hat{H}_\alpha}{dx}\, \hat{H}_\beta + \Delta_r^2\, \underline{\underline{\Gamma}}(1,1)\, \frac{d\hat{H}_\alpha}{dx}\, \frac{d\hat{H}_\beta}{dx} \Big\}\, dx \end{aligned} \tag{9.5}$$

where the indexes in $\underline{\underline{\Gamma}}$ which have not been omitted refer to the order of the derivative of the test function to the left and to the right of the operator, and $\Delta_r = x_{r+1} - x_r$. These integrals are evaluated with Gaussian integration; the standard option is with three points per element.

The stiffness matrix $\underline{\underline{M}}$ can then be constructed by making the following attributions:

$$\begin{aligned}
\underline{\underline{Q}}_r\left(\hat{H}_\alpha(\xi), \hat{H}_\beta(\xi)\right) &\Rightarrow \underline{\underline{M}}_{\alpha,\beta}(r,r) \\
\underline{\underline{Q}}_r\left(\hat{H}_\alpha(\xi), \hat{H}_\beta(-1+\xi)\right) &\Rightarrow \underline{\underline{M}}_{\alpha,\beta}(r,r+1) \\
\underline{\underline{Q}}_r\left(\hat{H}_\alpha(-1+\xi), \hat{H}_\beta(\xi)\right) &\Rightarrow \underline{\underline{M}}_{\alpha,\beta}(r+1,r) \\
\underline{\underline{Q}}_r\left(\hat{H}_\alpha(-1+\xi), \hat{H}_\beta(-1+\xi)\right) &\Rightarrow \underline{\underline{M}}_{\alpha,\beta}(r+1,r+1)
\end{aligned} \tag{9.6}$$

(diagonal blocks get two contributions, out of diagonal only one). These attributions are performed automatically by a set of all–purpose "master" routines which have already been used in several wave problems..

9.3 – The solver. The block structure of the discretized system is

$$\underline{\underline{L}}_i \cdot \vec{x}_{i-1} + \underline{\underline{D}}_i \cdot \vec{x}_i + \underline{\underline{R}}_i \cdot \vec{x}_{i+1} = \vec{y}_i \qquad i = 1, \ldots, N_p \tag{9.7}$$

with

$$\underline{\underline{L}}_1 = 0 \qquad \underline{\underline{R}}_{N_p} = 0 \tag{9.8}$$

Each $\vec{x}_i$ is a $(6\,M_s)$–dimensional complex vector made up by the Fourier components of $\vec{E}$ and $d\vec{E}/d\psi$ at $\psi = \psi_i$. Adding the boundary conditions at the antenna increases the number of elements by one, but does not alter this structure; the antenna current contributes to y_i at ψ_A. The other boundary conditions are easily implemented by modifying the appropriate blocks of coefficients.

The Ansatz

$$\vec{x}_{i-1} = \underline{\underline{E}}_{i-1} \cdot \vec{x}_i + \vec{F}_{i-1} \tag{9.9}$$

leads to the upward recursive relation

$$\begin{aligned}
\underline{\underline{E}}_i &= -\left(\underline{\underline{D}}_i + \underline{\underline{L}}_i \cdot \underline{\underline{E}}_{i-1}\right)^{-1} \cdot \underline{\underline{R}}_i \\
\vec{F}_i &= \left(\underline{\underline{D}}_i + \underline{\underline{L}}_i \cdot \underline{\underline{E}}_{i-1}\right)^{-1} \cdot \left(\vec{y}_i - \underline{\underline{L}}_i \cdot \vec{F}_{i-1}\right)
\end{aligned} \tag{9.10}$$

to be initialised by $\underline{\underline{E}}_0 = 0$, $\vec{F}_0 = 0$. The downward recursion (9.9) then begins with $\vec{x}_{N_p} = \vec{F}_{N_p}$. The matrices to be inverted are LU–decomposed and the equations (9.8) are implemented using LINPAK routines.

The solver based on this method has the advantage of simplicity and is relatively efficient, but is very memory–consuming. Since only the matrices $\underline{\underline{E}}_i$ and the vectors $\vec{F}_i$ need to be stored, a factor 3 is gained with respect to methods in which all blocks $\underline{\underline{L}}_i$, $\underline{\underline{D}}_i$, $\underline{\underline{R}}_i$ of the stiffness matrix must be simultaneously present in memory. Nevertheless, for M_s poloidal modes and N_ψ radial points the matrices $\underline{\underline{E}}_i$ taken together have $(6 \times M_s)^2 \times N_\psi$ complex elements. The size of the corresponding array limits the largest mesh which can be handled in a given computer. The solver used in previous version of TORIC [4] employed virtual memory on disk, thereby eliminating this restriction at the expense of a more complicated structure and slightly slower execution. If required, interfacing the new version with the old solver would be straightforward.

10 – Using the TORIC code.

10.1 – 'Modes' of the code. TORIC can be used in three 'modes': *exploratory, run,* and *diagnostic.* We now give a brief survey of each mode.

1) The exploratory mode. This mode is chosen by setting ISOL = 0, and allows to get quick information about the behaviour of the dielectric tensor, the local perpendicular index of the Fast and Bernstein waves, etc., both as functions of X along the equatorial plane, and as function of ϑ on a few selected magnetic surfaces. The plots which can be obtained in this mode are:

– The poloidal plasma cross–section with the shape of magnetic surfaces;

– The electron density and temperature and the safety factor q as functions of ψ;

– Information on the local dispersion relation: the elements R, L, S of the cold dielectric dielectric tensor, the FLR elements ρ and λ, and the two roots $n_\perp^2)_{FW}$ and $n_\perp^2)_{BW}$ of the dispersion relation corresponding to the magnetosonic and the Bernstein branches, respectively, as functions of position in the equatorial plane, for the three values $m = -M_s,\ 0,\ +M_s$ of the poloidal wavenumber.

– Information on local damping: the values of $x_e^o = \omega/k_\parallel v_{the}$ and of $k_\perp^2 v_{thi}^2/2\Omega_{ci}^2$ for the Bernstein wave, the damping of Alfvén resonances (imaginary part added to S) and of ion Bernstein waves (imaginary part added to λ_i^2), as functions of position in the equatorial plane, again for $m = -M_s,\ 0,\ +M_s$;

– The real and imaginary part of L, λ and of $n_\perp^2)_{FW}$ and $n_\perp^2)_{BW}$ as functions of ϑ on five equidistant magnetic surfaces for the case $m = 0$;

– The Fourier transforms of the quantities listed above.

The information gained in the exploratory mode is often useful to prepare for a run in a new unfamiliar situation. A look to $n_\perp^2)_{FW}$ and $n_\perp^2)_{BW}$ and their Fourier transforms, for example, gives immediate qualitative information on wether the mesh used is sufficiently dense for the situation under investigation.

2) The run mode. In the run mode (chosen by setting ISOL = 1) the stiffness matrix is built and inverted, and the solution (i.e. the values of the coefficients of the FEM discretization) is stored on disk. This is by far the most time consuming step; to keep the execution time as low as possible, the output is restricted to a summary of the results, and only the electric field components, the compressional component of the magnetic field along the equatorial plane, and the power deposition profiles are plotted. The options available in the run mode are explained in the nest paragraph.

3) The diagnostic mode. In the diagnostic mode (chosen by setting ISOL = -1) the solution is read again from disk, and is used to get more detailed information on the wave pattern, power balance, and so on. The separation between the inversion of the stiffness matrix and the elaboration of the results has two advantages: it allows to develop and test new diagnostics and visualization facilities without having to run each time a full case; and it makes possible to combine the results of several runs for the same plasma parameters but different values of the toroidal wavenumber n_φ, so that the complete spectrum of a real antenna can be scanned.

In addition to the electric and magnetic field components along the equatorial plane and of the power deposition profiles, in the diagnostic mode one can plot: the divergence of $\vec{E}$ (proportional to the charge separation due to the h.f. waves) along the equatorial plane; the Poynting flux versus radius; and contour plots of the three electric field components in a poloidal cross-section. Contour plots or three-dimensional plots of the power deposition are not foreseen, since the power deposition is essentially a surface quantity. Finally, as a "diagnostic" tool, plots of individual polodal components of $\vec{E}$ as functions of ψ can be obtained; this is sometimes useful to investigate the convergence of the spectral expansion.

10.2 – Available options. We now list the available options, indicating mutual incompatibilities when appropriate. Several of the options were made available to make possible the comparison of the standard model of TORIC with alternative models used in the literature or by other codes.

a) Number of independent variables. Normally, the three components of the wave electric field are evaluated simultaneously. This is obtained by setting NVRB = 3. It is also possible, however, to omit the evaluation of the parallel component by setting NVRB = 2. In this case only Transit Time damping by the electrons is taken into account if IFLRE = 1 (cfr. *c)* below); if IFLRE = 0 no power goes to the electrons (the perturbative evaluation of E_ζ which was used in FISIC has not been implemented in TORIC).

b) Ion model. The model for the ions is set by specifying the integer IFLR. The standard choice is IFLR = 1, which corresponds to the SCK model. With IFLR = 0 the finite Larmor radius terms from the ions are omitted; this choice is recommended for example when investigating electron heating or current drive in the absence of ion

cyclotron resonances. The value IFLR $= -1$ is reserved for the Order Reduction algorithm. It should be noted that the zero Larmor radius approximation and the OR algorithm are sometimes subject to spectral pollution; this problem can often be overcome by specifying RPSIBW appropriately (see below).

The following options specify further how ion terms are treated:

– *Toroidicity effects on ion cyclotron resonances.* The broadening of ion cyclotron resonances due to toroidicity discussed in section 5.1 is taken into account if IQTOR $= 1$ (standard option) and omitted if IQTOR $= 0$. The parameter IQTOR is ignored if IBPOL $= 0$ (cfr. *d)* below);

– *Damping of ion Bernstein waves.* Stochastic damping of ion Bernstein waves is taken into account if ISTOCH $= 1$. The parameters K_1, K_2 and μ^2_{crit} in Eq. (5.18) are called ENHSTC, QLBSTH and QLBEPS, respectively; they should all be of order unity. By adding an appropriate *real* contribution to λ_i^2 it is also possible (but not recommended) to set an artificial lower limit to the wavelength of the IB wave, of the order of QMSHBW times the length of a radial mesh element.

Ion Bernstein waves can be altogether suppressed (made evanescent) by altering λ_i^2 outside a given magnetic surface $r =$ RPSIBW. This is done by imposing

$$\lambda_i^{(2)} = \rho^{(2)} = -\sigma_v^{(2)}\,\mathrm{Re}(S) \tag{10.1}$$

With this substitution the local perpendicular index of the slowest wave is

$$n_\perp^2)_{BW} \simeq 2S/(\lambda_i^{(2)} + \rho^{(2)}) = -\sigma_v^{(2)} \tag{10.2}$$

corresponding to a strongly evanescent wave. The constant $\sigma_v^{(2)}$ can be adjusted by the user (variable SIGVAC); it is defined so that when equal to unity the evanescence length is twice the radial mesh step. This option, which is turned off by chosing RPSIBW negative or larger than the vessel radius, can be useful in situations where Ion Bernstein waves violate the FLR approximation before being successfully damped for reasonable values of ENHSTC, QLBSTH and QLBEPS. A similar approach turns out to be useful also to suppress spectral pollution in vacuum behind the Faraday screen.

– *Damping of ion–ion and Alfvén resonances.* Setting IALFVN $= 1$ forces damping near Alfvén singularities according to Eq. (5.22). The parameters K_{awr} and Q_{awr} are called ENHRES and ANSLIM, respectively. Typically, both should be of the order of 10^2; a run in the exploratory mode can be useful to optimize the choice of these quantities. This option should be used only if other damping mechanisms are too weak to ensure that near–singularities can be properly resolved, in particular in the case of isolated ion–ion resonances and with the OR algorithm.

c) Electron model. The model for the electrons is set by specifying the integers NVRB (which indicates the number of components in $\vec{E}$) and IFLRE. The standard choice is NVRB = 3, IFLRE = 1, which corresponds to the full FLR model for the electrons, including the TTMP, ELD and the mixed term. With NVRB = 3, IFLRE = 0 FLR terms are omitted, i.e. only ELD is taken into account. With NVRB = 2 and IFLRE = −1 the parallel electric field is neglected, and only the TTMP term is taken into account. To obtain quantitatively accurate results in spite of this approximation, the coefficient describing TTMP damping is multiplied by 0.5 [36]. Finally, NVRB = 2, IFLRE = 0 corresponds to the zero electron inertia, zero electron Larmor radius approximation: in this limit the electrons completely screen out the parallel electric field E_ζ, but play no role in the absorption.

d) Poloidal magnetic field. The integer IBPOL specifies wether the poloidal component of the static magnetic field is taken into account (standard choice, IBPOL = 1) or omitted (IBPOL = 0). The reason to offer the option IBPOL = 0 is that the combination IFLR = 0, IBPOL = 1 is not physically meaningful. The option IFLR = 0 suppresses ion Bernstein waves by lowering the order of the local dispersion relation in $n_\perp^2$, but leaves unchanged the order in $n_\parallel^2$. With IBPOL = 1, however, $n_\parallel^2$ is itself a differential operator; as a consequence, at ion–ion resonances mode–conversion excites shear Alfvén waves propagating nearly parallel to the magnetic field lines on the side of the resonance opposite to that on which one would expect the ion Bernstein waves. The shear Alfvén wave root of the dispersion relation, however, is spurious, except in the very low pressure limit $\beta_i \ll m_e/m_i$ [7].

e) Modeling the plasma edge. The outer plasma layers often pose the most difficult numerical problems, since a given mesh in ϑ becomes less and less dense as the radius increases. At the same time, because of the low density and temperature at the plasma periphery, the wavelength of hot plasma waves becomes very short there. To alleviate these problems, we have tried and implemented several alternative treatments of the scrape–off plasma: in difficult cases the model giving the best results can be found by trial and error.

The parameter for the choice of the model for the outer layers is IMDEDG; modeling in this region, however, is influenced also by other parameters, such as RPSIBW. The options are:

– IMDEDG = 2 – The plasma extends up to the walls, with the density and temperature profiles specified by the user. The antenna is immersed in the plasma.

– IMDEDG = 1 – The plasma extends to the wall, but outside the Faraday screen the density is modulated poloidally so that it nearly vanishes around the antenna:

$$n_{eff}(\psi,\vartheta) = n_e(\psi)\left\{1 - 0.5\left[1 - \tanh\left(\frac{\vartheta - \vartheta_o}{2.5\Delta\vartheta}\right)\right]\right\} \qquad (10.3)$$

where $\vartheta_o = L_{ant}/2a$ is the angular aperture of the antenna, and $\Delta\vartheta$ the mesh step in ϑ. Ion Bernstein waves are suppressed in the whole region behind the screen by specifying RPSIBW to coincide with the screen position. This is the most realistic model: the antenna is (nearly) in vacuum, while elsewhere the plasma extends to the wall. This model occasionally predicts an enhanced value of E_ζ between the antenna and the Faraday shield; this might well be a real effect.

– IMDEDG = 0 – The plasma extends to the wall, but outside the Farady screen it is cold and dissipationless.

– IMDEDG = -1 – A vacuum layer extends between the Faraday screen and the wall. This choice has been provided for comparison with other codes which make the same assumption, using a separate analytic treatment for this layer, including the antenna boundary conditions. The solution in the vacuum layer, unfortunately, is prone to spectral pollution for low n_φ modes.

– IMDEDG = -2 – This choice is similar to the previous one, except that spectral pollution in the vacuum layer is suppressed by slightly modifying Maxwell equations, as discussed below.

Maxwell equations in vacuum are invariant for rotations around the local radial direction, or, in other words, their solutions do not depend on the presence of the poloidal component of the static magnetic field, except indirectly through the boundary conditions at the plasma-vacuum interface. We have therefore found it convenient, in cases IMDEDG ¡ 0, to switch off B_ϑ in the vacuum region. This not only speeds up the computation, but appreciably reduces the tendency to spectral pollution.

10.3 – Performances of TORIC. Both the memory requirements and the execution time of TORIC increase linearly with the number of radial elements N_p and quadratically with the number of poloidal modes M_s. Rough estimates are

Memory:	$10^{-4} \cdot (N_p\, M_s^2)$ MW
CPU time (Cray YMP):	$10^{-2} \cdot (N_p\, M_s^2)$ sec

for a run of the most complicated model (IFLR = IFLRE = IBPOL = IQTOR = IMDEDG = 1). All other models execute faster. The OR algorithm, in particular, reduces the CPU time by a factor between 1.5 and 3 (for the same mesh).

These performances limit the size of plasmas which can be confortably handled by TORIC, since the effort required for a full scan of the antenna spectrum increases roughly as the cube of the plasma size. The full version of TORIC is well adapted to plasmas of the size of ASDEX Upgrade or somewhat larger; it is possible to deal routinely with plasmas of the JET or ITER size only with the Order Reduction option.

10.4 – Convergence. Convergence of the radial FEM discretization is generally very good: the only requirement is that the mesh step should everywhere be somewhat smaller than the shortest wavelength in the solution. Problems arising if Ion Bernstein waves are allowed to propagate in the region where $k_\perp v_{thi}/\Omega_{ci} \gtrsim 1$ can usually be overcome by increasing ad–hoc damping of these waves. More difficult can be to ensure the numerical resolution of evanescent shear waves excited near the plasma boundary, particularly if the edge density is low and n_φ small. Collisional damping can help provided no Alfvén resonance occurs close to the plasma edge.

Convergence of the poloidal expansion is easily achieved if absorption is sufficiently strong, which is usually the case if the toroidal wave number is not too close to zero. When a non–negligible fraction of the power is mode–converted to ion Bernstein waves (low toroidal wavenumbers) the number of poloidal modes required increases. As long as the overall field pattern is not disrupted, however, lack of complete convergence of the poloidal expansion does not greatly affect the power balance. Convergence can nevertheless be problematic in situations where absorption is weak, and in the presence of sharp resonances, particularly if located far from the magnetic axis.

A rough indicator of convergence is the comparison of the total power deposited in the plasma with the power radiated by the antenna. The latter, moreover, is evaluated in two independent ways, namely as $\langle \vec{J}_A \cdot \vec{E} \rangle$, and as flux of the Poynting vector through the magnetic surface in which the antenna is located. In well converged cases the three values agree typicaly within a fraction of a percent; the remaining discrepancy is mostly imputable to inaccuarcy in the integration of the power deposition profiles over the plasma volume.

It should be kept in mind, however, that the consistency of the power balance is neither sufficient nor, in some sense, necessary for a convergent solution. As already mentioned, the most difficult numerical problems often arise in the outer plasma layers; in particular, convergence of $\langle \vec{J}_A \cdot \vec{E} \rangle$ at the antenna is considerably more difficult to achieve than convergence of the field pattern inside the plasma. The Galerkin discretization of the problem turns out to be very robust with respect to local inaccuracies; thus power deposition profiles and wave pattern in the plasma are often well converged even if the power balance is wrong by 20% or more. By contrast, obviously spectrally polluted solutions sometimes have a surprisingly good power balance. In doubt, only the comparison of runs with different meshes can prove or disprove the reliability of a solution.

A situation which TORIC is definitely unable to handle, as already mentioned, is the presence of Alfvén or Lower Hybrid resonances at the plasma periphery. Short wavelength solutions associated to these singularities interact strongly with the boundary conditions. Resonance layers of this kind, moreover, are often strongly inhomogeneous also in the poloidal direction, since they do not coincide exactly with a magnetic surface. In such cases, convergence is nearly impossible to achieve with a reasonable mesh.

10.5 – Numerical resolution of Ion Bernstein Waves. The problems posed by the numerical resolution of Ion Bernstein waves (IBW) become obvious when one think that their wavelength becomes comparable to the ion Larmor radius before they are damped away. This in principle seems to require prohibitively large poloidal wavenumbers, particularly at large radii: the minimum number $2M + 1$ of poloidal modes should satisfy

$$M \gtrsim \frac{r\Omega_{ci}}{v_{thi}} \tag{10.4}$$

In fact, the requirements are somewhat less severe, because only modes around $n_{\|} \simeq 0$ are efficiently mode converted. For example, for minority heating of H^+ in D^+ the criterion is

$$|k_{\|}|v_{thi} \lesssim \frac{n_H}{n_e}\Omega_{cH} \tag{10.5}$$

since at larger values of $k_{\|}$ Doppler broadening of the cyclotron resonance washes away the conversion region. As a consequence of this restriction on m_ϑ the wavefronts if IBW tend to align with magnetic surfaces. This is fortunate, because convergence in the radial mesh is much easier to obtain at all radii. For waves with low toroidal wavenumber the requirement is therefore

$$M \gtrsim \frac{n_H}{n_e}\frac{r\Omega_{ci}}{v_{thi}} \tag{10.6}$$

reduced by a factor $\sim n_H/n_e$ compared to (10.4), but very still difficult to satisfy in the outer plasma layers of large devices. It is also clear that waves with large toroidal wavenumber will be subject to much less conversion to IBW, since the spectrum of $k_{\|}$ presented by these waves is centered on values which do not satisfy (10.5). Even in this case, however, full convergence will not be achieved unless poloidal modes around $n_{\|} \simeq 0$ are adequately sampled. Thus in principle one should require

$$M \gtrsim |n_\varphi|\frac{r}{qR} + \frac{n_H}{n_e}\frac{r\Omega_{ci}}{v_{thi}} \tag{10.7}$$

where q is the safety factor. At first sight, this is even more severe than (10.6); as n_φ increases, however, coupling among poloidal modes decreases, because the Fourier transform of the coefficients of the wave equation has a narrower m_ϑ distribution. Thus excitation of poloidal modes with $n_{\|} \simeq 0$ is very weak, and omitting them results in a negligible error.

10.6 – A note on Spectral Pollution. As mentioned above, the solutions obtained with the cubic FEM discretization in the radial variable can be spoiled by spectral pollution, i.e. by numerically generated oscillations on the scale of the mesh step. The origin of this problem is easily understood. The dispersion relation of plane waves satisfying the discretized equations (in the local or WKB approximation) is slighltly different from the dispersion relation of the continuous equations, the differences in wavevelength being of the order of the mesh step Δr. The discretized solution, therefore, is reliable only

for waves with wavelengths sufficiently larger than Δr. Spectral pollution occurs when an evanescent wave with evanescence length of the order Δr is transformed into a propagating wave (with a wavelength of the same order) by the discretization.

In vacuum or in the plasma in the zero Larmor radius approximation (including the Order Reduction case) the wave equations admit only two independent solution. In these cases the third order FEM discretization *always* introduces a third independent wave. This has no consequences as long as this spourious additional wave is evanescent, but becomes the dominant feature if it happens to be propagative. When this occur, however, it can be suppressed by modifying slightly the vave equations so that they possess a third evanescent wave with evanescence length just large enough to be robust to the discretization. This is done in TORIC by adding a term of the form

$$-\vec{\nabla}\left(\sigma_v \vec{\nabla}\cdot\vec{E}\right) \tag{10.8}$$

with $\sigma_v > 0$ as small as possible. This trick can be regarded as a modification of the discretization procedure which eliminates a numerical instability without interfering with the other properties of the solution. The spurious evanescent wave (whether due to the discretization or artificially imposed by modifying the wave equations) is slightly excited at discontinuities, e.g. at the antenna. The FEM discretization, however, is extremely robust to local perturbations which do not radiate, since it always choses *automatically* the solution which dies away exponentially from the excitation point. The local perturbation, therefore, does not interfere with the other boundary conditions, and does not alter in any way the solution elsewhere.

Empirically, the OR algorithm turns out to be almost immune to spectral pollution. In the standard ASDEX Upgrade case discussed below only the $n_\varphi = 0$ and 1 modes showed some sign of pollution (the mode $n_\varphi = 0$ is singular in the OR approximation, since it has no absorption whatsoever, and in principle the solution should be infinite. The fact that it could nevertheless be run obtaining a recognizable field pattern, although irregular and with very large amplitude, indicates a weak numerical dissipation). The full wave equations showed spectral pollution in vacuum for $|n_\varphi| \leq 5$; it could be suppressed successfully by the procedure indicated above.

As mentioned above, spectral pollution in the vacuum layer behind the Faraday screen is often successfully suppressed by switching off the poloidal component of the magnetic field in vacuum. When all three approaches (i.e. straightfordward integration, regularization by a term of the form (10.8) and $B_\theta = 0$) can be used, they give practically identical results provided σ_v is sufficiently small.

11 – Examples.

For space reasons, only a "reference" case for TORIC can be presented here, namely a minority heating scenario in ASDEX Upgrade (5% Hydrogen in a Deuterium plasma). We will also omit any discussion of the results from the point of view of the physics of IC heating. The plasma and antenna parameters are listed in Table 1 (this table is part of the standard output of the code itself). The density, temperature and $q(\psi)$ profiles are shown in fig. 1 (note that safety factor at the separatrix, $\psi = 0.68$, is only $q \simeq 3.5$; the poloidal field in vacuum is irrelevant). Fig. 2 and 3 show the components of the dielectric tensor and the roots of the dispersion relation along the equatorial plane for the toroidal wavenumber $n_\varphi = 20$ and the central poloidal mode $m = 0$; also shown are the ratio of the parallel phase velocity to the electron thermal speed x_e, the imaginary contribution added to λ_i^2 to damp ion Bernstein waves, and the value of $k_\perp^2 v_{thH}^2/\Omega_{cH}$ for the Bernstein wave.

11.1 – Minority regime. We consider first the toroidal wavenumber $n_\varphi = 20$, which is representative of the spectre of the antisymmetric (dipole) antenna at $f = 30$ Mhz. This is a relatively "easy" case well in the minority heating regime, with high single-pass absorption and rather weak excitation of ion Bersntein waves. Figure 4 shows the fields components in the equatorial plane, fig. 5 the Poynting flux and the power deposition profiles, and fig. 6 contour plots of the electric field (real part of E_+, E_- and E_ζ) in the poloidal cross-section at the antenna position. A summary of the power balance is given in Table 2 (run n. 1) .

Particularly interesting from the numerical point of view is the solution in the outer layers. The plasma terminates at the Faraday screen and the antenna is located in vacuum. Although spectral pollution is globally absent, there is some hint of it in the spikes of the electric field at the 'discontinuities' represented by the Faraday shield and the antenna itself; they are particularly conspicuous in the plot of $\vec{\nabla}\cdot\vec{E}$, which in vacuum should be strictly zero. The magnetic field, on the other hand, behaves well everywhere.

The number of poloidal modes used to obtain the solution of figs. 4 to 6 was 31, with a poloidal mesh of 64 points and a radial mesh with 300 elements. From the results of table 2, however, it appears that reasonable convergence can be achieved with fewer poloidal modes. With 19 modes (run n. 3) the CPU time is reduced by almost a factor 3 without appreciably spoiling the results. With as few as 11 modes and 32 points in ϑ (run n. 5) the power balance and the power deposition profiles are still nearly unchanged, and the field pattern is perfectly recognizable, although rough.

A closer exhamination, on the other hand, shows that full convergence has not been reached even with the largest number of modes used. The Poynting flux towards the plasma and $\langle \vec{J}\cdot\vec{E}\rangle$ at the antenna agree to 5 digits, but the total power deposited in the plasma is about 5 % lower, a much larger discrepancy than justified by the inherent inaccuracy due to the discretization. Part of the discrepancy is due to the spikes of $\vec{E}$

near the antenna. A further reason, however, must be identified with the failure to fully resolve Bernstein waves with the poloidal mesh available, as discussed in section 10.5.

Also interesting is to compare the complete model with simulations in which the model has been simplified. The first of such simplifications (run n. 3a) consists in neglecting the toroidal broadening of ion cyclotron resonances (cfr. section 7.1). This reduces somewhat minority absorption, and makes the power deposition profile of Hydrogen narrower (and therefore peaked sligtly off-axis, since the resonance is located about 3 cm to the inside), as shown in fig. 7a. The additional available power goes mostly to the electrons, but for a small part also to ion Bernstein waves, whose amplitude, accordingly, is appreciably larger. Even in a relatively small tokamak, however, this is not a large effect, and its importance decreases with the plasma size.

Next (run n. 3 b) we have run the same case with $B_\vartheta = 0$. If the poloidal component of the static magnetic field is neglected the argument of the toroidal Z functions in the dielectric tensor elements is the same for all poloidal modes; exploiting this, the overhead for the evaluation of the stiffness matrix is appreciably reduced. The results (fig. 7b) are nevertheless almost indistinguishable from those of the previous run, both globally and in details. We can conclude, not unexpectedly, that when the toroidal wavenumber n_φ is sufficiently large the broadening of the $k_\parallel$ spectrum due to the $(m_\vartheta/r)\sin\Theta$ contributions, although numerically important ($10 \lesssim k_\parallel \lesssim 30$ near the magnetic axis if $-15 \leq m_\vartheta \leq +15$, does not strongly affect the power deposition profiles, all modes being anyhow well in the minority regime.

Finally, we have investigated the performances of the Order Reduction Algorithm. With 19 poloidal modes (run n. 6 and fig. 8) the field pattern and the global power balance are remarkably close to those obtained with the exact model. In the power distribution among species, however, one notes that heating of the majority is somewhat increased, since the power which was previously mode-converted to IBW is now assigned to harmonic heating.

In the ORA the ion FLR current is an algebraic instead of a differential operator, but to evaluate it one must solve the local dispersion relation at each point of the mesh. If the mesh is kept constant, therefore, the gain in execution time is relatively modest. The advantage of the ORA is that the number of mesh points can be drastically reduced without spoiling the convergence. This is illustrated by runs 6 to 9a. The latter, in particular, which has been further accelerated by suppressing the evaluation of the parallel electric field, offers a sufficiently accurate power deposition profiles in less than 10 s. In this operation mode TORIC compares favorably in performance with plane geometry and even ray-tracing codes, and could be used in conjunction with transport codes for the quantitative predictions of ICRH in tokamaks.

For comparison, the results from the slab code FELICE and the ray tracing code RAYIC for the same case are also listed in table 2, and in figs. 9 and 10, respectively.

Although the plasma size is such that the validity of the Eikonal approximation is rather marginal, the agreement is good; ray tracing, however, predicts slightly broader power deposition profiles (note that in RAYIC $\psi = 1$ is at the plasma edge; the profiles of FELICE, of course, cannot be compared). It is also interesting to note that the range of $k_{\|}$ predicted by RAYIC near the magnetic axis is quite comparable with the one predicted by TORIC, although the origin of the spread (the different evolution of $k_{\|}$ along different rays) is completely different.

Ray tracing also offers an estimate of the so called "single pass absorption", a somewhat vaguely defined quantity which, however, is a useful indication of the strength of damping. Ray tracing stops either when all the power is absorbed, or at the cutoff associated with an ion-ion resonance; the efficiency of mode conversion there is estimated from a modified slab model constructed keeping constant the vertical component k_Z of the wavevector [37]. In RAYIC, therefore, the single pass absorption takes into account damping of the incoming wave (but not of the wave reflected from the cutoff) at the cyclotron resonance, and absorption by the electrons between the antenna and the ion-ion cutoff; the mode converted power, moreover, is attributed entirely to the electrons. For the present case the single pass absorption defined in this way exceeds 90%.

11.2 – Mode conversion regime. As an example of the difficulty of reaching convergence for low toroidal wavenumbers we consider now the case $n_\varphi = 4$, well in the mode conversion regime. According to RAYIC the single pass absorption in this case is only about 15%, and Felice predicts a rather large amount of power going into the excitation of ion Bernstein waves. Although toroidicity has been predicted to decrease substantially the efficiency of mode conversion [30], this is obviously a difficult scenario for a full wave toroidal code.

If the wave equations are straightforwardly integrated through the vacuum layer behind the Faraday screen, the solution in this layer is found to be heavily polluted. Fortunately, pollution disappears if either we regularize the equations according to the scheme of section 10.6 (with $\sigma_v = 4\,10^{-6}$), or we switch off the irrelevant B_{pol} in vacuum. The two procedures give identical results to an accuracy of $\sim 10^{-4}$ or better. It is remarkable, moreover, that in the run with polluted edge the compressional magnetic field pattern and the power distribution profiles in the plasma are not only well behaved, but almost identical with those of the unpolluted case (fig. 11, to be compared with fig. 12 below). This illustrates the robustness of the FEM discretization to local perturbations of the solution. When pollution is eliminated, one finds a rather strong surface wave between the antenna and the Faraday shield. This mode has $m_\vartheta = -8$, which makes $n_{\|}^2 \simeq 1$ in vacuum. This kind of 'guided' wave in vacuum is often found also by FELICE [38], although not in this particular case. In toroidal geometry, however, it is strongly localized to the low field side, and, in contrast to the predictions of the slab approximation, does not contribute appreciably to the radiation resistance of the antenna, since it cannot radiate to infinity.

Once the pollution problem is overcome, a run with 19 poloidal modes (64 points in the poloidal mesh) appears to reach an acceptable convergence, although the power in the plasma is about 15% too large (figs. 12-13). A closer look to the field pattern, however, reveals that convergence is poor just inside the separatrix. Thus in the plot of E_ζ along the equatorial plane short wavelength oscillations can be seen on the low-field side near the plasma edge, where Bernstein waves should be evanescent. These oscillations "spill over" from the high field side, where Bernstein waves are excited, due to insufficient destructive interference among poloidal modes.

Increasing the number of poloidal components, however, further spoils the consistency of the power balance, instead of improving it. As can be seen in Table 3, with 31 modes the discrepancy between P_{abs} and $\langle \vec{J} \cdot \vec{E} \rangle$ at the antenna is a factor 2. The reason is that the parallel wavevector of components with $m_\vartheta \simeq -15$ happens to be around zero just in the region where Ion Bernstein waves propagate (modes with large positive m_ϑ, on the other hand, have a sufficiently large $k_\parallel$ to be in the minority regime in which mode conversion is suppressed). Thus with 19 modes the domain of Fourier space in which mode conversion is most efficient is only marginally explored, while with 31 modes the scan is stopped just in the middle of it. Since in the sums giving P_{abs} there are large internal compensations, it is not astonishing that the error in the power balance is larger in the second case. We must conclude that as far as Bernstein waves are concerned the convergence of the run with 19 poloidal modes is illusory; to reach true convergence one should use say 63 modes and 128 points in the poloidal mesh. Such a run, unfortunately, would require about two hours of CPU time and 100 Mwords of memory, and we have not attempted it. We stress, however, that while the mode converted power is likely to be somewhat underestimated, the other dissipation channels and their radial profiles are already essentially correct in the runs made.

We will also mention that if we assume a warm low density plasma to extend to the wall, we find little change in the field pattern and in the ion and electron heating profiles, but the antenna loading and the mode conversion efficiency are increased by a factor of about 3. These runs, however, are so poorly converged that we cannot consider these results as quantitatively accurate.

If we neglect the poloidal magnetic field in the plasma we find an increase in majority harmonic damping, and less electron heating. This is due to the suppression of $k_\parallel$-broadening: when B_ϑ is taken into account, a non-negligible part of the positive m_ϑ components have a sufficiently large $k_\parallel$ to be in the minority regime; this decreases harmonic damping and increases damping by the electrons. Thus, in contrast to the previous case, the poloidal magnetic field has a nonnegligible influence on low n_φ modes. The results of the order reduction algorithm are again close to those of the standard case, although electron heating is also somewhat reduced, probably because electron damping of Bernstein waves is no more available.

In the mode conversion regime the results of FELICE and RAYIC agree less well with those of the toroidol wave code. In FELICE the dominant toroidal effect, namely the large dispersion of $k_{\|}$ due to the poloidal magnetic field, is completely omitted; for the single value of $k_{\|}$ retained, moreover, a much larger mode conversion efficiency is predicted. The power profiles of ray tracing, on the other hand, account for only 15% of the total power, so that a detailed comparison is difficult; it is clear, however, that they are again too broad, a fact which is probably to be attributed to the marginal validity of the Eikonal approximation for a plasma of this size.

12 – Conclusions.

TORIC gives very satisfactory results in ICRH scenarios with good absorption. The flexibility of the code and the numerous options available offer the possibility of investigating the effects of toroidicity on the propagation and absorption of cyclotron waves in details. The Order Reduction Algorithm, on the other hand, makes it possible to obtain sufficiently accurate power deposition profiles with a very reduced numerical effort. Since power deposition profiles taking into account correctly the toroidal geometry are very difficult to produce with any other approach, this constitute a decisive progress in view of the simulation of ICR heated discharges.

Reaching a full numerical convergence in situations with low absorption and large excitation of short wavelength modes (ion Bernstein waves) is more difficult, and might require very long runs with prohibitively dense meshes. Even if complete convergence is not achieved, however, TORIC often gives acceptable solutions also in such scenarios, which can be very useful to understand the physics of ICR heating and to predict the radial power deposition profiles. Spectral pollution, in particular, can almost always be avoided.

Future development which are particularly desirable are a better treatment of the vacuum region around the antenna, and the inclusion of the effects of quasilinear deformations of the ion distribution functions on the coefficients of the wave equations.

References.

[1] – Fukuyama A., Itoh K., Itoh S.-I., Comp. Phys. Rep. **40** (1986) 137.

[2] – Villard L, Appert K, Gruber R., Vaklavik J., Comp. Phys. Rep. **40** (1986) 95.

[3] – Edery D., Picq H., Comp. Phys. Comm. 4 (1986) 95.

[4] – Brambilla M., Krücken T., Nucl. Fus. **28** (1988) 1813.

[5] – Jaeger E.F., Batchelor D.B., Carter M.D., Weitzner H., Nucl. Fus. **30**(1990) 505.

[6] – Cattanei G., Murphy A.B., Nucl. Fus. **31** (1991) 219.

[7] – Brambilla M., Plasma Phys. Contr. Fus. **35** (1993) A141.

[8] – Swanson D.G., Phys. Fluids **24** (1981) 2035.

[9] – Colestock P.T., Kashuba, R.J., Nucl. Fus. **23** (1983) 763.

[10] – Brambilla M., Plasma Phys. Contr. Fus. **31** (1989) 723.

[11] – Appert K., Hellsten T., Vaclavik J., Villard L., Comp. Phys. Comm. 4 (1986) 73.

[12] – Smithe D.N., Colestock P.L., Kashuba R.J., Kammash T. Nucl. Fus. **27** (1987) 1319.

[13] – Brambilla M., Nucl. Fus. **34** (1994) 1121.

[14] – Van Eester D., J. Plasma Phys. **54** (1995) 31.

[15] – Brunner S., Vaclavik J. Phys. Fluids **B 5** (1993) 1695.

[16] – Brambilla M., Krücken T., Plasma Phys. Contr. Fus. **30** (1988) 1083.

[17] – Brambilla M., Nucl. Fus. **35** (1995) 1265.

[18] – V.P. Bhatnagar, R. Koch, A.M. Messiaen, R.R. Weynants, Nucl. Fus. **22** (1982) 279.

[19] – Kaladze T.D., Mikhailowskii A.B., Sov. J. Plasma Phys **1** (1975) 128.

[20] – Cattanei G., Croci R., Nucl. Fus. **17** (1977) 239.

[21] – Kasilov S.V., Pyatak A.I., Stepanov K.M., Nucl. Fus. **30** (1990) 2467.

[22] – Becoulet A., Gambier D.J., Rax J.-M., Samain A., Proc. 8th Top. Conf. on Applications of RF Power to Plasmas, Irvine (CA., USA) 1989, p. 197.

[23] – S.-I. Itoh, A. Fukuyama, K. Itoh, K. Nishikawa, J. Phys. Soc. Japan **54** (1985) 1800.

[24] – Faulkoner D.W., Plasma Phys. Contr. Fus. **29** (1987) 433.

[25] – Smithe D., Colestock P., Kammash T., Kashuba R., Phys. Rev. Lett. **60** (1988) 801.

[26] – Catto P.J., Lashmore-Davies C.N., Europ. Topical Conf. on Radiofrequency Heating and Current Drive of Fusion Devices, Bruxelles 1992, p. 165.

[27] – Lamalle P.U., Phys. Lett. **A 175** (1993) 45.

[28] – Kerbel G.D., McCoy M.G., Phys. Fluids **28** (1985) 3629.

[29] – Catto P.J., Myra J.R., Phys. Fluids **B 4** (1992) 187.

[30] – Gambier D.J., Samain A., Nucl. Fus. **25** (1985) 283.

[31] – Brambilla M., Phys. Lett. **A 188** (1994) 376.

[32] – Fried B.D., Conte S.D., *The Plasma Dispersion Function*, Academic Press (N.Y.) 1961.

[33] – Gautschi W., SIAM Rev. **9** (1967) 24.

[34] – Karney C.F.F., Phys. Fluids **21** (1978) 1584.

[35] – Karney C.F.F., Phys. Fluids **22** (1979) 2188.

[36] – T.H. Stix, Nucl. Fus. **15** (1975) 737.

[37] Brambilla M., Ottaviani M., Plasma Phys. Contr. Fus. **27** (1985) 1.

[38] Brambilla M., Chodura R., Hoffman J., Neuhauser J., Noterdaeme J.-M., Ryter F., Schubert R., Wesner F., 13th AIEA Conf. on Plasma Phys. and Contr. Nucl. Fusion Res., Washington (USA) 1990, Vol. 1, p. 723.

APPENDIX: PARAMETERS AND INPUT COMMONS OF THE TORIC CODE

A) Parameters to be set by the user:

LVRB Dimensions of the arrays of the field components (normal value 3; can be set to 2 if NVRB=2)

LMOD Dimensions of the arrays of the poloidal Fourier modes (must be ≥ NMOD)

LTT Dimensions of the arrays of the poloidal angle mesh (must be a power of 2 and satisfy LTT ≥ NTT)

LELM Dimensions of the arrays of the radial (psi) mesh (must satisfy LELM ≥ NELM+1)

NGAUS Number of Gauss quadrature points in each element (normal value 3)

NSPMX Dimensions of the arrays of ion species (must satisfy NSPMX ≥ NSPEC)

NPROF Dimensions of the arrays of the density and temperature profiles.

NMHD Dimensions of the arrays of the MHD profiles

B) Alphabetic list of the input variables in labeled commons:

ACONC(NSPMX) ion species concentrations (n_i/n_e).

AELLIP Ellipticity at the magnetic axis.

AICURR Plasma toroidal current (kA).

ALFANT Inclination of the antenna to the polidal plane (deg) (only ALFANT = 0 is implemented at present)

ANSLIM Threshold for onset of collisional regularization of ion-ion and Alfvén resonances.

ANTLC Propagation constant along the antenna.
If < 0 the current goes smoothly to zero at the antenna tips.

ANTLEN Half-length of the antenna (cm)

ATM(NSPMX) Atomic mass of the ion species (a.u.)

AZI(NSPMX) Atomic charge of the ion species (a.u.)

BZERO Toroidal magnetic field at the vessel center (T).

DENEC Central electron density (cm^-3)

DNEDGE Electron density at separatrix or limiter (cm^-3)

DNWALL Electron density at the wall (cm^-3)
(only with IMDEDG ≥ 0)

ENHCOL Factor for the enhancement of collisional damping.

ENHSTC Enhancement factor for the stochastic damping of IB waves

ENHRES Enhancement of the collisional regularization of ion-ion and Alfvén resonances (only with IALFVN = 1).

FREQCY Applied frequency (hz)

GAMVAC Evanescence length of ad-hoc wave for the suppression of spectral pollution (in units of the mesh step; only with IMDEDG = -2 or 0 < RPSIBW < RWALL)

GLDN Scrape-off density decay length, cm.

GLTE Scrape-off electron temperature decay length, cm.

GLTI Scrape-off ion temperature decay length, cm.

IALFVN Collisional regularization of ion-ion and Alfvén resonances.
= 1 - taken into account;
= 0 - ignored.

IBCANT Boundary condition at the antenna:
= 0 - One point (standard)
= 1 - Two points

IBPOL Control of the poloidal magnetic field model.
= 1 - taken into account;
= 0 - ignored (should be used with IFLR ≤ 0).

ICLPLO(3) Contour plots for E_+, E_-, E_z (ISOL = -1).
= 1 - made;
= 0 - skipped.

ICOLL Collisions:
= 1 - taken into account;
= 0 - ignored.

IFLR Choice of the plasma model for ions in the plasma.
= 1 - FLR effects included;
= 0 - FLR effects ignored.
= -1 - Order Reduction Algorithm
= -2 - Order Reduction with suppression of spectral pollution

IFLRE Choice of plasma model for electrons in the plasma.
= 1 - ELD, TTMP & mixed term taken into account;
= 0 - only ELD included.
= -1 - only (1/2)*TTMP included (with NVRB = 2)

IMDEDG Choice of plasma model behind the Faraday screen:
- = 2 - plasma, full dielectric tensor;
- = 1 - same, going to vacuum for the antenna;
- = 0 - cold dissipationless plasma;
- = -1 - vacuum;
- = -2 - vacuum with suppression of spectral pollution.

INTMHD MHD model:
- = 1 - Coefficients of the MHD configuration defined by the user and interpolated with splines;
- = 0 - Analytic default (pseudo)-equilibrium.

IOUT Output level.
- = 0 - reduced output;
- = 1 - normal output.
- = 2 - detailed output (for tests only);

IPLBEQ Plots of the wave magnetic field along the equatorial plane.
- = 1 - done;
- = 0 - skipped.

IPLEEQ Plots of the wave electric field along the equatorial plane.
- = 1 - done;
- = 0 - skipped.

IPLEQL Plots of the dielectric tensor and index squared along the equatorial plane (ISOL = 0).
- = 1 - done;
- = 0 - skipped.

IPLDIV Plots of div.E along the equatorial plane.
- = 1 - done;
- = 0 - skipped.

IPLLEV Quality of the plot output (1 or 4 plots per page)
- = 1 - high (1 plot per page);
- = 0 - low (4 plots per page).

IPLMAG Plots of the MHD tokamak configuration (ISOL = 0).
- = 1 - done;
- = 0 - skipped.

IPLMOD Plots of the poloidal mode coeffs vs radius (ISOL = -1).
- = 1 - done;
- = 0 - skipped.

IPLNTQ Plots of density and temperature profiles (ISOL = 0).
- = 1 - done;
- = 0 - skipped.

IPLOPW Plots of power deposition profiles.
= 1 - done;
= 0 - skipped.

IPLOPY Plots of the Poynting flux profile.
= 1 - done;
= 0 - skipped.

IPLTHT Plots of the dielectric tensor vs theta and of its Fourier transform (ISOL = 0).
= 1 - done;
= 0 - skipped.

IPRODF Density and temperature profiles:
= 1 - entered by the user;
= 0 - default

IQTOR Toroidal broadening of the cyclotron resonances.
= 1 - taken into account;
= 0 - ignored.

ISOL Call to the solver.
= 1 - solver called (TORICA);
= 0 - skipped (exploratory runs, TORICT).
= -1 - skipped (solution read from disk, TORICB)

ISTOCH Ad-hoc IBW damping.
= 1 - taken into account;
= 0 - ignored.

IWDISK Results to be written on disk (ISOL = 1 only)
= 1 - yes;
= 0 - no.

MAINSP Majority ion species.

NELM Number of radial elements.

NMOD Number of poloidal modes (preferably odd).

NPHI Toroidal wavenumber.

NSPEC Number of ion species.

NTT Number of points in theta (power of 2)

NVRB Number of components of the electric field:
= 3 - Ez taken into account;
= 2 - Ez ignored.

PPNEE Outer power in the default density profile.

PPNEI Inner power in the default density profile.

PPTEE Outer power in the default electron temperature profile.

PPTEI	Inner power in the default electron temperature profile.
PPTIE	Outer power in the default ion temperature profile.
PPTII	Inner power in the default ion temperature profile.
QBFRAC	Minimum effective beta in the stoch. damping of IB waves.
QLBSTH	Threshold of (k^*ri)2/2 for the onset of IBW damping.
QLBEPS	Enhancement factor for IBW stoch. damping.
QMSHBW	Minimum allowd IBW wavelength (in units of the mesh step; ignored if ≤ 0).
RANT	Radius of the antenna position (cm).
RFARSH	Radius of the Faraday shield position (cm)
RPLASM	Plasma radius (cm)
RPSIBW	Maximum radius allowing IBW propagation.
RSHIFT	Shafranov shift (cm).
RTOR	Major radius (cm).
RWALL	Vessel radius (cm).
TEEDGE	Electron temperature at the separatrix (keV)
TEMPEC	Central electron temperature (keV)
TEMPIC(NSPMX)	Central ion temperature (keV)
TEWALL	Electron temperature at the wall (keV) (only with IMDEDG ≥ 0)
TIEDGE(NSPMX)	Ion temperature at the separatrix (keV)
TIWALL(NSPMX)	Ion temperature at the wall (keV) (only with IMDEDG ≥ 0)
ZELLIP	Ellipticity of the outer magnetic surface.
ZTRIAN	Triangularity of the outer magnetic surface.

TABLE I

TOKAMAK PARAMETERS:

Major radius	=	165.000	cm
Plasma radius (separatrix)	=	50.000	cm
Faraday Shield radius	=	55.000	cm
Antenna radius	=	60.000	cm
Vacuum vessel radius	=	70.000	cm
Central magnetic field	=	2.000	Tesla
Toroidal plasma current	=	750.000	kA
Safety factor q on axis	=	1.118	
Safety factor q at separatrix	=	2.698	
Shift of the magnetic axis	=	4.500	cm
Triangularity	=	-0.150	
Ellipticity: at plasma edge	=	1.600	
Ellipticity: at magnetic axis	=	1.000	

PLASMA PARAMETERS

Central electron density	=	8.000E+13	cm-3
Central electron temperature	=	2.000	keV
Electron density at the limiter	=	2.000E+13	cm-3
Electron temperature at the lim.	=	0.400	keV
Ion Species 1 :			
Charge (atomic units)		1.0	
Mass (atomic units)		2.0	
Concentration (Ni/Ne)	=	0.950	
Central temperature	=	2.000	keV
Harmonic resonance at X	=	-2.703	cm
Ion Species 2 :			
Charge (atomic units)		1.0	
Mass (atomic units)		1.0	
Concentration (Ni/Ne)	=	0.050	
Central temperature	=	2.000	keV
Fundam. resonance at X	=	-2.703	cm

Default profiles (1 - psi^pi)^pe

Density:	pi =	3.00	pe =	1.00
Elec. temperature:	pi =	2.00	pe =	1.00
Ion temperature:	pi =	2.00	pe =	1.00

Parameters of the scrape-off plasma:

Decay length of n	=	2.000	cm
Decay length of Te	=	5.000	cm
Decay length of Ti	=	5.000	cm
Electron density at the F.S.	=	4.797E+12	cm-3
Electron temperature at the F.S.	=	0.134	keV
Electron density at the wall	=	4.001E+12	cm-3
Electron temperature at the wall	=	0.027	keV

PLASMA MODEL:

Ions: finite Larmor radius approximation
Ion Bernstein waves damped

k.rho_i	>	0.50
Factor in exp(-q*w^2)	q =	2.00
Enhancement factor	=	5.00

Parallel electric field taken into account
Electrons: Landau damping and TTMP with mixed term
Collisions omitted
Poloidal magnetic field taken into account
Toroidal broadening of IC resonances taken into account

Plasma extending to the wall

WAVE AND ANTENNA PARAMETERS

Frequency	=	30.000	Mhz
Toroidal wavenumber NPHI	=	4	
Equiv. parallel index	=	3.856	
Feeders at the ends in push-pull			
Half-length of the antenna	=	50.000	cm
(LC)-constant of the antenna	=	1.500	

MESH PARAMETERS

Number of poloidal modes:	21
Number of poloidal mesh points	64
Number of radial elements:	301
Number of radial mesh points:	302
Psi at the plasma edge:	0.680
Psi at the Faraday shield:	0.757
Psi at the antenna:	0.837
Faraday shield at meshpoint:	229
Antenna at meshpoint:	253

TABLE 2
(n_ϕ = 20)

Description of the run and CPU time on the CRAY-1

(1) Complete, 31 poloidal modes (64 pts)	837.0 s
(2) Complete, 25 poloidal modes	546.6 s
(3) Complete, 19 poloidal modes	350.0 s
(4) Complete, 15 poloidal modes (32 pts)	183.7 s
(5) Complete, 11 poloidal modes	119.4 s
(1a) Same as (1), with plasma extending to the wall	859.3 s
(3a) Same as (3), without toroidal broadening	337.7 s
(3b) Same as (3), $B_\theta = 0$	236.2 s
(6) ORA, 19 poloidal modes	209.9 s
(7) ORA, 15 poloidal modes (32 pts)	115.9 s
(8) ORA, 11 poloidal modes	72.1 s
(9) ORA, 7 poloidal modes (16 pts, 151 rad. elem.)	17.2 s
(9a) Same with $E_z = 0$	9.6 s
(10) RAYIC (Ray Tracing)	6.0 s
(11) FELICE (slab), 25 n_y modes	74.9 s

a) Repartition of the power

	minority (fundam)	majority (1st harm)	electrons	Bernstein waves
(1)	79.89%	7.61%	10.98%	1.52%
(2)	79.80%	7.63%	10.99%	1.58%
(3)	79.57%	7.67%	11.02%	1.74%
(4)	79.52%	7.68%	11.03%	1.78%
(5)	79.15%	7.67%	11.05%	2.14%
(1a)	80.37%	7.68%	10.55%	1.40%
(3a)	77.37%	7.81%	12.81%	2.00%
(3b)	76.84%	8.07%	13.35%	1.73%
(6)	75.52%	11.47%	13.01%	-
(7)	75.34%	11.61%	13.05%	-
(8)	75.90%	11.47%	12.63%	-
(9)	76.65%	11.34%	12.01%	-
(9a)	76.98%	11.39%	11.63%	-
(10)	68.70%	13.01%	10.33%	-
(11)	71.02%	13.87%	13.41%	1.69%

b) Global balance (MW/m3.A)

	absorbed in the plasma	Poynting flux	<J.E>
(1)	0.012430	0.013086	0.013085
(2)	0.011223	0.012297	0.012297
(3)	0.011602	0.012727	0.012726
(4)	0.009609	0.010553	0.010552
(5)	0.010516	0.011558	0.011557
(1a)	0.060905	0.065857	0.066349
(3a)	0.012570	0.012647	0.012646
(3b)	0.012866	0.013886	0.013884
(6)	0.014121	0.014353	0.014350
(7)	0.012767	0.012970	0.012969
(8)	0.012299	0.012467	0.012465
(9)	0.011545	0.011670	0.011668
(9a)	0.011686	0.011686	0.011686
(10)	-	-	-
(11)	0.012489	-	0.012489

TABLE 3
($n\phi = 4$)

Description of the run and CPU time on the CRAY-1

(1) Complete, 31 poloidal modes (64 pts)	832.0 s
(2) Complete, 19 poloidal modes	322.9 s
(2a) Same as (2), $B\theta = 0$	236.2 s
(3) ORA, 19 poloidal modes	215.7 s
(4) RAYIC (Ray Tracing)	6.2 s
(5) FELICE (slab), 25 n_y modes	74.7 s

a) Repartition of the power

	minority (fundam)	majority (1st harm)	electrons	Bernstein waves
(1)	72.13%	24.97%	0.45%	2.45%
(2)	84.87%	13.85%	0.43%	0.85%
(2a)	75.77%	20.83%	0.01%	3.39%
(3)	87.57%	12.39%	0.04%	-
(4)	75.10%	20.21%	4.64%	-
(5)	46.84%	20.76%	0.01%	32.40%

b) Global balance (MW/m3.A)

	absorbed in the plasma	Poynting flux	<J.E>
(1)	0.020038	0.014852	0.014837
(2)	0.015650	0.014681	0.014673
(2a)	0.012866	0.013886	0.013884
(4)	-	-	-
(5)	0.013029	-	0.013029

Figure Captions.

Fig. 1 – Density, temperature and q-profiles for the standard ASDEX Upgrade case. The 'separatrix' is at $\psi = 0.68$, where $q \simeq 3.5$; the values of q outside the plasma are irrelevant.

Fig. 2 – The dielectric tensor elements L, R and S, the perpendicular index squared of the Fast Wave; $k_\parallel$ for the $m_\vartheta = 0$ component and $\omega/k_\parallel v_{the}$ for the electrons along the equatorial plane. Standard ASDEX Upgrade case: $n_\varphi = 20$, plasma parameters in Table 1.

Fig. 3 – The FLR contributions $\lambda_i^{(2)}$, $\rho_i^{(2)}$ to the dielectric tensor; the correction to $\lambda_i^{(2)}$ which simulates stochastic damping of Berstein waves; perpendicular index squared of the Bernstein wave; value of $k_\perp^2 v_{thH}^2/2\Omega_{cH}^2$ for the Bernstein wave along the equatorial plane.

Fig. 4 – Wave electric and magnetic field components along the equatorial plane, standard ASDEX Upgrade case.

Fig. 5 – Power deposition profiles and Poynting flux for 1 kA in the antenna, standard ASDEX Upgrade case.

Fig. 6 – Contour plots of E_+, E_-, E_z in the poloidal plane, standard ASDEX Upgrade case.

Fig. 7 – Power deposition profiles for the standard ASDEX Upgrade case, but: a) without toroidal broadening of cyclotron resonances; b) with $B_\vartheta = 0$.

Fig. 8 – Wave fields along the equatorial plane, power deposition profiles and Poynting flux, and contour plots of $E_\pm$ for the standard ASDEX Upgrade case, solved with the Order Reduction Algorithm.

Fig. 9. – Results of the ray tracing code RAYIC for the standard ASDEX Upgrade case.

Fig. 10 – Results of the FELICE slab geometry code for the standard ASDEX Upgrade case.

Fig. 11 – Compressional component of the wave magnetic field and power deposition profiles in a solution with spectral pollution in vacuum. $n_\varphi = 4$, plasma parameters in Table 1.

Fig. 12 – Wave electric and magnetic field, power deposition profiles and Poynting flux for the same case as in fig. 11; vacuum layer integrated with $B_\vartheta = 0$.

Fig. 13 – Contour plots of $E_\pm$ in the poloidal plane for the case of fig. 12.

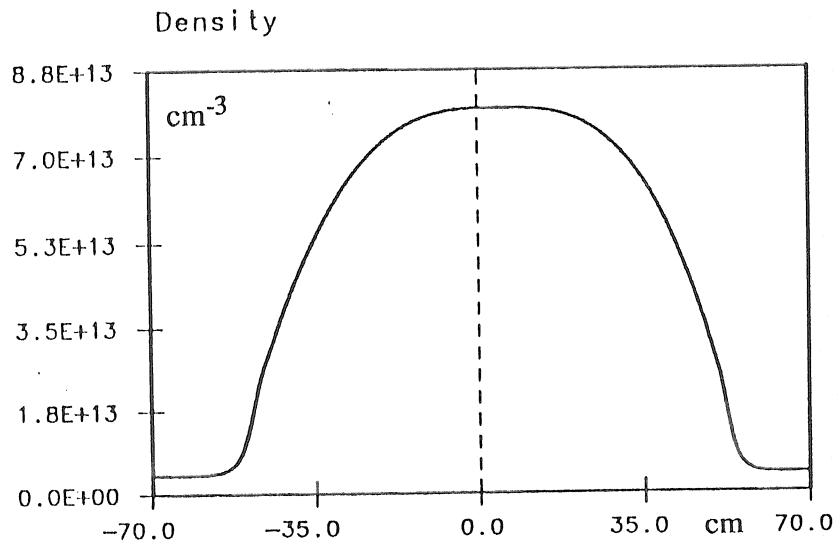
Density
8.8E+13
7.0E+13
5.3E+13
3.5E+13
1.8E+13
0.0E+00
cm-3
-70.0
-35.0
0.0
35.0
cm
70.0

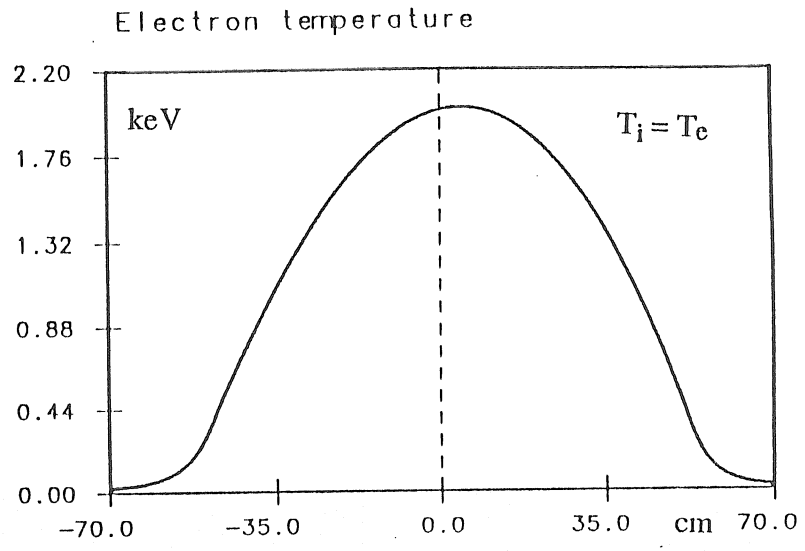
Electron temperature
2.20
1.76
1.32
0.88
0.44
0.00
keV
Ti = Te
-70.0
-35.0
0.0
35.0
cm
70.0

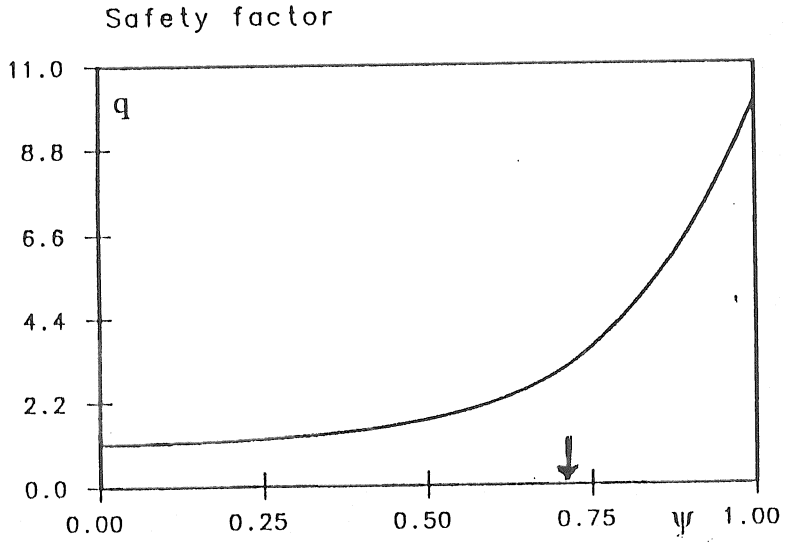
Safety factor
11.0
8.8
6.6
4.4
2.2
0.0
q
0.00
0.25
0.50
0.75
ψ
1.00

Fig. 1

Fig. 2

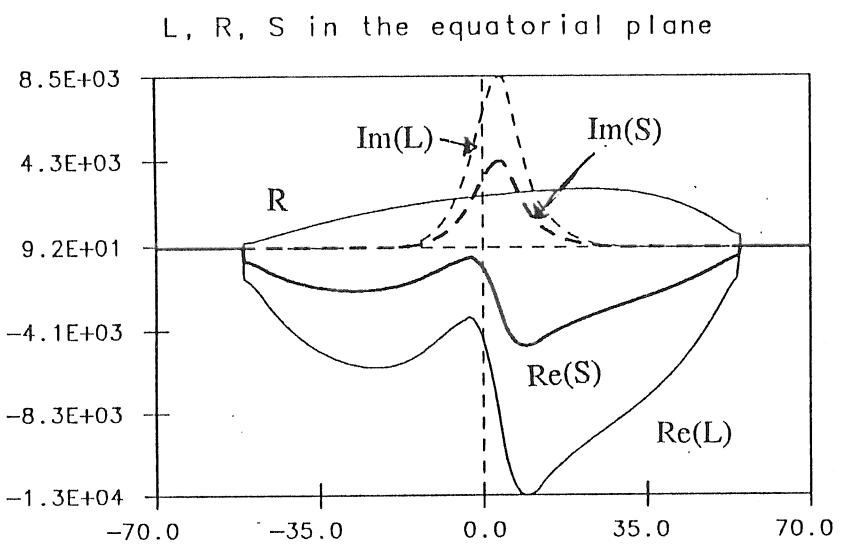
L, R, S in the equatorial plane
8.5E+03
4.3E+03
9.2E+01
-4.1E+03
-8.3E+03
-1.3E+04
-70.0
-35.0
0.0
35.0
70.0
Im(L)
Im(S)
R
Re(S)
Re(L)

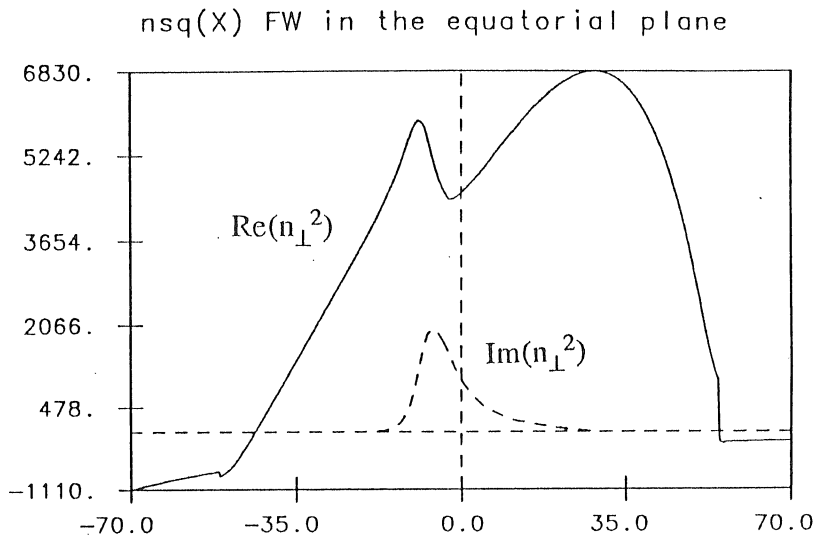
nsq(X) FW in the equatorial plane
6830.
5242.
3654.
2066.
478.
-1110.
-70.0
-35.0
0.0
35.0
70.0
Re(n⊥²)
Im(n⊥²)

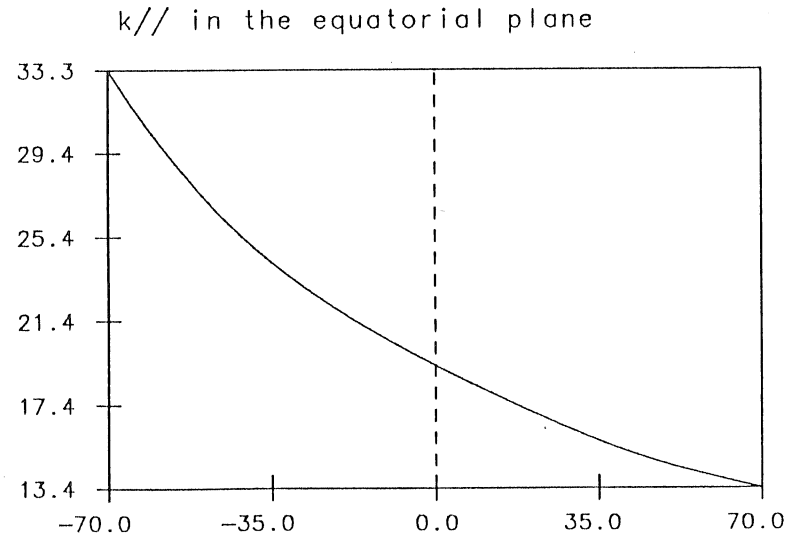
k// in the equatorial plane
33.3
29.4
25.4
21.4
17.4
13.4
-70.0
-35.0
0.0
35.0
70.0

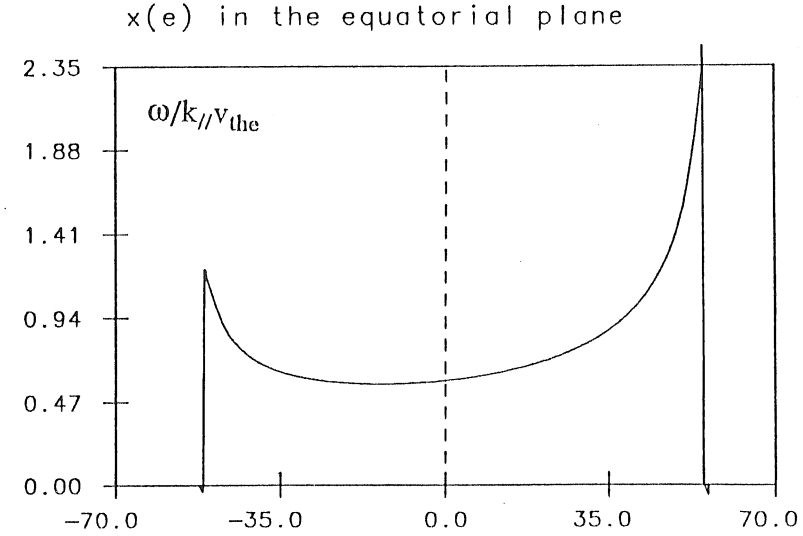
x(e) in the equatorial plane
2.35
1.88
1.41
0.94
0.47
0.00
-70.0
-35.0
0.0
35.0
70.0
ω/k//vthe

Fig. 3

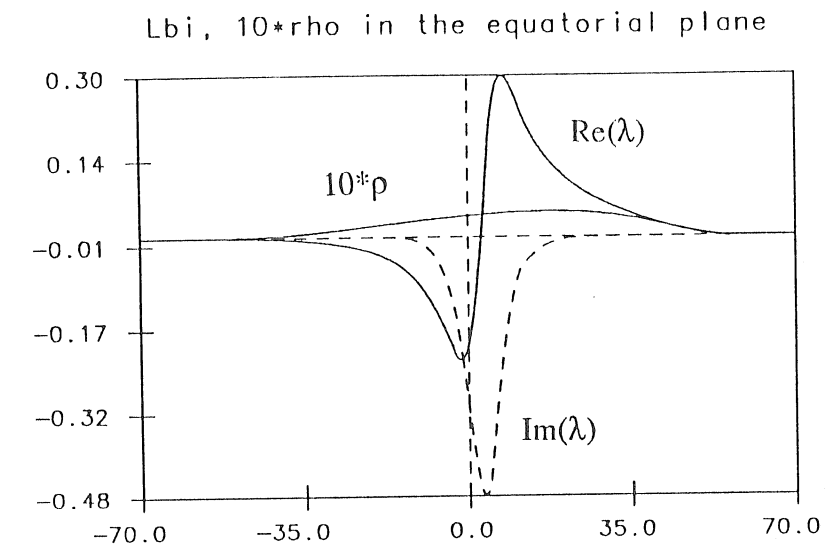
Lbi, 10*rho in the equatorial plane
0.30
0.14
-0.01
-0.17
-0.32
-0.48
-70.0
-35.0
0.0
35.0
70.0
Re(λ)
10*ρ
Im(λ)

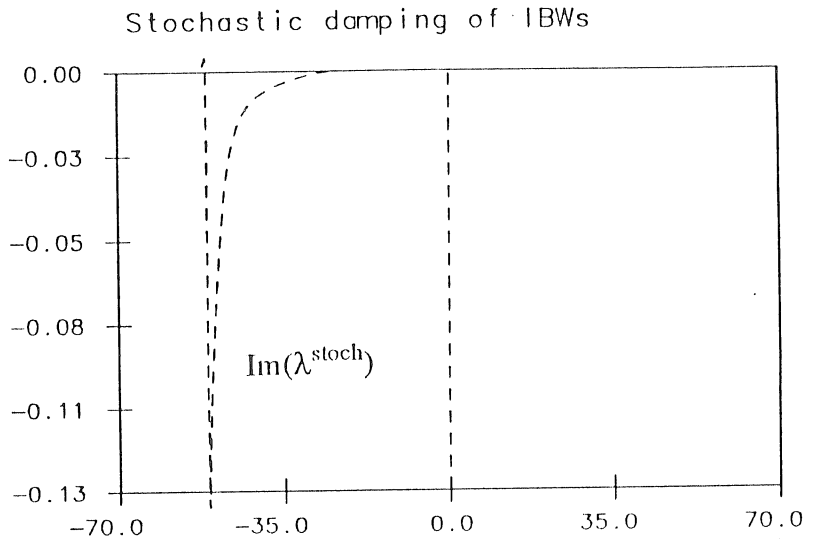
Stochastic damping of IBWs
0.00
-0.03
-0.05
-0.08
-0.11
-0.13
-70.0
-35.0
0.0
35.0
70.0
Im(λ^stoch)

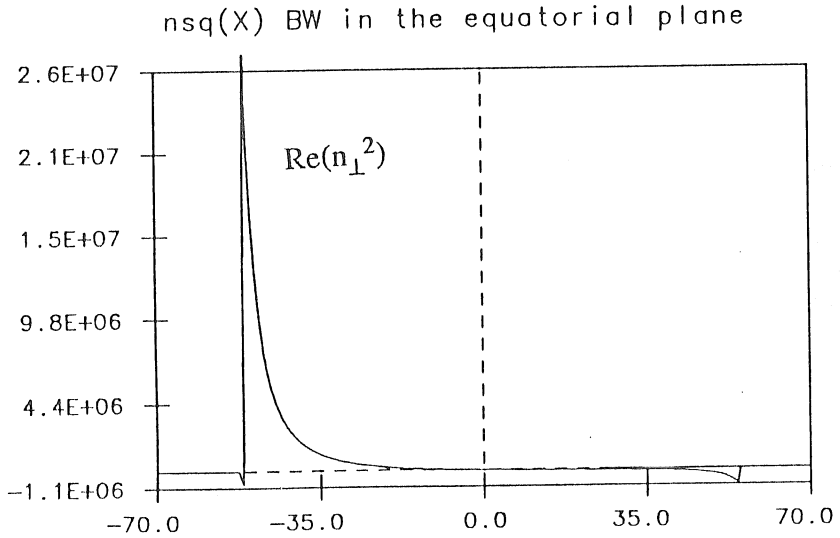
nsq(X) BW in the equatorial plane
2.6E+07
2.1E+07
1.5E+07
9.8E+06
4.4E+06
-1.1E+06
-70.0
-35.0
0.0
35.0
70.0
Re(n⊥^2)

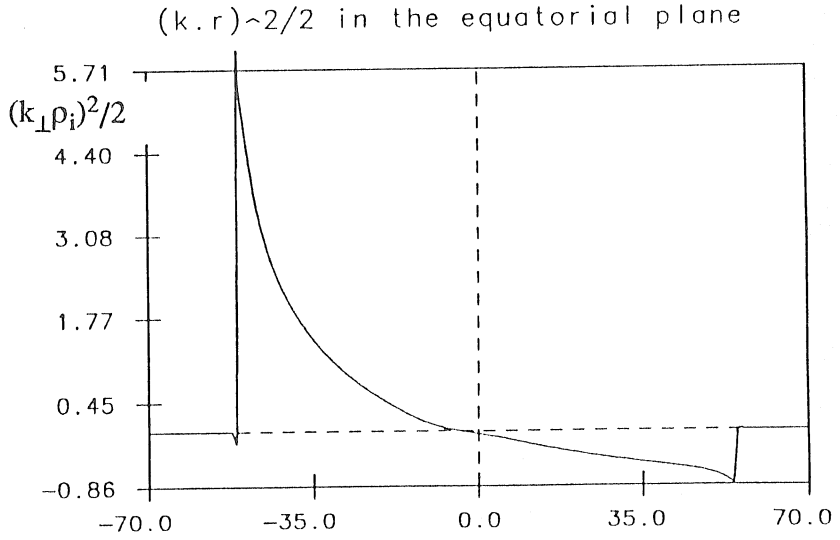
(k.r)~2/2 in the equatorial plane
5.71
(k⊥ρi)^2/2
4.40
3.08
1.77
0.45
-0.86
-70.0
-35.0
0.0
35.0
70.0

Fig. 4a

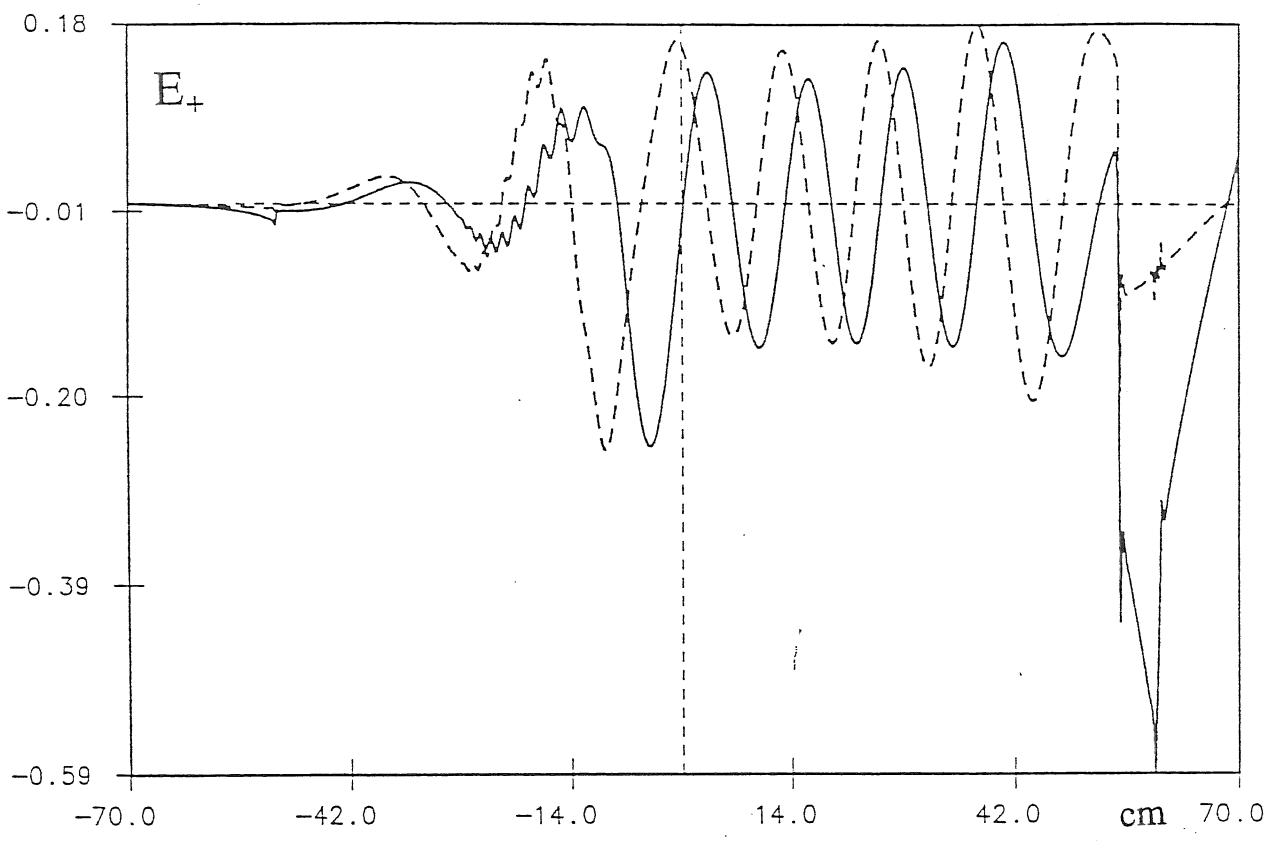
0.18
E+
-0.01
-0.20
-0.39
-0.59
-70.0
-42.0
-14.0
14.0
42.0
cm
70.0

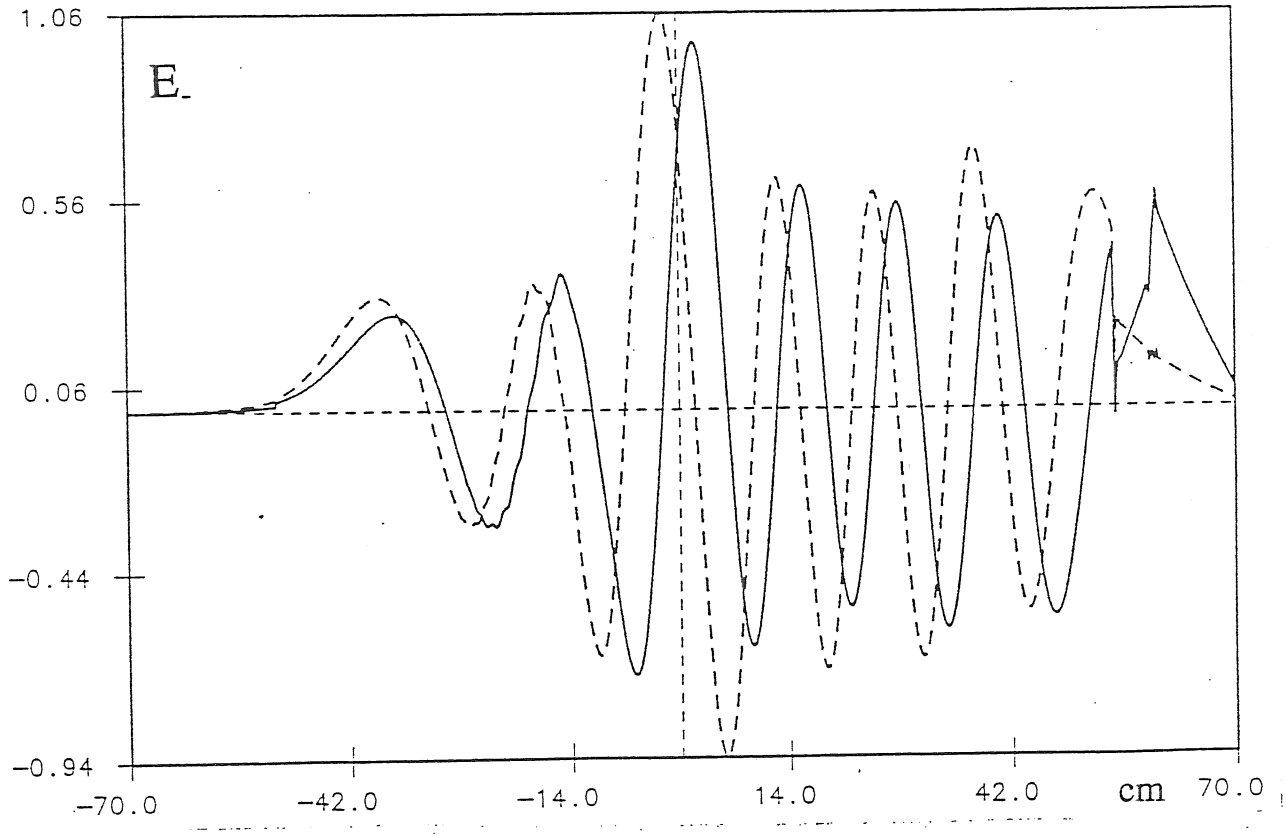
1.06
E-
0.56
0.06
-0.44
-0.94
-70.0
-42.0
-14.0
14.0
42.0
cm
70.0

Fig. 4b

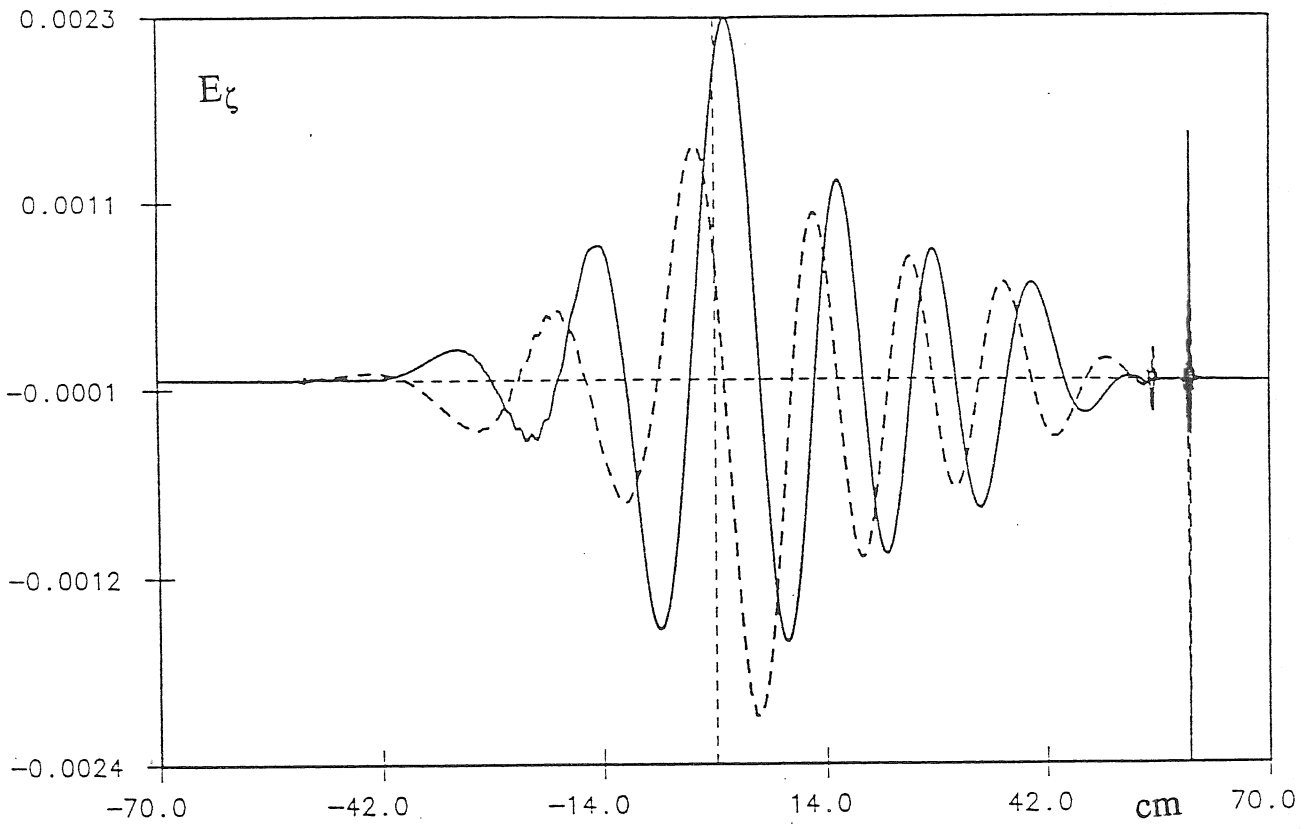
0.0023
E_ζ
0.0011
-0.0001
-0.0012
-0.0024
-70.0
-42.0
-14.0
14.0
42.0
cm
70.0

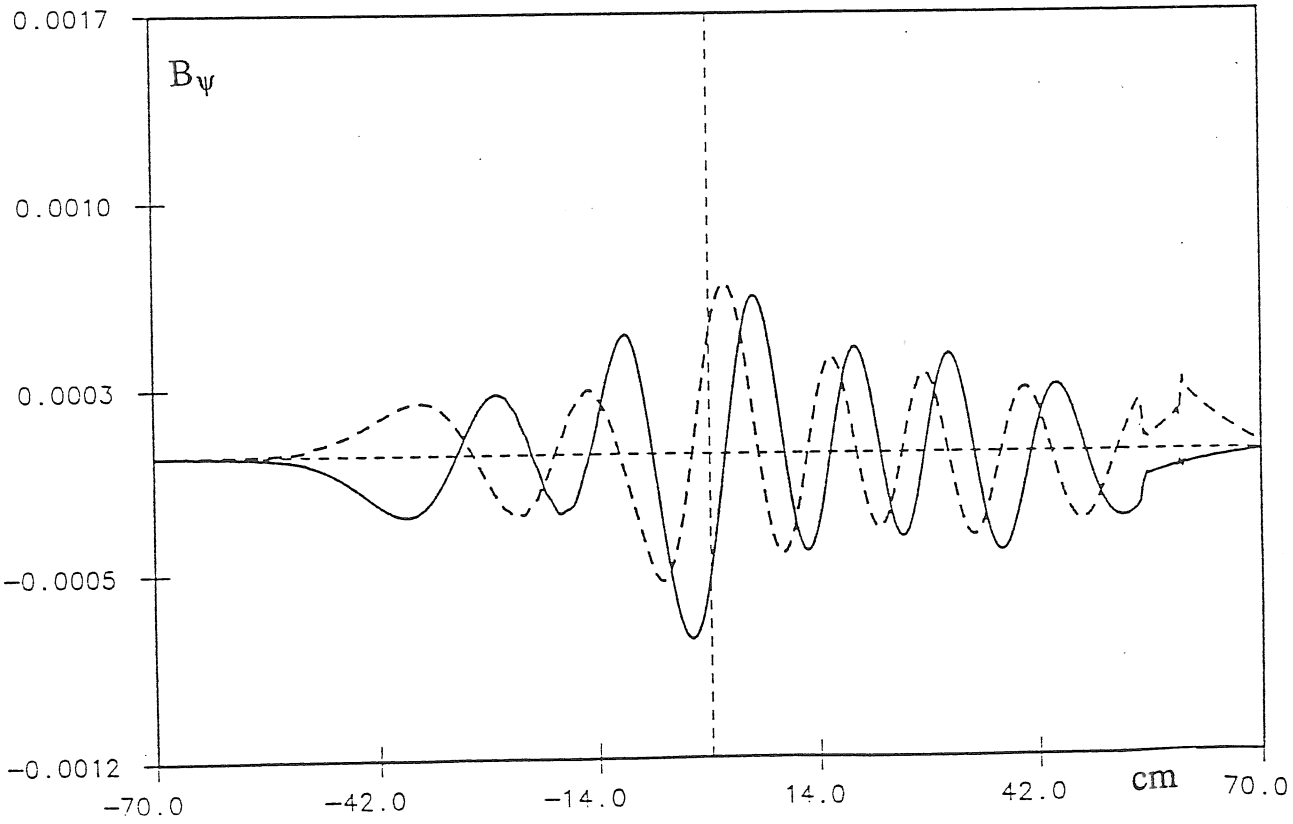
0.0017
B_ψ
0.0010
0.0003
-0.0005
-0.0012
-70.0
-42.0
-14.0
14.0
42.0
cm
70.0

Fig. 4c

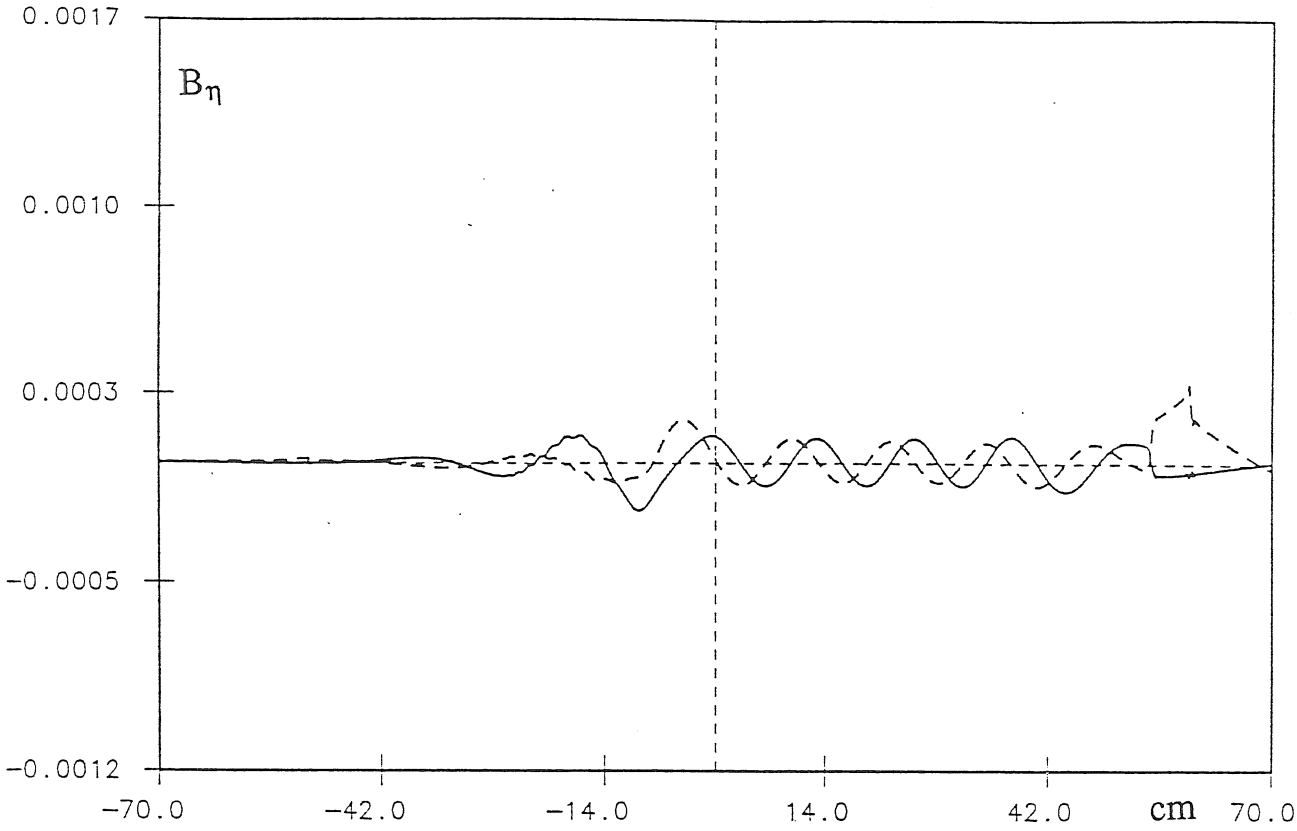
0.0017
B_η
0.0010
0.0003
-0.0005
-0.0012
-70.0
-42.0
-14.0
14.0
42.0
cm
70.0

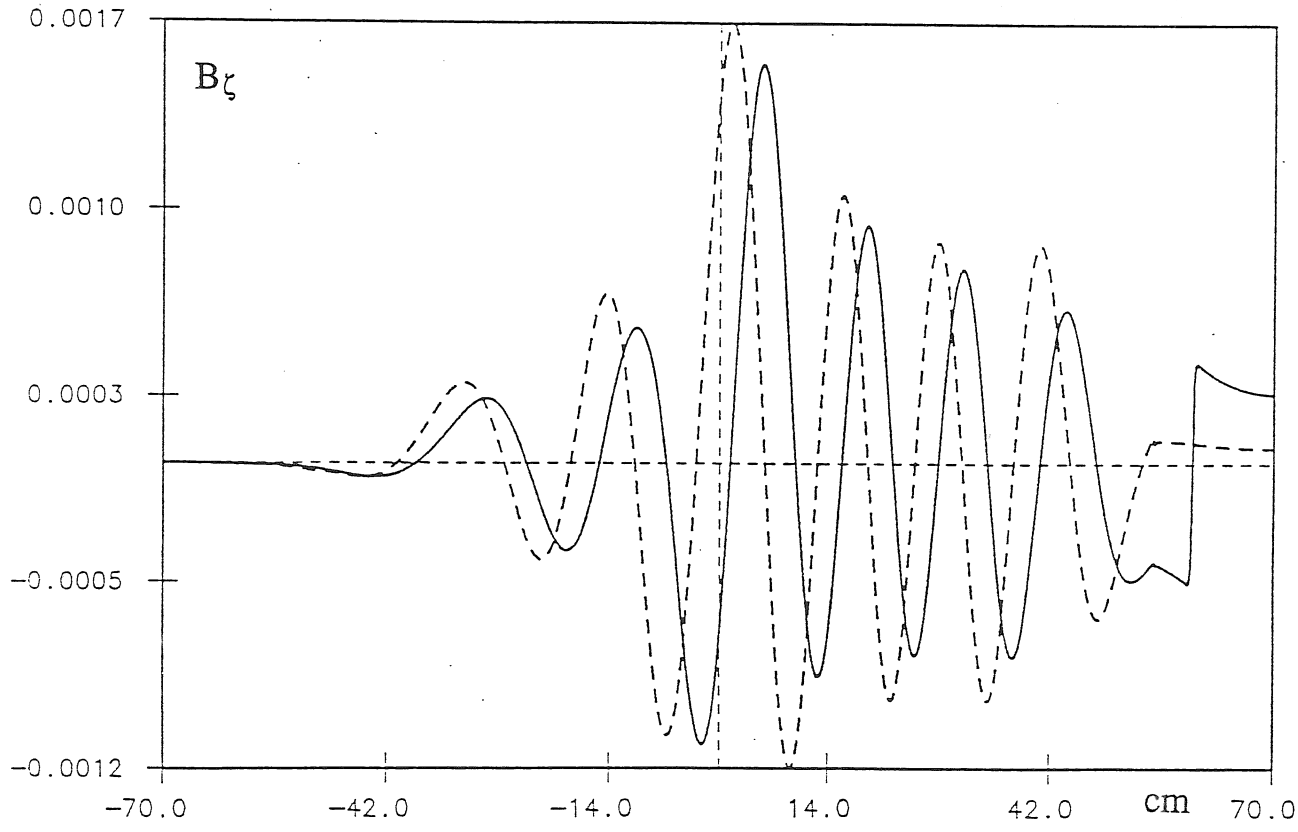
0.0017
B_ζ
0.0010
0.0003
-0.0005
-0.0012
-70.0
-42.0
-14.0
14.0
42.0
cm
70.0

Fig. 4d

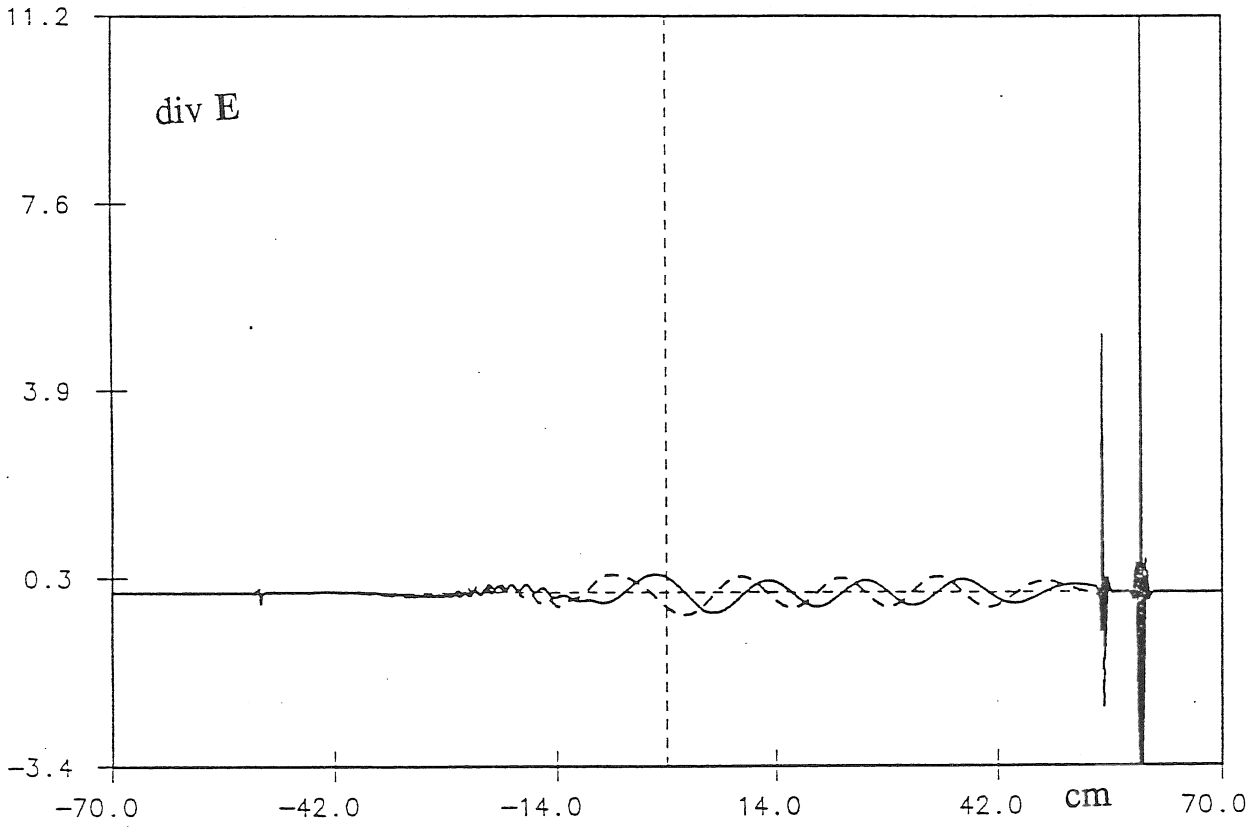

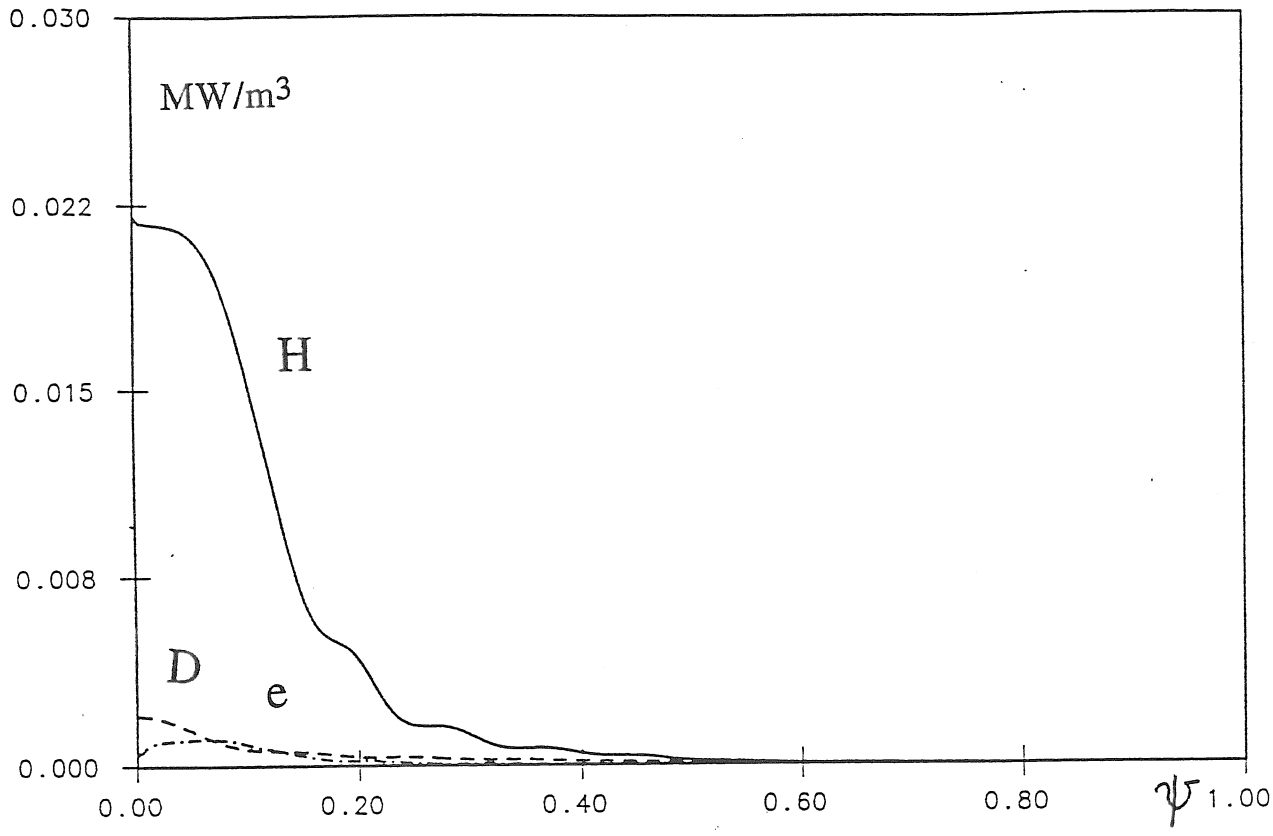
0.030
MW/m3
0.022
H
0.015
0.008
D
e
0.000
0.00
0.20
0.40
0.60
0.80
ψ 1.00

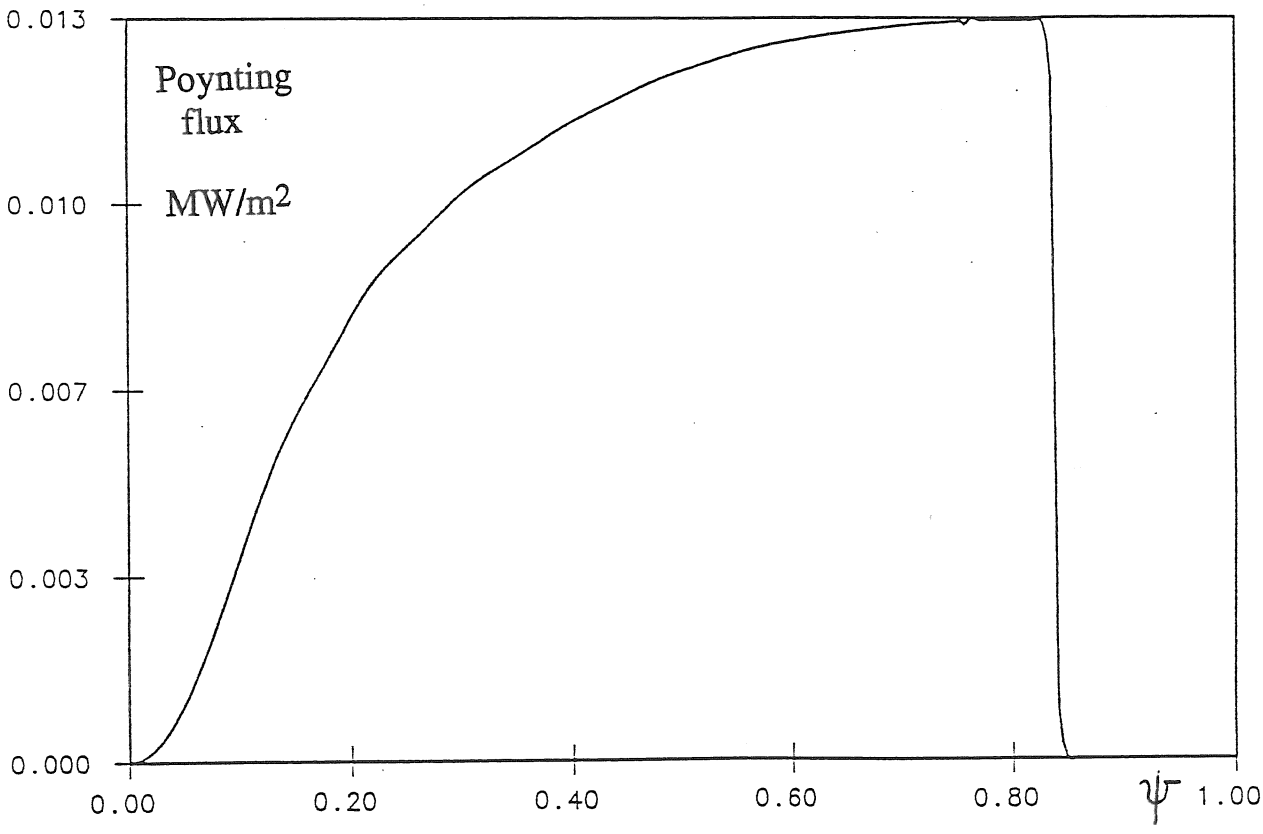
0.013
Poynting
flux
0.010
MW/m2
0.007
0.003
0.000
0.00
0.20
0.40
0.60
0.80
ψ 1.00

Fig. 5

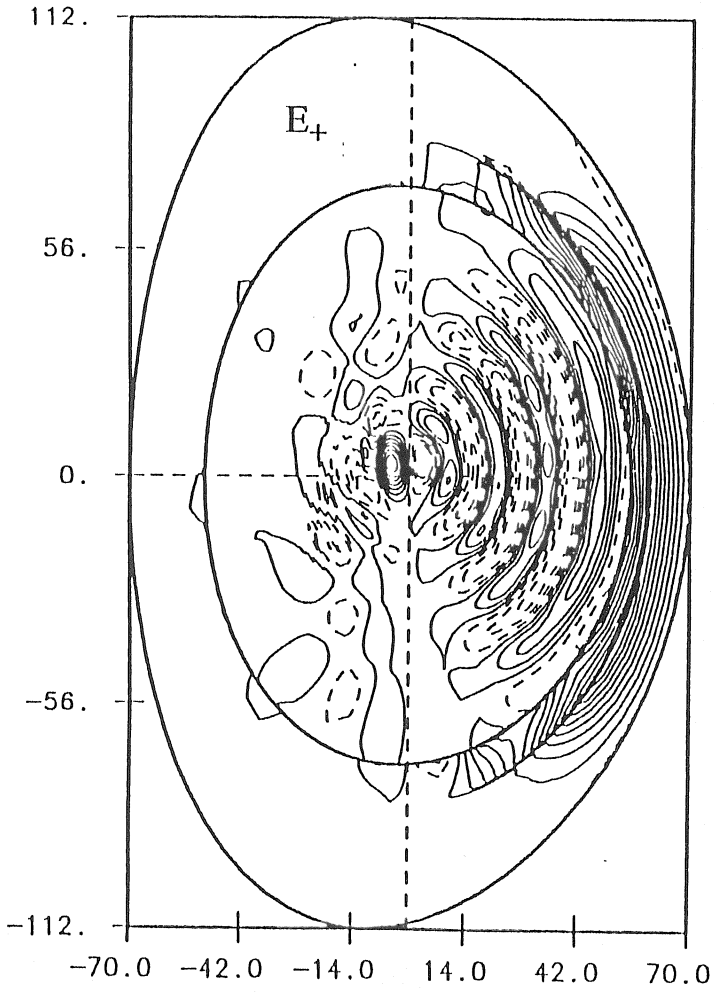
112.
56.
0.
-56.
-112.
E_+
-70.0
-42.0
-14.0
14.0
42.0
70.0

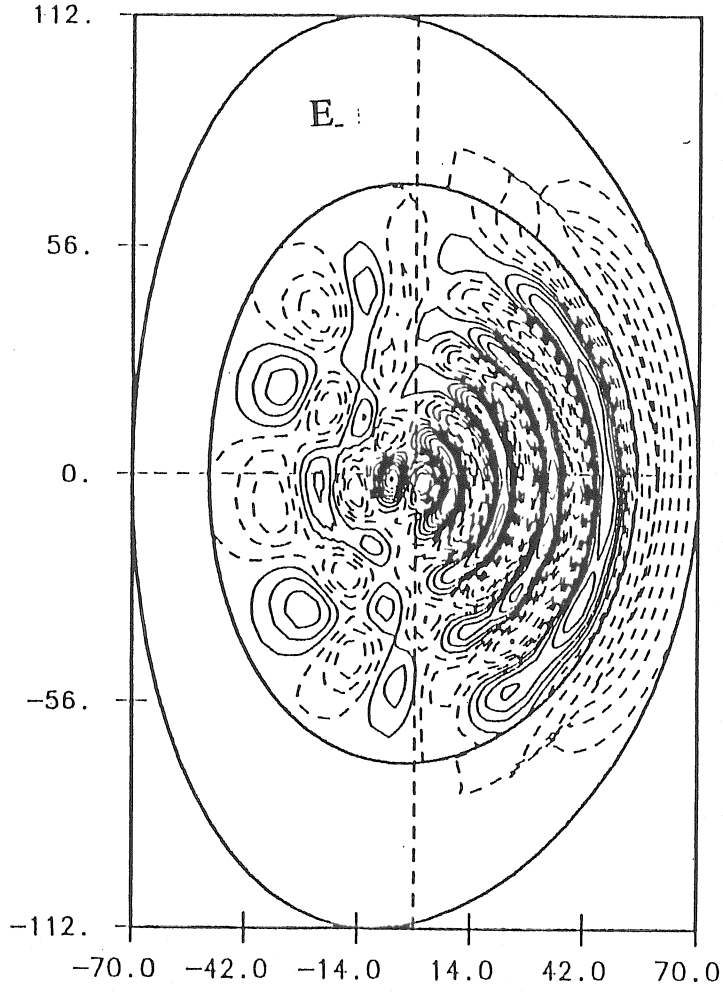
112.
56.
0.
-56.
-112.
E_-
-70.0
-42.0
-14.0
14.0
42.0
70.0

Fig. 6a

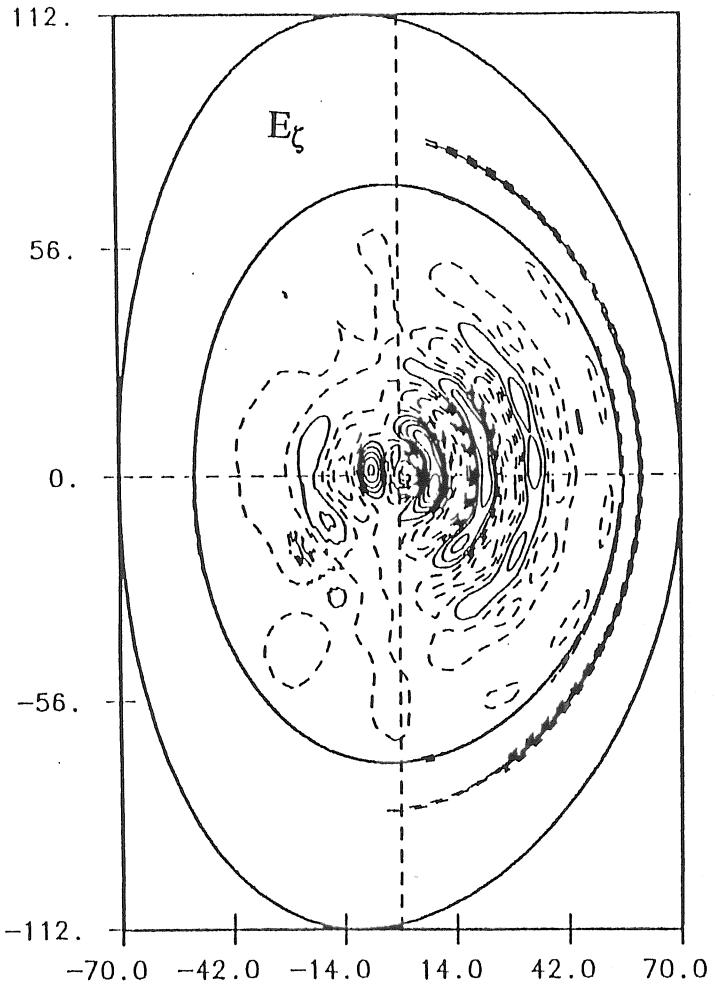

Fig. 6b

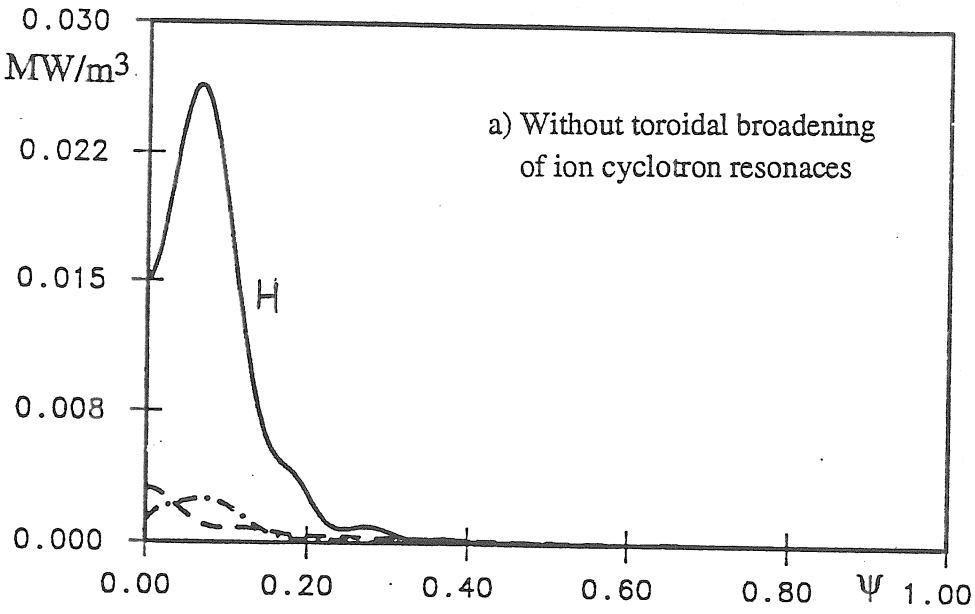
0.030
MW/m3
0.022
0.015
0.008
0.000
a) Without toroidal broadening
of ion cyclotron resonaces
H
0.00
0.20
0.40
0.60
0.80
Ψ
1.00

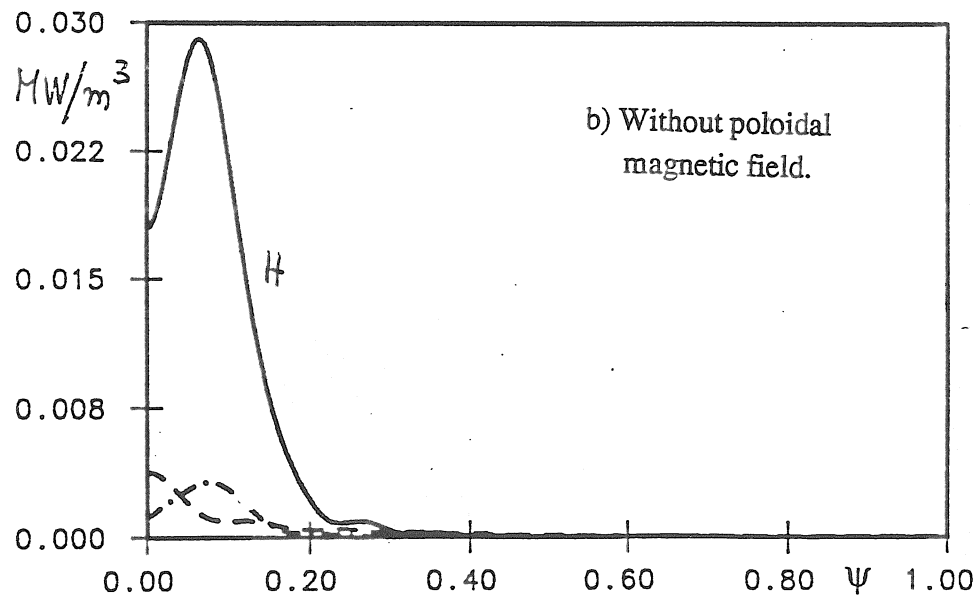
0.030
MW/m3
0.022
0.015
0.008
0.000
b) Without poloidal
magnetic field.
H
0.00
0.20
0.40
0.60
0.80
Ψ
1.00

Fig. 7

Fig. 8a

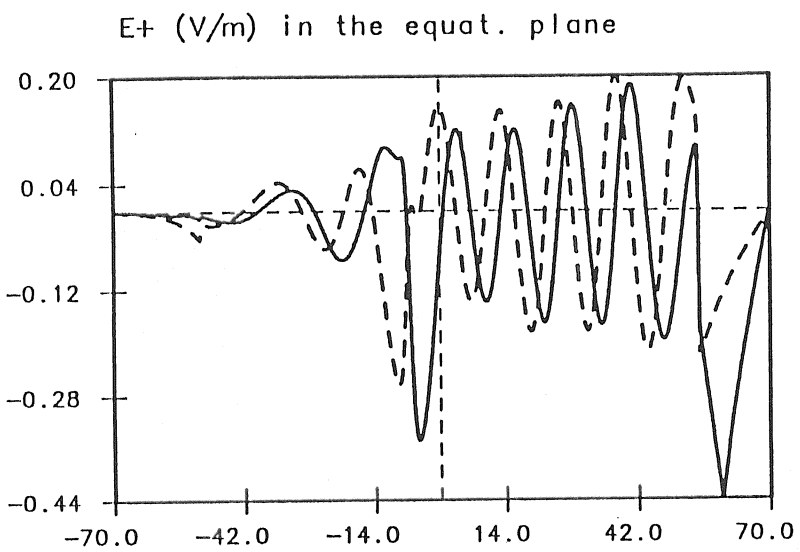
E+ (V/m) in the equat. plane
0.20
0.04
-0.12
-0.28
-0.44
-70.0
-42.0
-14.0
14.0
42.0
70.0

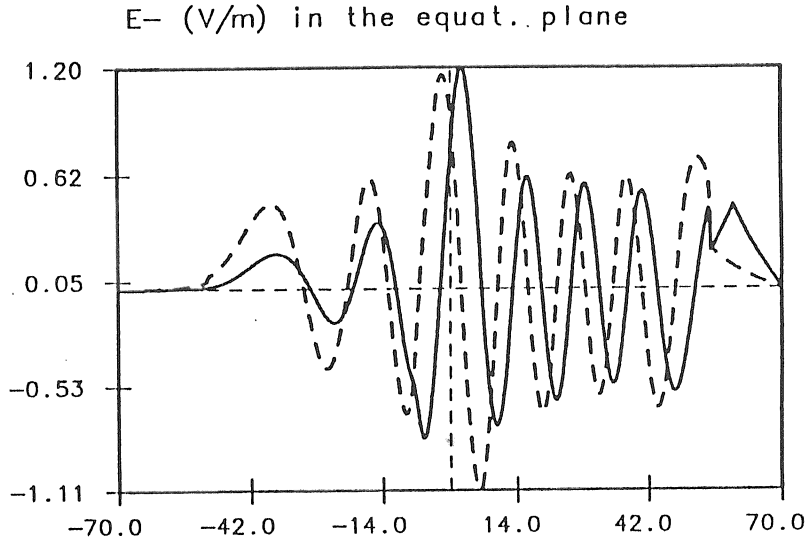
E- (V/m) in the equat. plane
1.20
0.62
0.05
-0.53
-1.11
-70.0
-42.0
-14.0
14.0
42.0
70.0

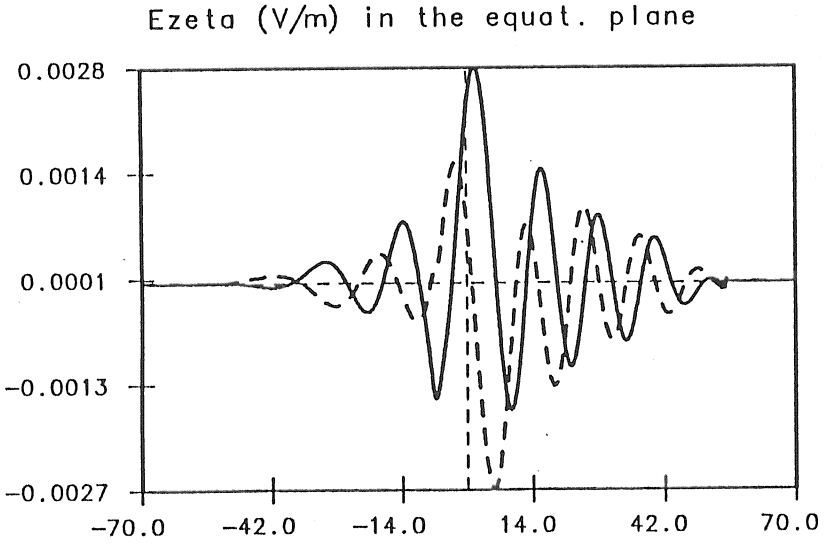
Ezeta (V/m) in the equat. plane
0.0028
0.0014
0.0001
-0.0013
-0.0027
-70.0
-42.0
-14.0
14.0
42.0
70.0

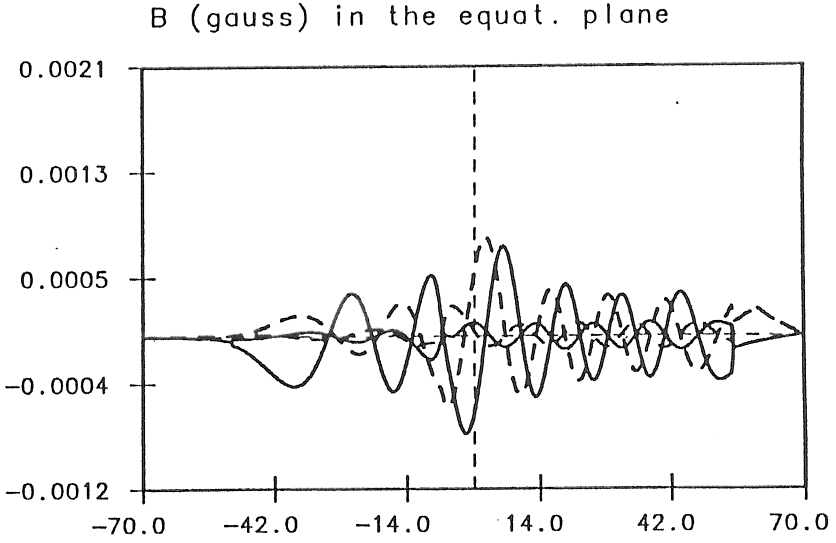
B (gauss) in the equat. plane
0.0021
0.0013
0.0005
-0.0004
-0.0012
-70.0
-42.0
-14.0
14.0
42.0
70.0

Fig. 8b

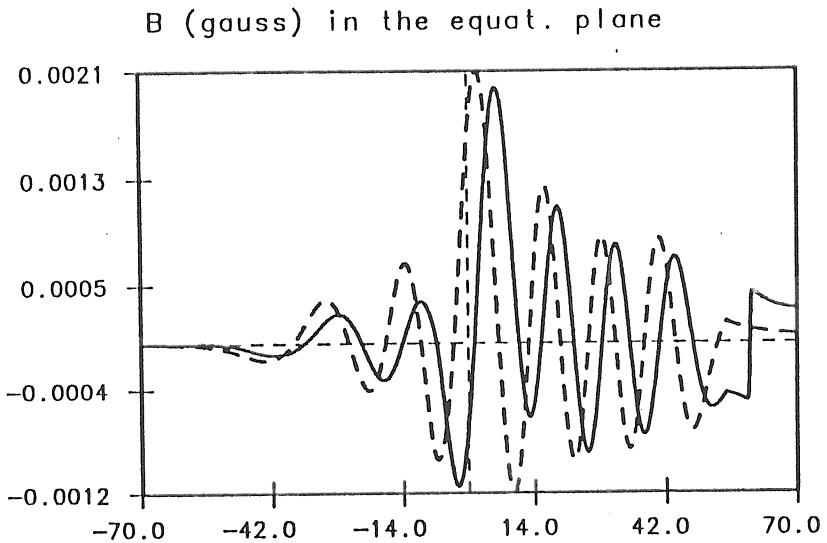
B (gauss) in the equat. plane
0.0021
0.0013
0.0005
-0.0004
-0.0012
-70.0
-42.0
-14.0
14.0
42.0
70.0

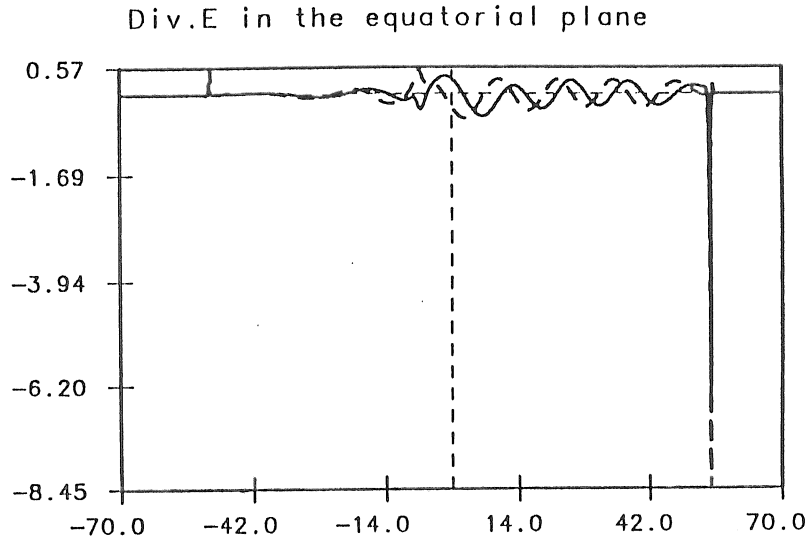
Div.E in the equatorial plane
0.57
-1.69
-3.94
-6.20
-8.45
-70.0
-42.0
-14.0
14.0
42.0
70.0

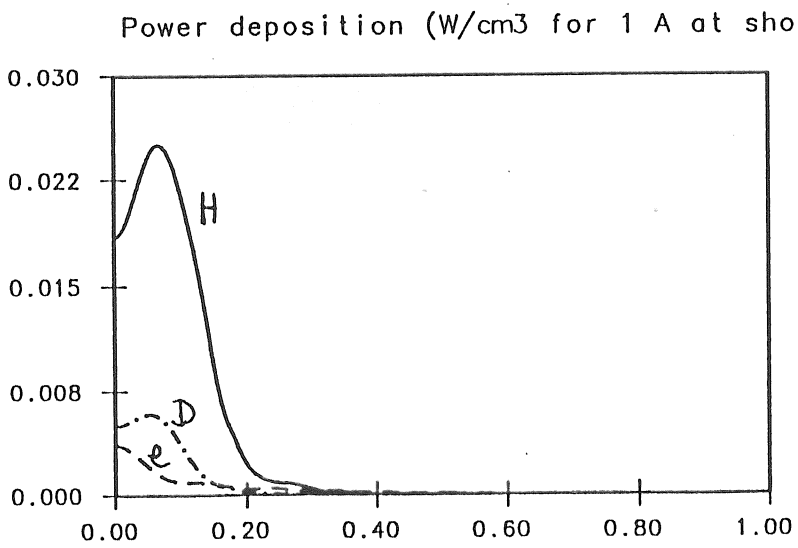
Power deposition (W/cm3 for 1 A at shorts)
0.030
0.022
0.015
0.008
0.000
H
0.00
0.20
0.40
0.60
0.80
1.00

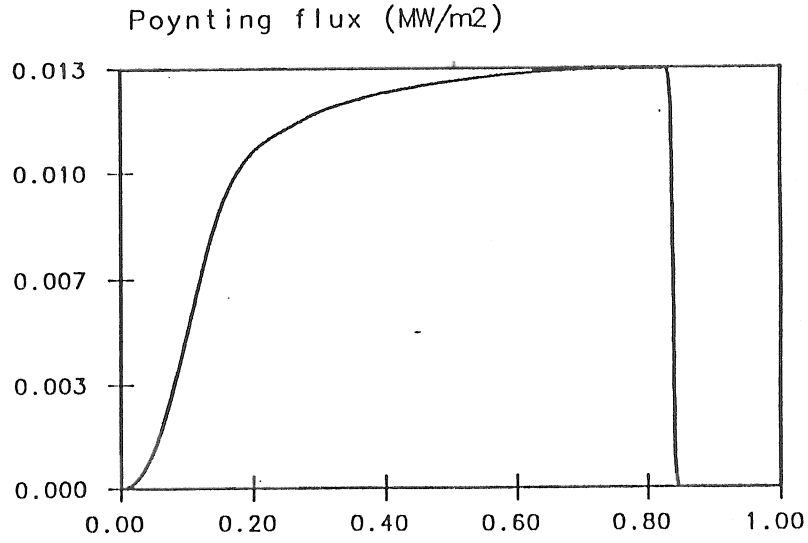
Poynting flux (MW/m2)
0.013
0.010
0.007
0.003
0.000
0.00
0.20
0.40
0.60
0.80
1.00

Fig. 8c

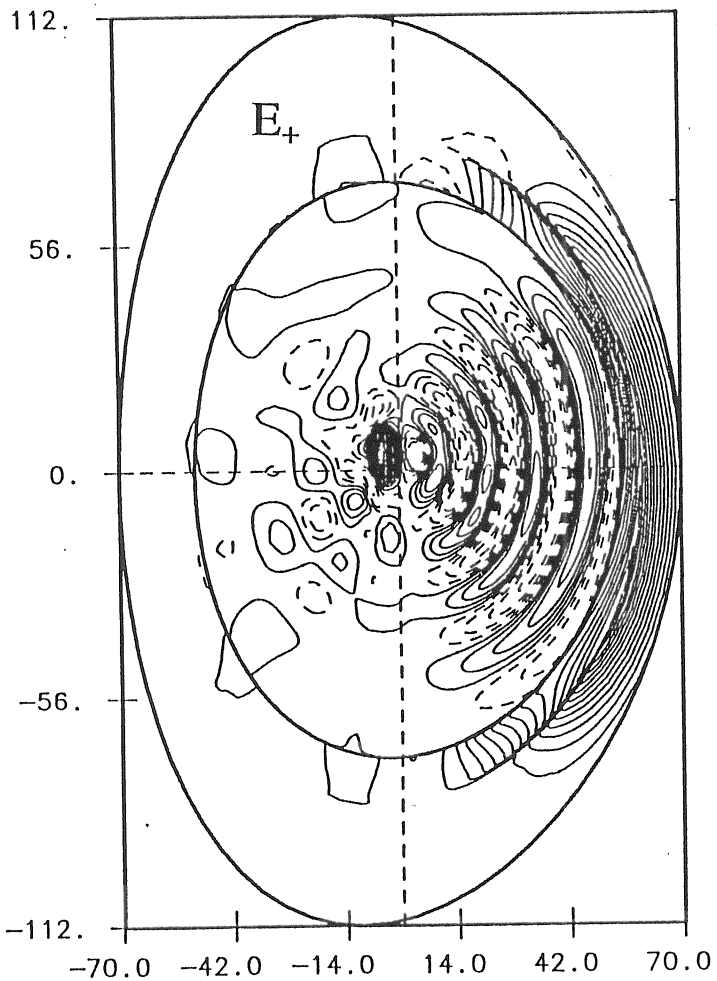
112.
56.
0.
−56.
−112.
E+
−70.0
−42.0
−14.0
14.0
42.0
70.0

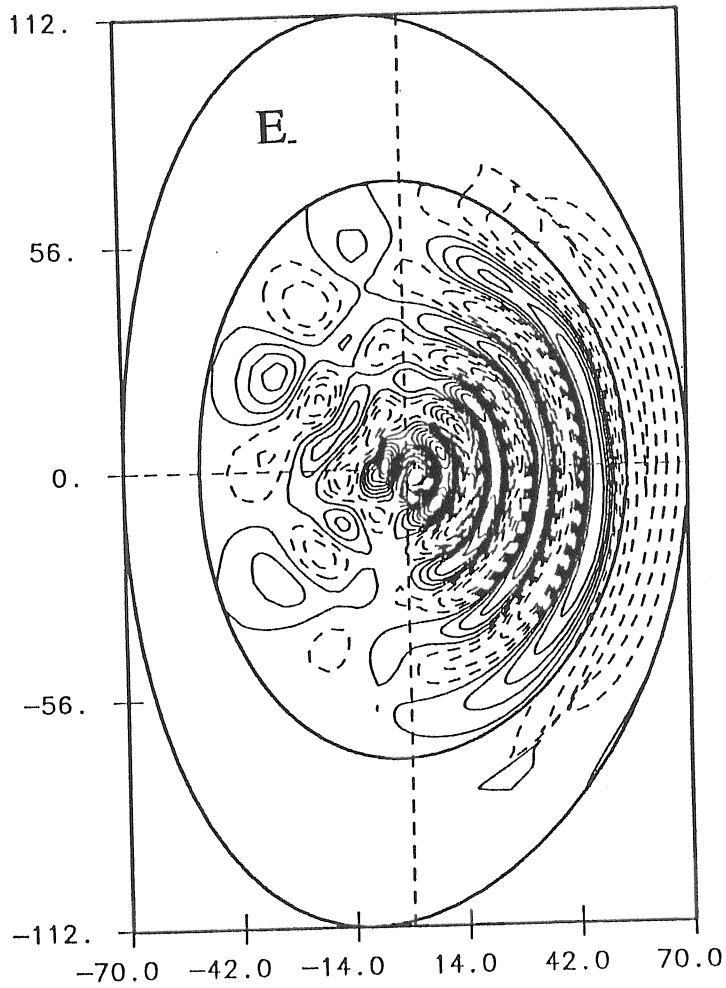
112.
56.
0.
−56.
−112.
E-
−70.0
−42.0
−14.0
14.0
42.0
70.0

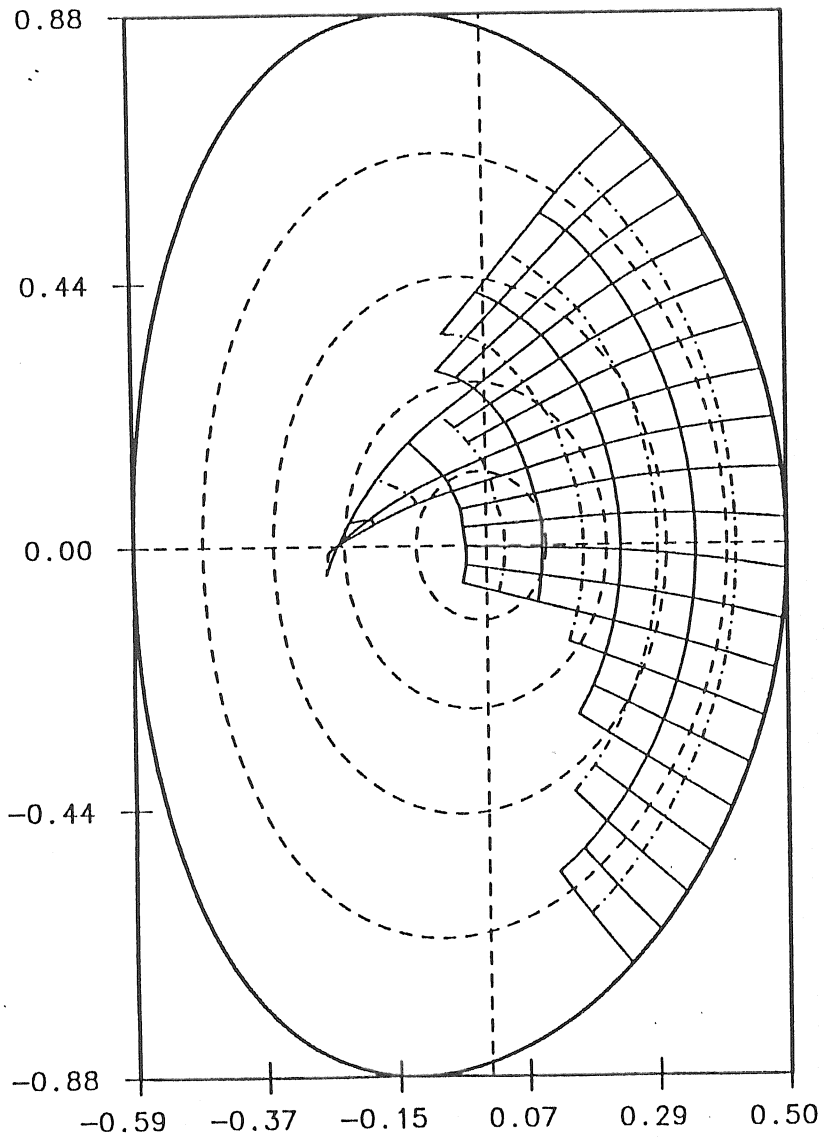

Torus radius 1.65 m
Plasma radius 0.55 m
B on axis 2.00 T
Plasma current 0.75 MA
Safety factor 5:53
Frequency 30.00 Mhz
n phi = 20, dS = 3.14
Monopole antenna
Feeders up and down

Electrons: dens. on axis 0.80 10**14 cm-3
Temp. on axis 2.00 keV
Ions: A = 2 Z = 1 conc. = 95.00 T(0) = 2.00 keV
Ions: A = 1 Z = 1 conc. = 5.00 T(0) = 2.00 keV

Fig. 9a

Fig. 9b

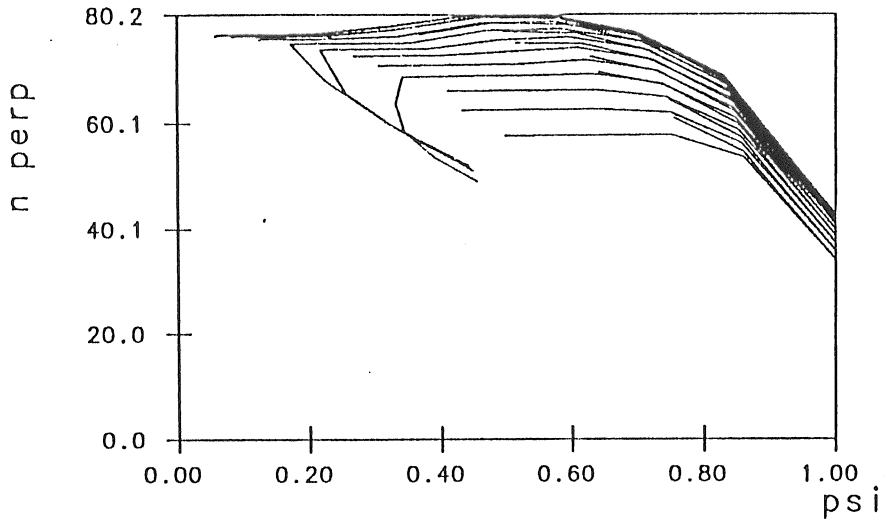
n perp
80.2
60.1
40.1
20.0
0.0
0.00
0.20
0.40
0.60
0.80
1.00
psi

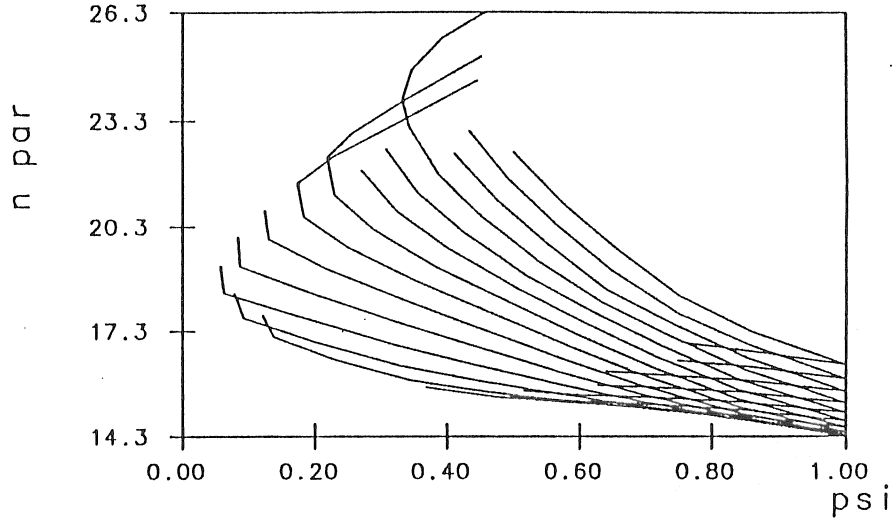
n par
26.3
23.3
20.3
17.3
14.3
0.00
0.20
0.40
0.60
0.80
1.00
psi

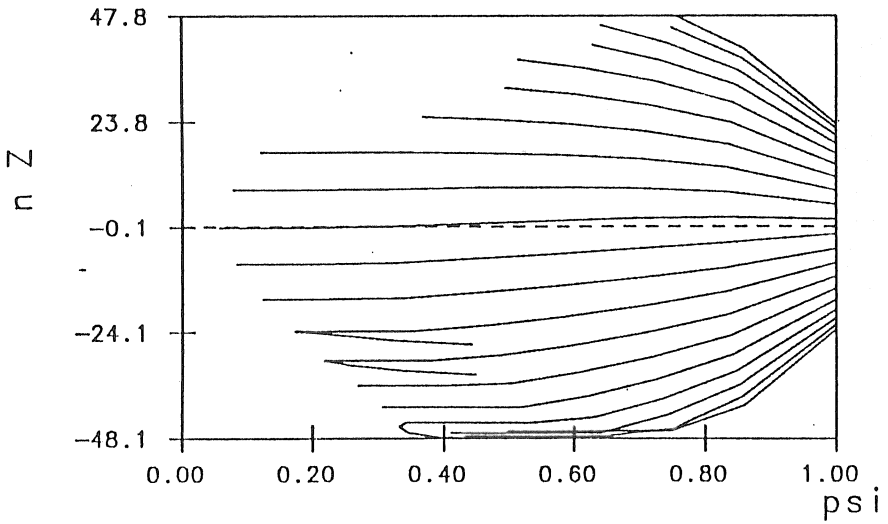
n Z
47.8
23.8
-0.1
-24.1
-48.1
0.00
0.20
0.40
0.60
0.80
1.00
psi

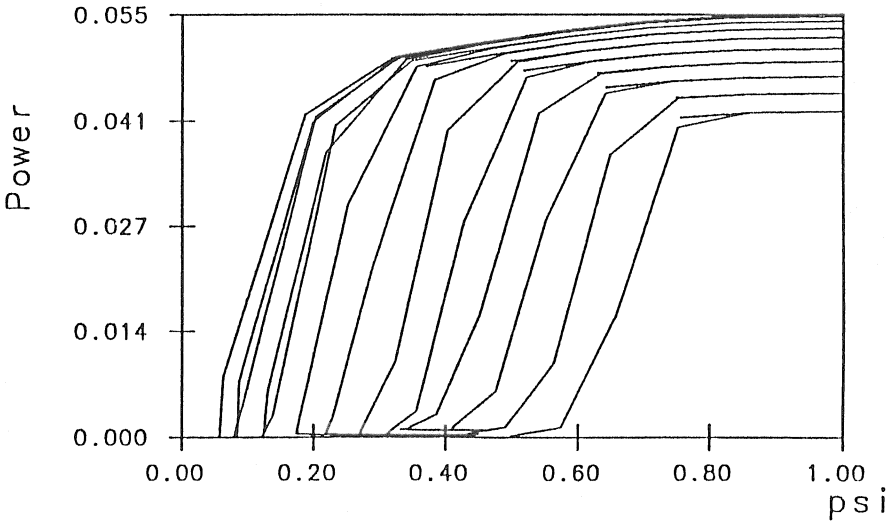
Power
0.055
0.041
0.027
0.014
0.000
0.00
0.20
0.40
0.60
0.80
1.00
psi

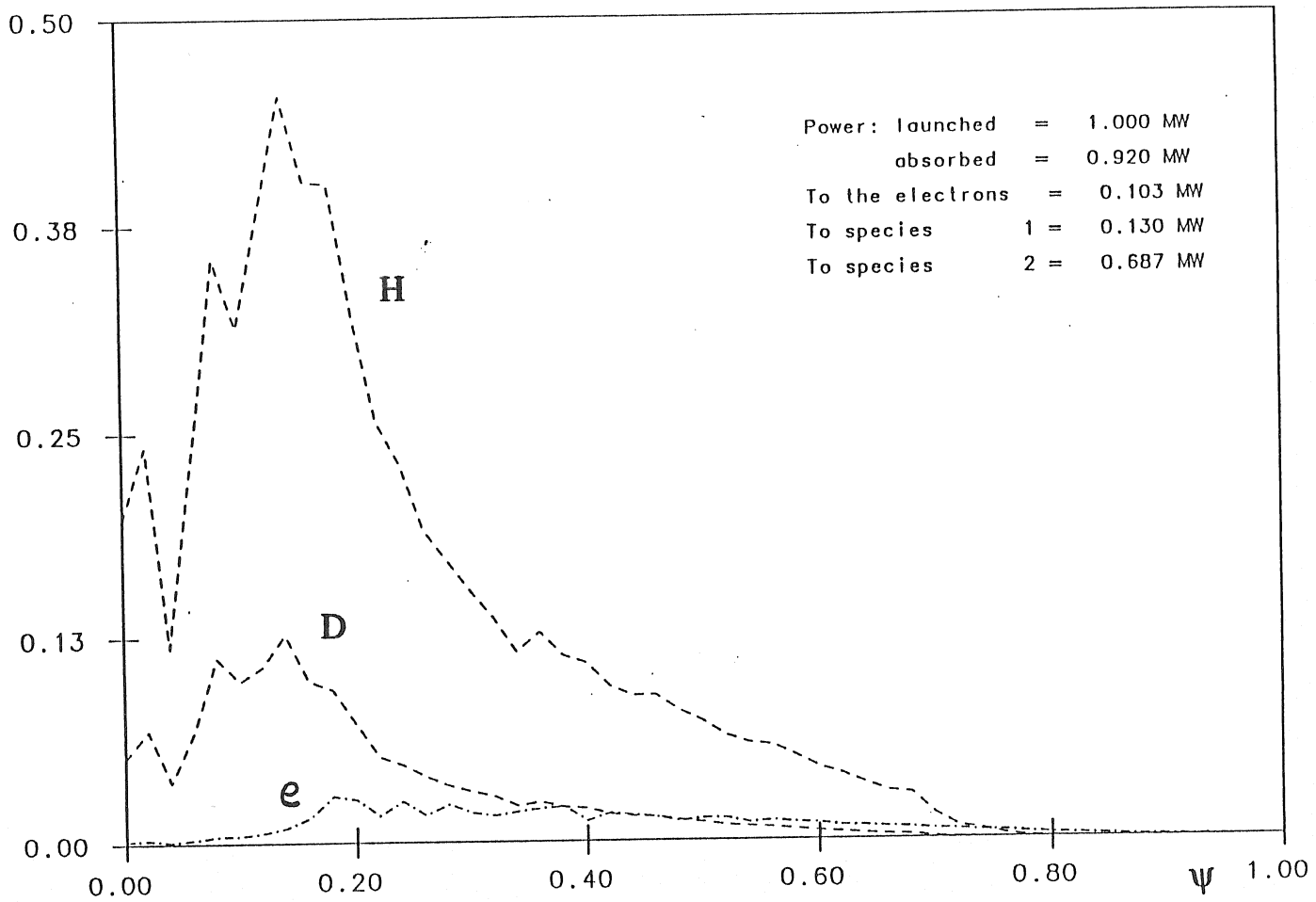
0.50
0.38
0.25
0.13
0.00
0.00
0.20
0.40
0.60
0.80
1.00
ψ
H
D
e
Power: launched = 1.000 MW
absorbed = 0.920 MW
To the electrons = 0.103 MW
To species 1 = 0.130 MW
To species 2 = 0.687 MW

Fig. 9c

Fig. 10a

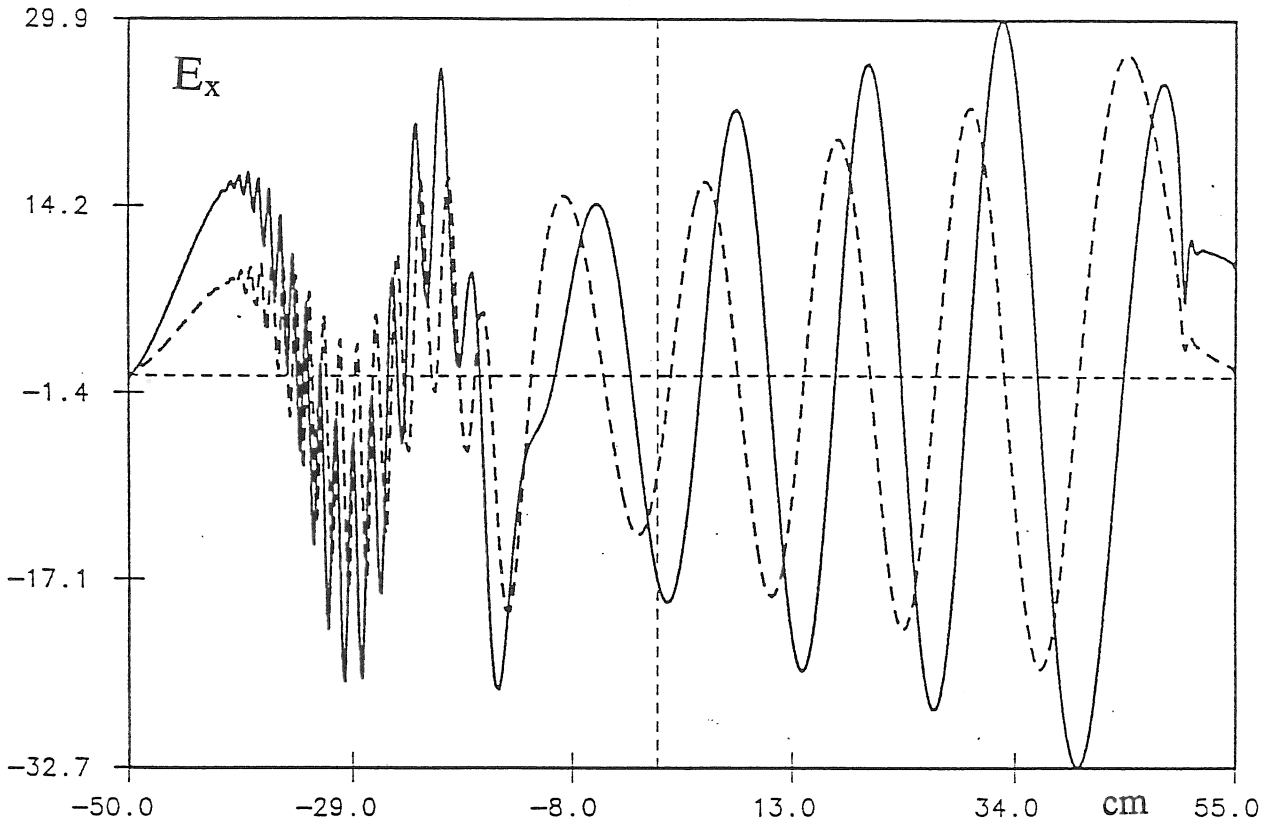
29.9
E_x
14.2
-1.4
-17.1
-32.7
-50.0
-29.0
-8.0
13.0
34.0
cm
55.0

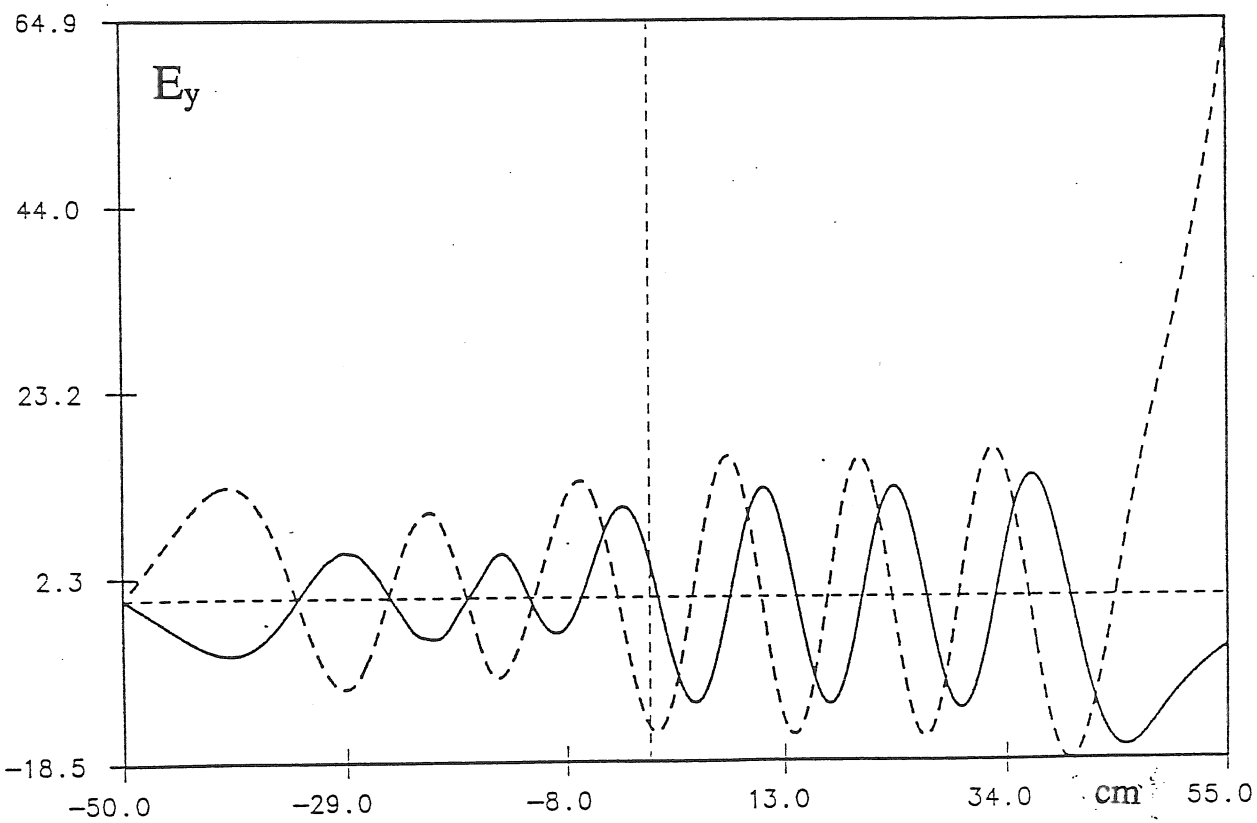
64.9
E_y
44.0
23.2
2.3
-18.5
-50.0
-29.0
-8.0
13.0
34.0
cm
55.0

Fig. 10b

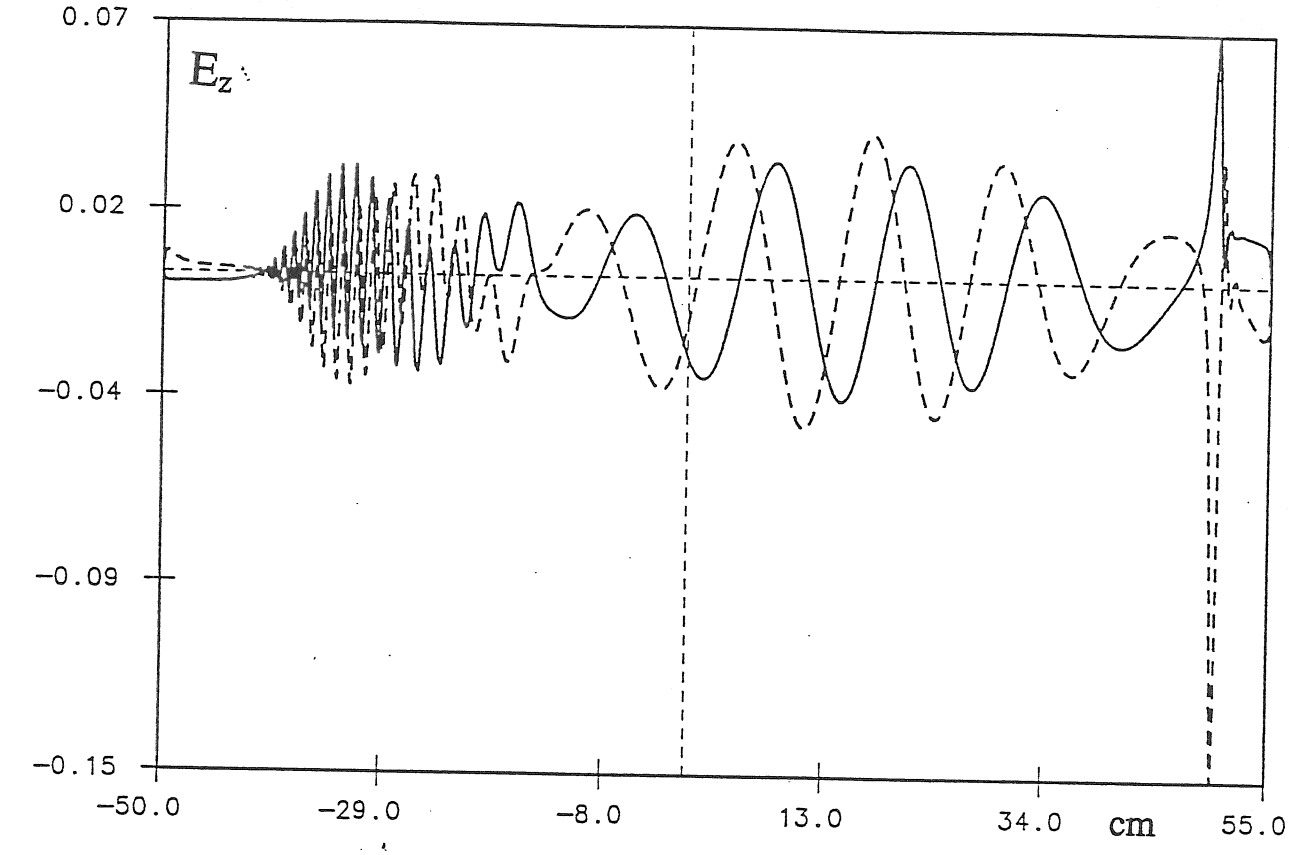
0.07
E_z
0.02
-0.04
-0.09
-0.15
-50.0
-29.0
-8.0
13.0
34.0
cm
55.0

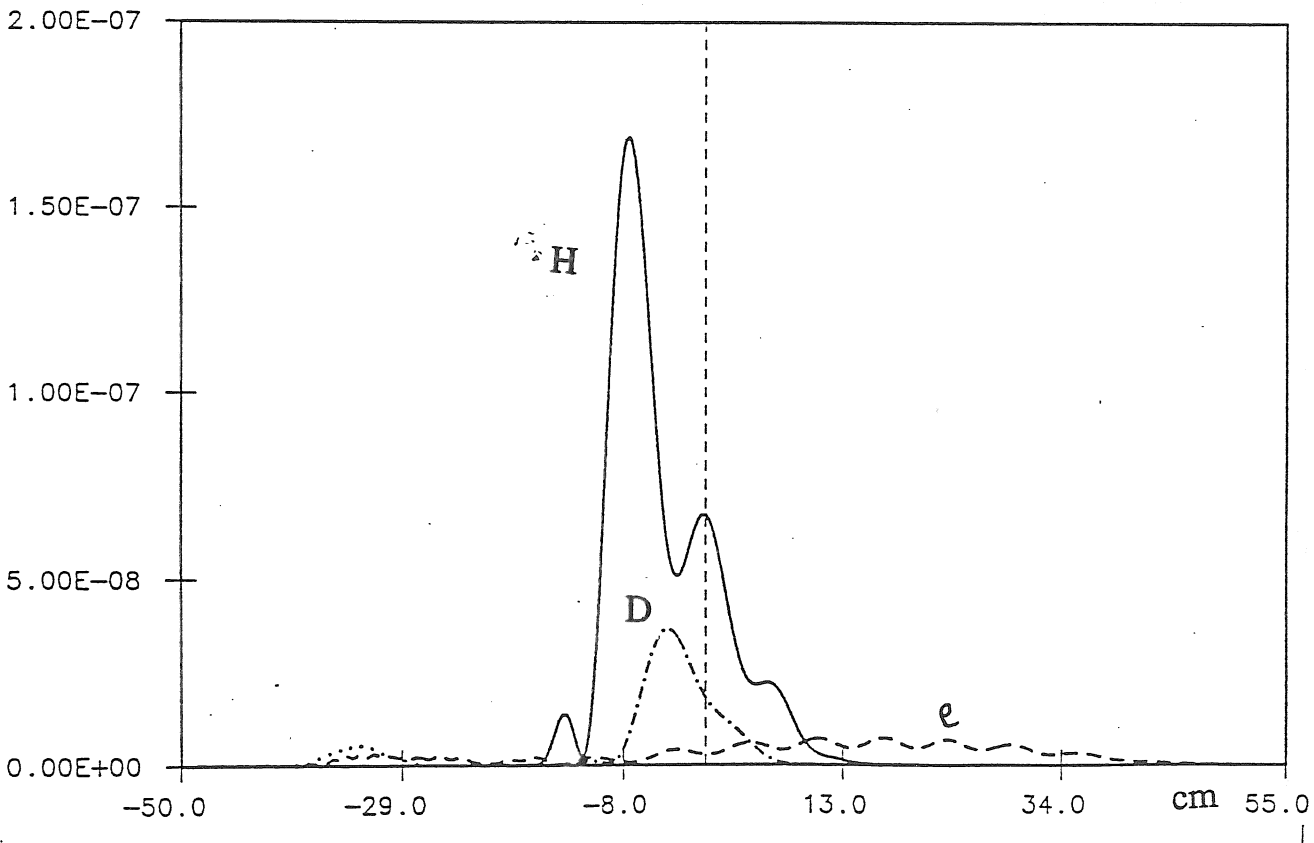
2.00E-07
1.50E-07
1.00E-07
5.00E-08
0.00E+00
H
D
e
-50.0
-29.0
-8.0
13.0
34.0
cm
55.0

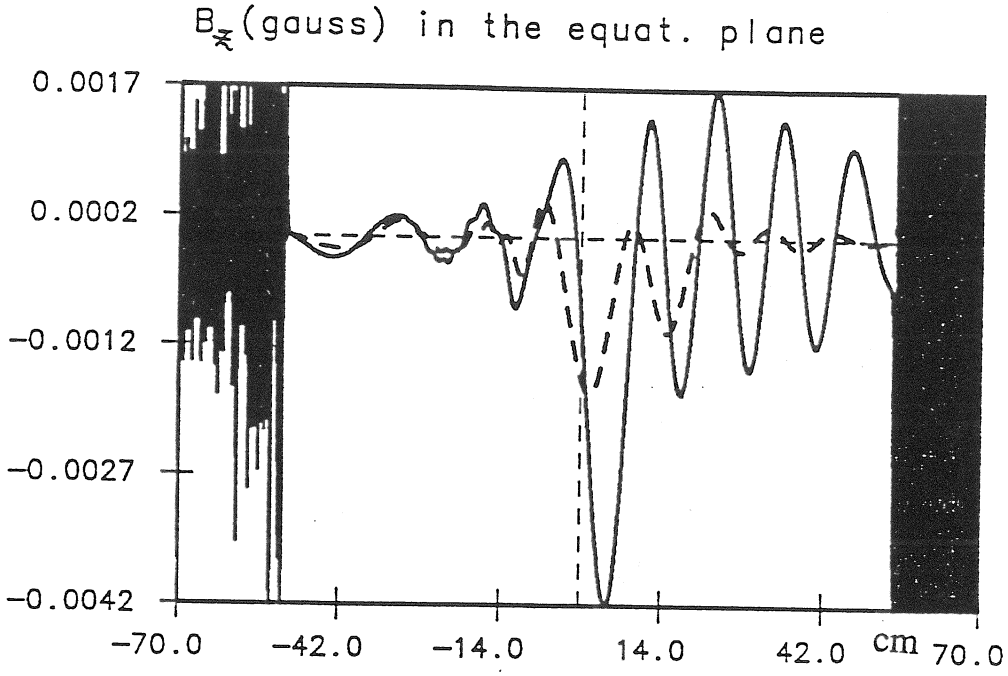
B_z(gauss) in the equat. plane
0.0017
0.0002
−0.0012
−0.0027
−0.0042
−70.0
−42.0
−14.0
14.0
42.0
cm
70.0

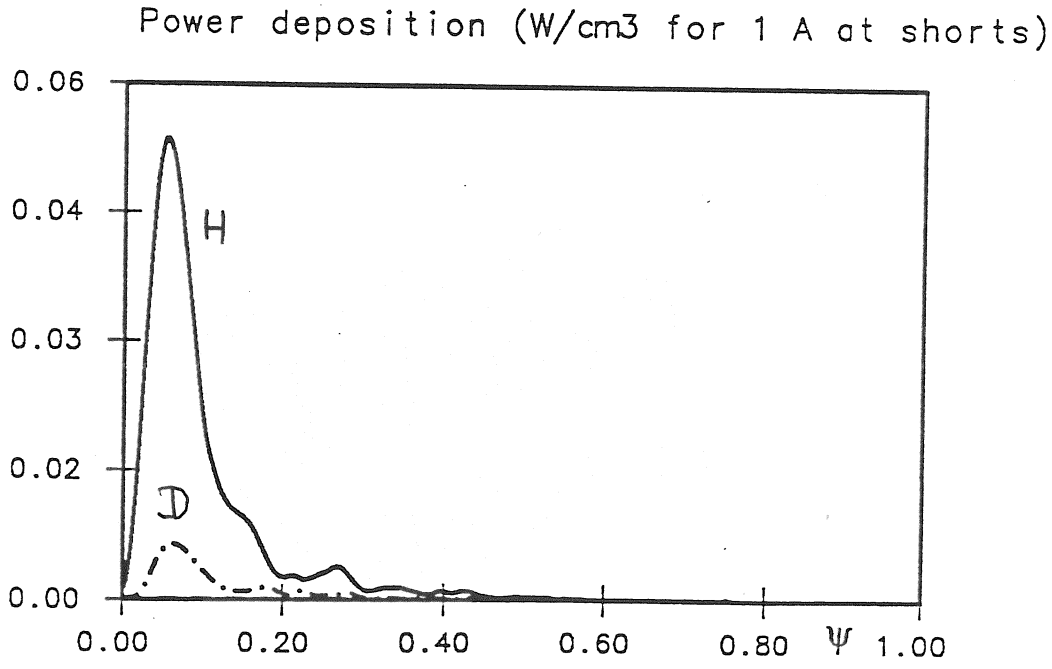
Power deposition (W/cm3 for 1 A at shorts)
0.06
0.04
0.03
0.02
0.00
H
D
0.00
0.20
0.40
0.60
0.80
Ψ
1.00

Fig. 11

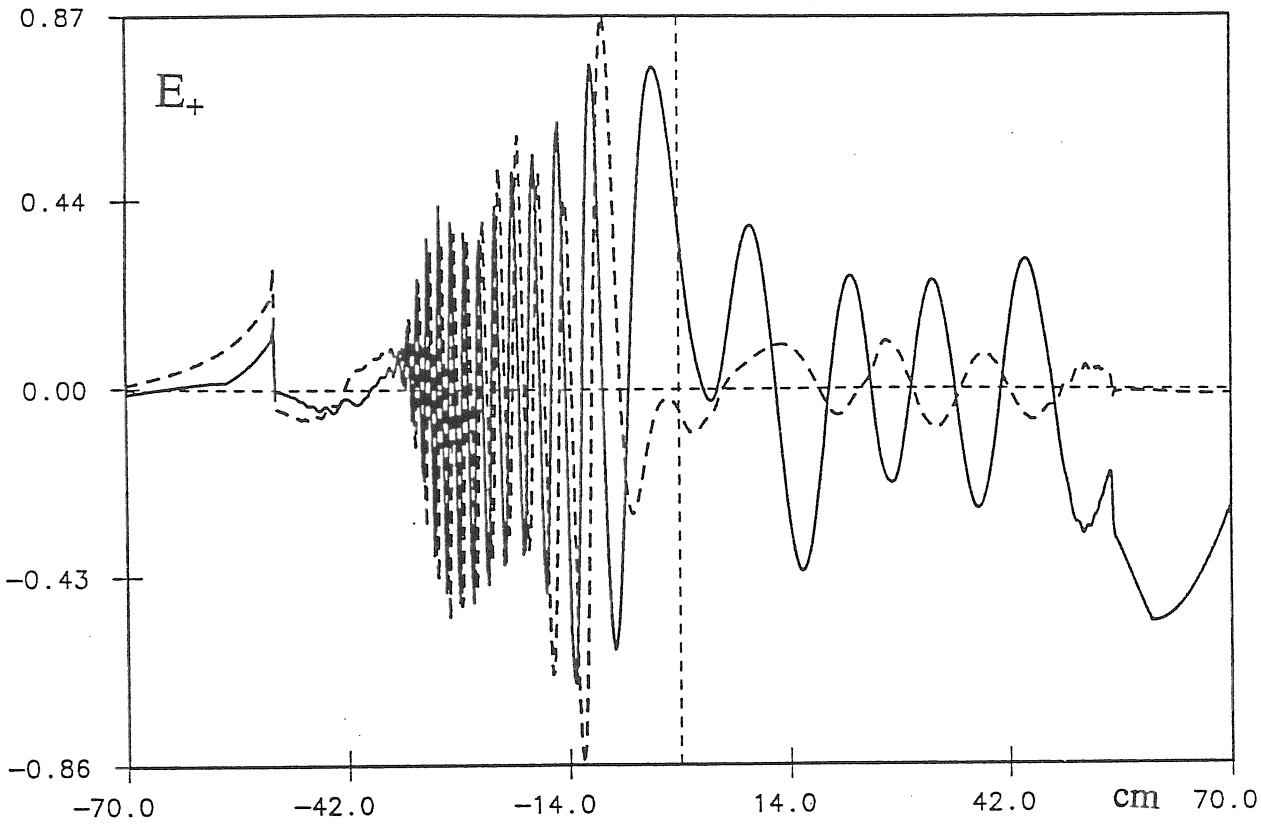
0.87
E_+
0.44
0.00
−0.43
−0.86
−70.0
−42.0
−14.0
14.0
42.0
cm
70.0

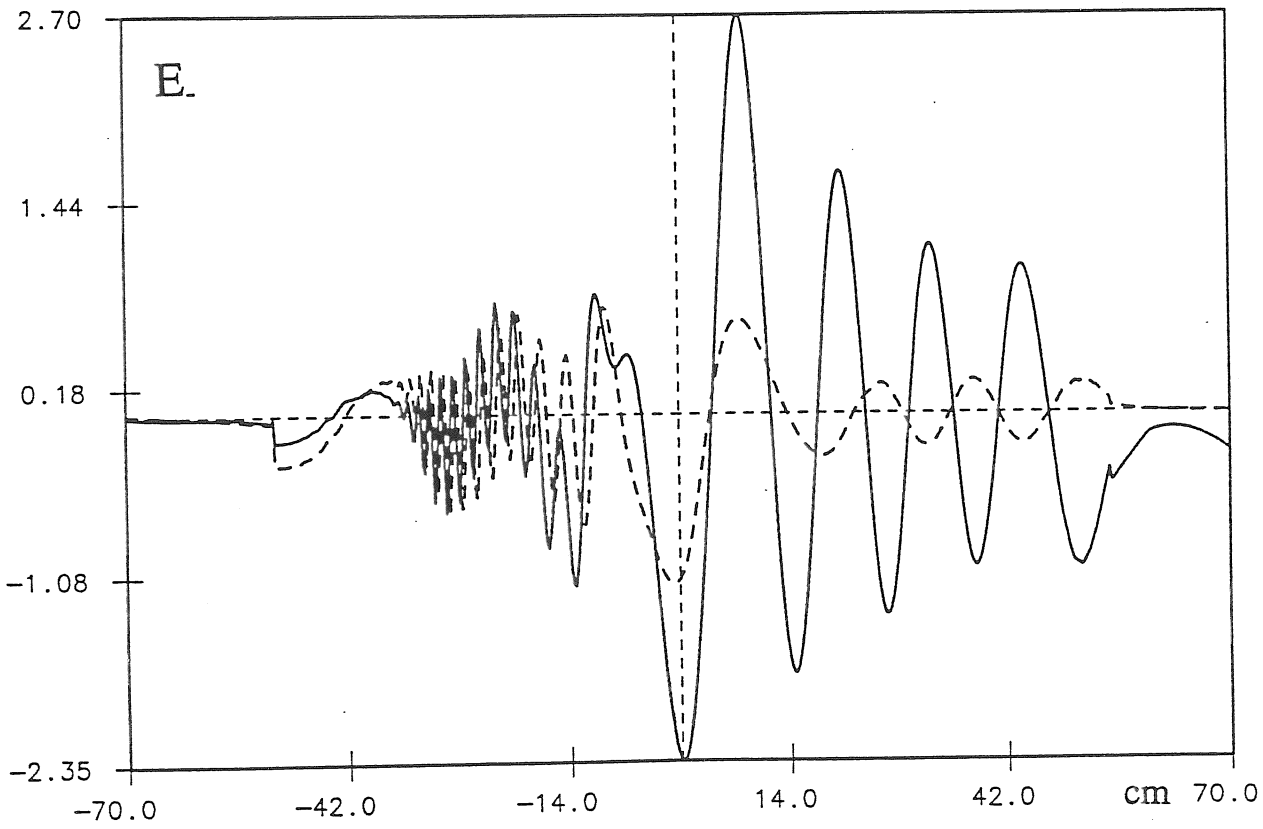
2.70
E_-
1.44
0.18
−1.08
−2.35
−70.0
−42.0
−14.0
14.0
42.0
cm
70.0

Fig. 12a

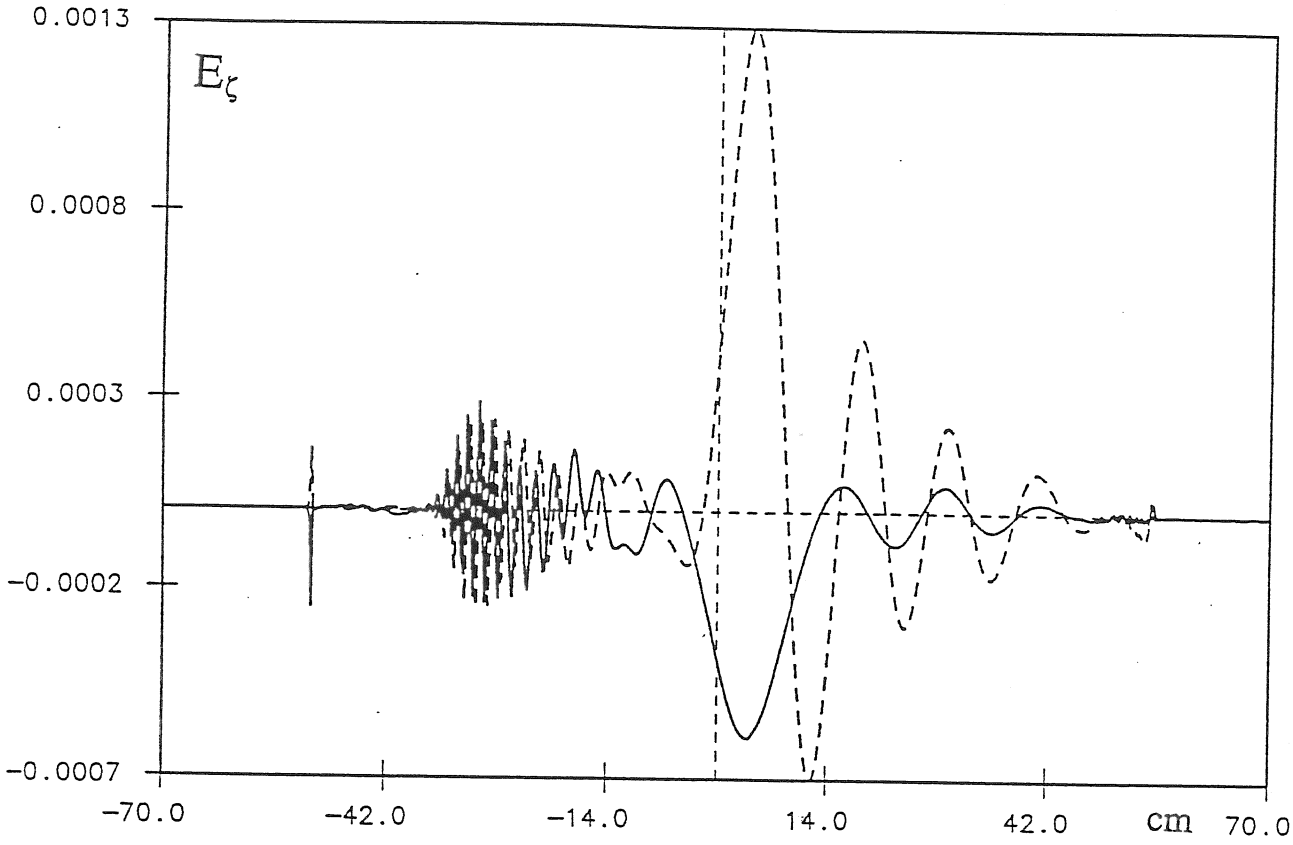
0.0013
E_ζ
0.0008
0.0003
−0.0002
−0.0007
−70.0
−42.0
−14.0
14.0
42.0
cm
70.0

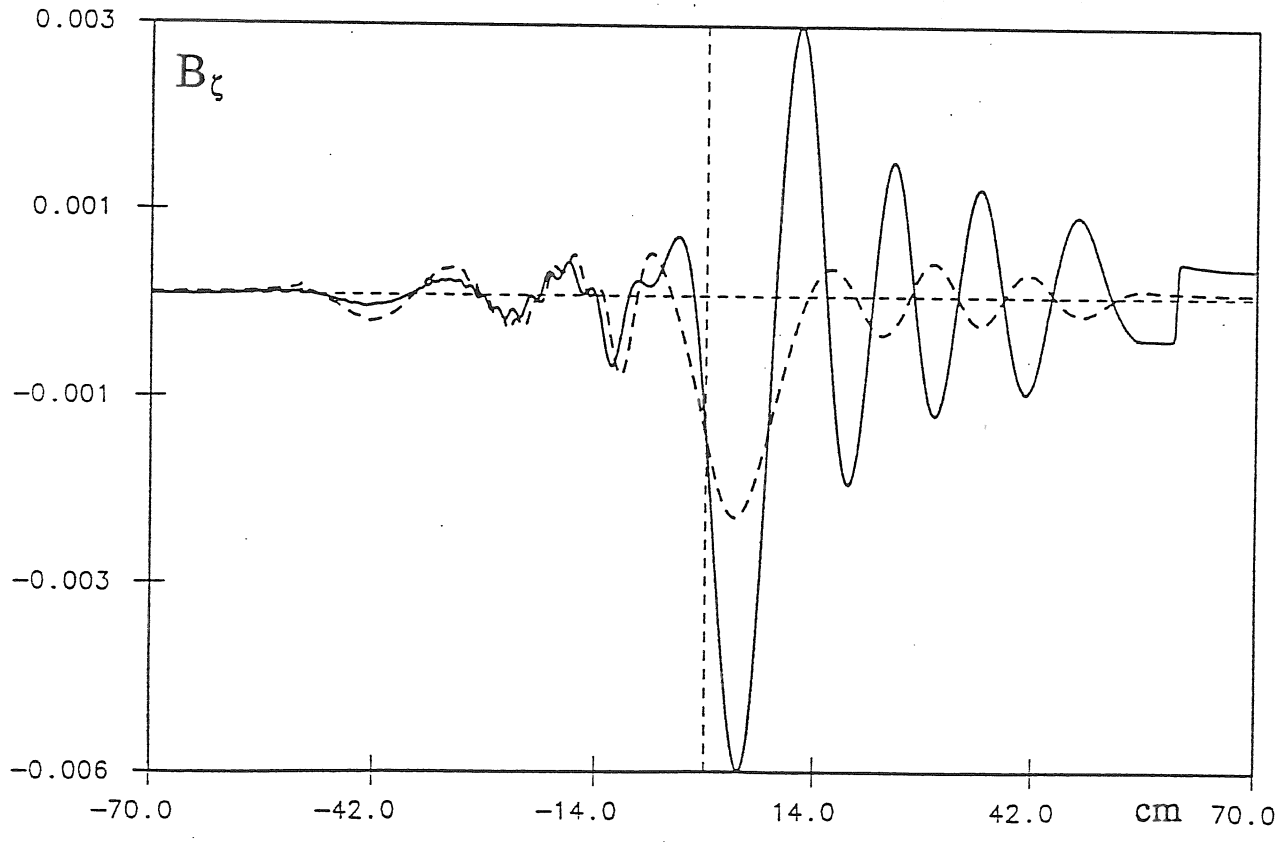
0.003
B_ζ
0.001
−0.001
−0.003
−0.006
−70.0
−42.0
−14.0
14.0
42.0
cm
70.0

Fig. 12b

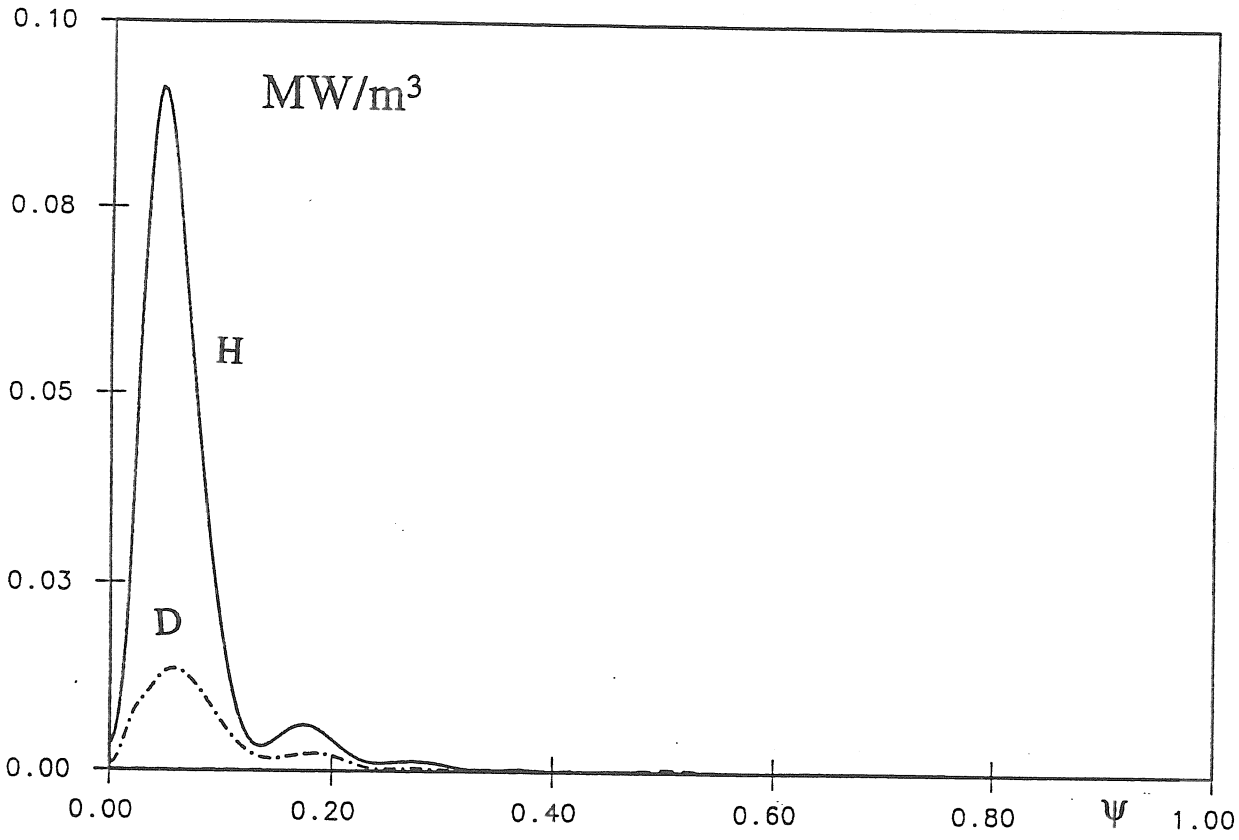
0.10
MW/m3
0.08
H
0.05
0.03
D
0.00
0.00
0.20
0.40
0.60
0.80
ψ
1.00

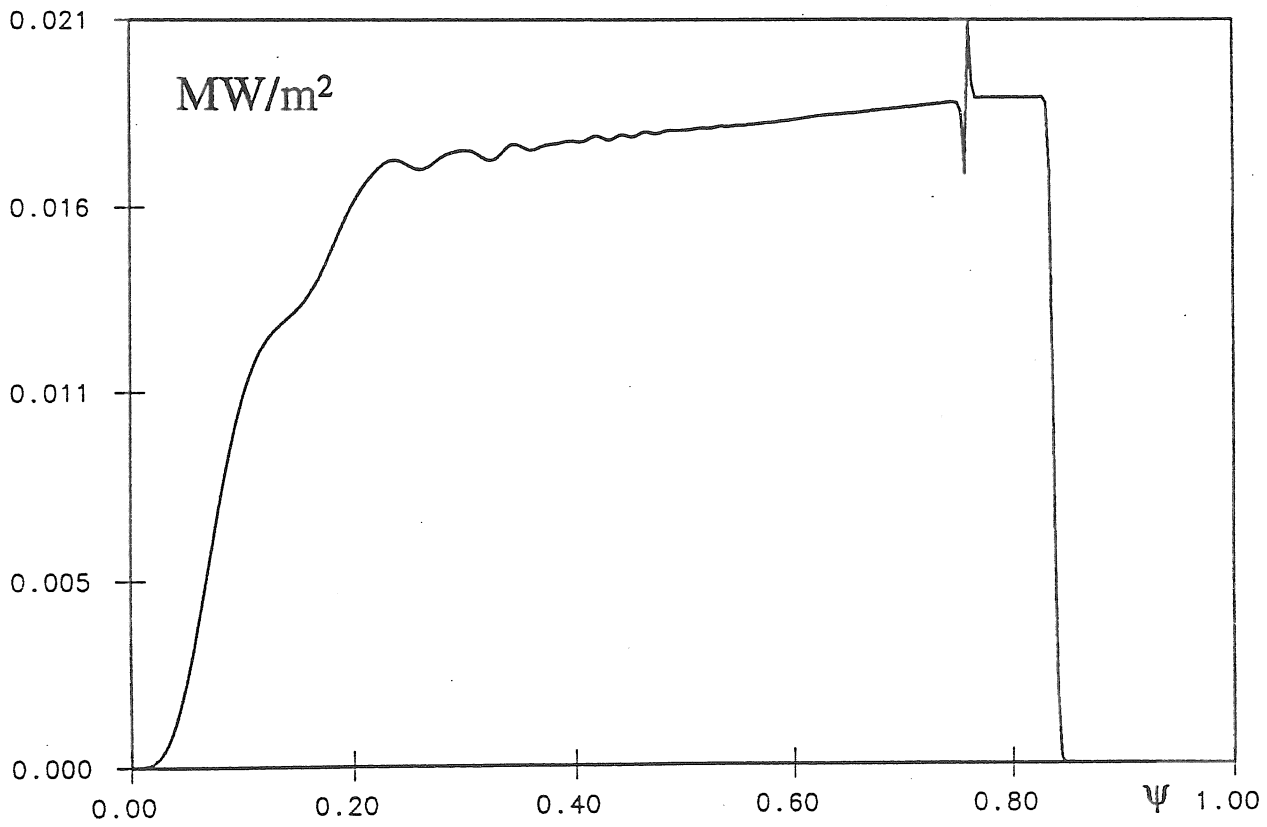
0.021
MW/m2
0.016
0.011
0.005
0.000
0.00
0.20
0.40
0.60
0.80
ψ
1.00

Fig. 12c

Fig. 13

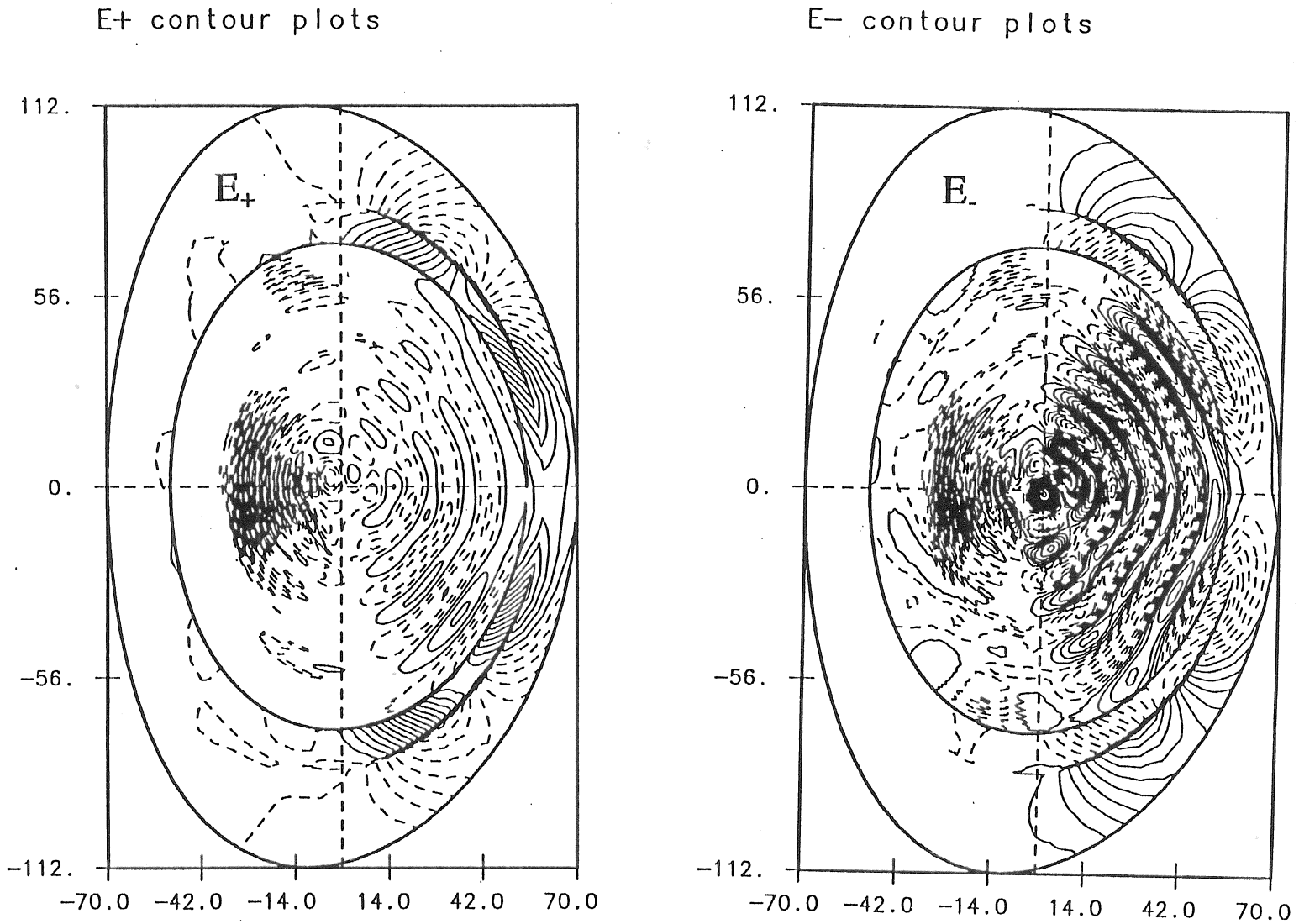
E+ contour plots
E− contour plots
E+
E-
112.
56.
0.
-56.
-112.
-70.0
-42.0
-14.0
14.0
42.0
70.0